High data-rate ultra low-power backscatter wireless communication systems for brain-computer interfaces

Eleftherios Kampianakis

A dissertation
submitted in partial fulfillment of the
requirements for the degree of

Doctor of Philosophy

University of Washington

2019

Reading Committee:

Matthew S. Reynolds, Chair

Chet Moritz

Payman Arabshahi

Pavel Nikitin

Program Authorized to Offer Degree:
Electrical & Computer Engineering

University of Washington

Abstract

High data-rate ultra low-power backscatter wireless communication systems for
brain-computer interfaces

Eleftherios Kampianakis

Chair of the Supervisory Committee:
Professor Matthew S. Reynolds
Department of Electrical & Computer Engineering

Neural interfacing is a promising technology for effectively treating a multitude of challenging clinical conditions. Recent research has demonstrated that some tetraplegic patients can control robotic limbs using a brain-computer interface (BCI), signifying the beginning of an era wherein many forms of paralysis may be treatable with a neuro-prosthesis. However, the current state of the art is bulky, tethered, and impractical for applications outside a clinical lab setting. Moreover, current wireless communication approaches for brain computer interfaces (BCI) do not meet the necessary specifications for power, size, and bandwidth. In contrast, we developed fully integrated BCIs equipped with high data-rate and low power miniaturized wireless backscatter communication systems to enable the development of autonomous brain-controlled prosthetics. First, we proposed a wireless μ-Power, low-noise frequency mixing approach for extending the passband frequency response of existing neural interfaces. We demonstrated the translation of a pre-recorded mouse electrocorticogram from a frequency range of 0.5 Hz to 100 Hz up to an intermediate frequency (IF) of 407 Hz, thus enabling the use of an existing integrated circuit (IC) for electrocorticography (ECoG), despite its low-frequency cutoff of 12 Hz. Subsequently, we presented a dual-band implantable BCI that integrates 47%-efficient high frequency (HF) wireless power delivery into a 5 Mb/s ultra-high frequency (UHF) backscatter communication. The implant system supports ten neural channels sampled at 26.10 kHz and four electromyography (EMG) channels sampled at 1.628 kHz and can communicate with a custom software-defined-radio-based external system with a packet error ratio (PER) that is better than 0.19 % at an implant depth of up to 3 cm. Finally, in order to enable neural plasticity experiments inside the home cages of freely behaving animals, we

developed a 25 Mbps backscatter-based data uplink for Neurochip 3 using a differential quadrature phase shift keying (DQPSK) constellation. We statically collected 10^4 packets from 126 locations, and the system exhibited effectively 0 % (PER) for all but two of the surveyed sites despite the reverberant cavity effects of the animal cage that critically impair the communication channel.

TABLE OF CONTENTS

ACKNOWLEDGMENTS

and it was all fantastic. Thank you!

To my Mom and Dad, my brother Andreas, and my sister Marianna thank you for being the proudest family one could ever have. Thank you for supporting every decision I've made so far even if that meant creating a distance of hundreds of miles between us. Thank you for believing in me and telling me that I can do this even though you didn't fully understand what I was doing. You were right.

Finally, I would like to thank my support group at Hall Health and my therapist Ricardo Hidalgo. The mental gymnastics that are required to go through the process of getting a Ph.D. degree need an Olympic-level mental fortitude. I didn't come prepared, but luckily I had a solid team and a wise coach. There are not enough words I can use to express my gratitude for helping me come out of this process sane, healthy and very very happy.

To Ricardo and the group.

Chapter 1

INTRODUCTION

1.1 Brain computer interfaces

1.1.1 Introduction

Brain computer interfacing (BCI) is an increasingly promising technology that could facilitate the treatment of a plethora of clinical conditions. The spectrum of clinical conditions that BCI could address includes severe depression, muscle spasticity, chronic pain, epileptic seizures, and numerous others [1, 2]. In particular, BCI exhibits tremendous potential in the treatment of paralysis. Recent research published in *Nature* by Hochberg et. al. [3] demonstrated that a tetraplegic patient can control a robotic arm with BCI to restore function and eat a chocolate bar by herself. Other achievements include the partial restoration of arm movement in a person with tetraplegia through BCI-controlled muscle stimulation [4] and the implementation of a high-performance communication system using a BCI-controlled keyboard among paralyzed patients [5]. Specifically, BCIs for prosthesis implement one or more of the following functions:

1. Recording and telemetering the electrical signals from the brain.
2. Signal processing to extract stimulation patterns and control parameters.
3. Stimulation of the brain or with the extracted patterns from step 2.
4. Control of prosthetics, such as robotic arms, with the extracted control parameters from step 2.
5. Haptic/sensory feedback from the prosthesis.

The integration of these functions is shown in Fig. 1.1. The brain signals are recorded and telemetered from a fully implanted recording/stimulation device to an external processor. The processor extracts the control parameters for a robotic limb in real-time. The robotic limb incorporates haptic feedback sensors that the implant utilizes to restore the sense of touch by stimulating the brain accordingly. Each of the functions summarized above pose significant engineering and scientific
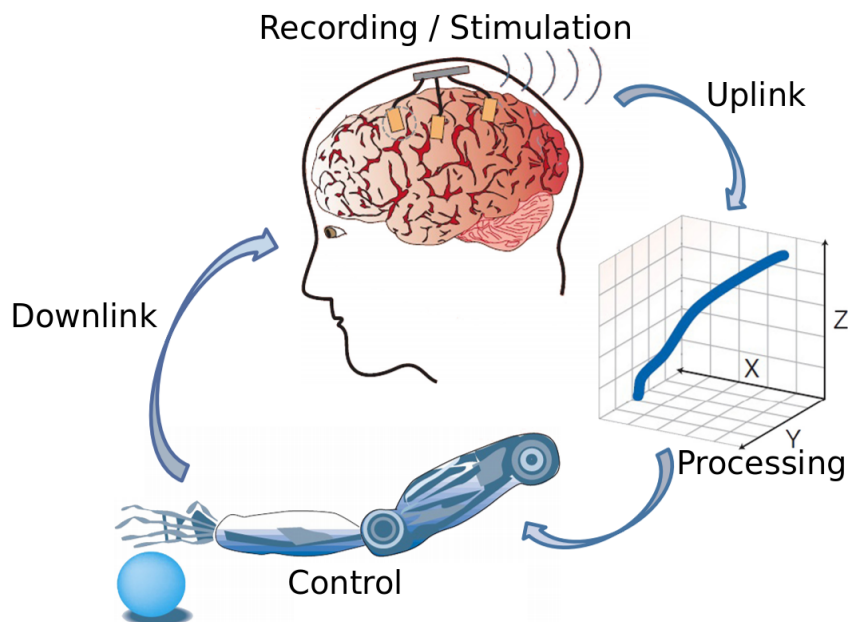
Figure 1.1: BCI block diagram: The signals from the brain are recorded and processed in order to control robotic limbs or stimulate the body/brain. Adapted from [6]

challenges. The majority of this thesis addresses the challenges that revolve around recording and telemetering brain signals in real-time while developing BCIs for prosthesis.

1.1.2 Brain Activity Recording

The brain consists of more than 100 billion neurons. The ideal brain recording interface is one that doesn't require invasive surgery or damage the brain and that can record brain activity with high fidelity from each neuron, individually and simultaneously. We are far from achieving such a monumental task, but the technology for achieving a subset of these specifications is available now. Three methods in particular have been developed to directly measure the voltage potential from the brain, each with distinct tradeoffs: electroencephalography (EEG), electrocorticography (ECoG), recording of local field potentials (LFP) or single neurons (SN). These methods are distinguished by their degree of invasiveness and are summarized in Table 1.1 [7].

EEG, although the least invasive method, is critically limited for use with BCIs for prosthetics [8] due its bandwidth limitations. On the other hand, ECoG exhibits good tradeoff between

Table 1.1: Different methods for acquiring neural signals from the brain. Adapted from [7].

	EEG	ECoG	LFP/Single Neuron
Invasiveness	None	Craniotomy	Craniotomy Neural damage
Bandwidth	0.5-5Hz	1-500Hz	1 Hz–10 kHz
Amplitude	1-50 μV	1-500 μV	0.010-50 mV
Spacing	3 cm	0.2-10 mm	0.1-1 mm
Area Coverage	Whole brain	$\sim$ cm^3	$\sim$ mm^3
Max. Duration	Decades	Decades	Months

invasiveness, lifetime, and resolution and is, therefore, a suitable candidate for BCIs [8]. ECoG requires craniotomy and is thus more invasive than EEG but doesn't cause brain damage as the electrodes are installed non-invasively on top of the dura right underneath the skull. Finally, the most precise method for measuring the neuronal potentials involves penetrating the brain with electrode structures such as the Utah array [9] and monitoring single neurons (SN) or local field potentials (LFP). As shown in Table 1.1, recording LFP/SN comes at the cost of reduced lifetime and increased invasiveness, but it has demonstrated tremendous potential in research experiments and applications, both in animals [10] as well as in humans [3]. The technologies developed during this thesis are exclusively suitable for ECoG and LFP/SN, because we believe that these methods demonstrate the highest potential for applicability in future BCIs, particularly for prosthesis.

1.2 Wireless BCIs

1.2.1 The Bandwidth Challenge

At the moment, the only devices that provide the computing power necessary for real-time processing of complex brain signals are large structures that can only reside outside the skull [3, 4, 5]. As a result, a majority of researchers' efforts are focused on systems that telemeter the data wirelessly to an extra-cranial processing unit [7, 12, 13, 14, 15, 16].
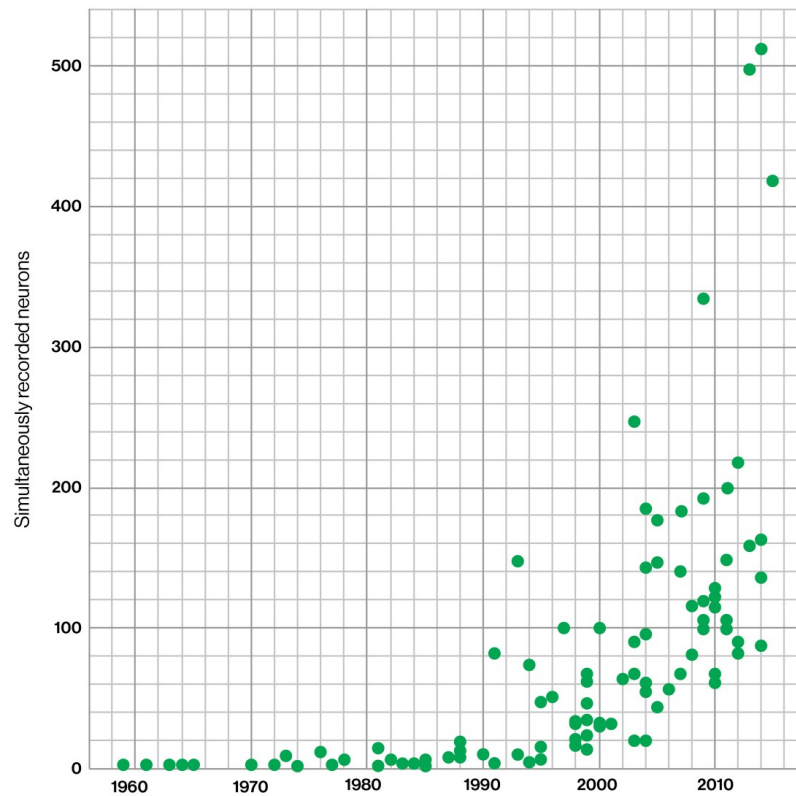
Figure 1.2: "Number of neurons recorded simultaneously from any animal's brain. Each point represents a published paper". Adapted from [11].

Stevenson et al. observed that "Over the last five decades, progress in neural recording techniques has allowed the number of simultaneously recorded neurons to double approximately every 7 years, mimicking Moore's law" [11]. This is illustrated by a graph in Fig. 1.2. Exponential increase in neural channel count translates to exponential increase in bandwidth demands, and sampling more neural signals is essential in order to implement high fidelity prosthesis. For example, it has been recently estimated that at least 100k neural channels are required to sufficiently decode body movement [17]. However, the number of channels that a BCI can telemeter to an external system is ultimately constrained by its data-rate.
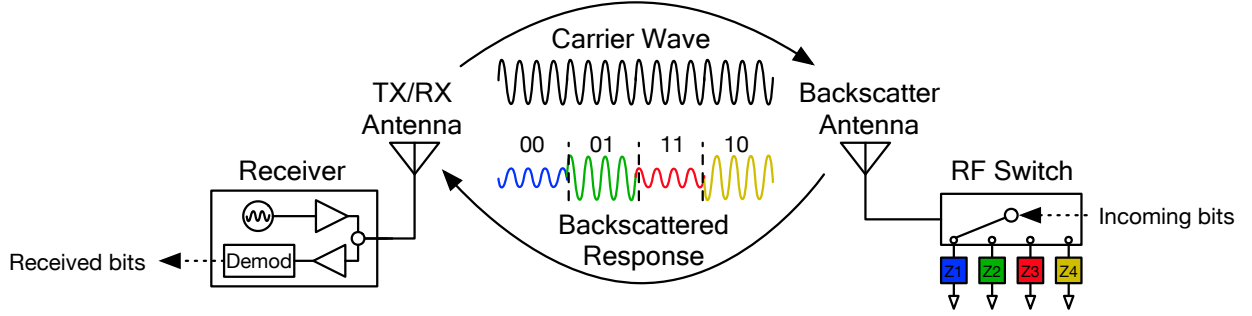
Figure 1.3: High order backscatter communication: the receiver/reader generates a carrier wave. The carrier wave is reflected with different phase/amplitude from the backscatter device modulating multiple bits/symbol (2 in this case).

1.2.2 High data-rate Backscatter Communication for BCIs

High bandwidth conventional wireless standards including WiFi and Bluetooth Low Energy (BLE) don't meet the power and size specifications of BCI. For example, a BLE transmitter consumes more than 10 nJ/bit [18], and a 1 Mbps uplink would dissipate 10 mW for the transmitter alone. Therefore, these approaches are thermally unfavorable for implanted applications where the power dissipation into tissue is limited to of 10 mW/cm^3. Moreover, in battery-operated BCIs such as the Neurochip [19], high power consumption leads to reduced life-time and, thus, constrains experimentation.

An appealing approach in BCI uplinks is backscatter communication. In principle, when a carrier wave (CW) is incident on an antenna and the load of the antenna changes, the CW will be reflected with a phase and amplitude that depends on the corresponding antenna termination load. High-order backscatter modulation schemes that allow for high data-rates to be achieved with very low power have been explored in the literature [20]. In particular, a BCI that employs backscatter communication requires a single RF switch to uplink the neural data to the corresponding host. Therefore, the use of RF amplifiers and high-frequency oscillators, which typically consume the largest portion of the power-budget and take up the bulk of the physical space in a communication system, is avoided.

Thomas et al. demonstrated that data-rates greater than 96 Mbps [20] can be achieved using backscatter communication with power as low as 15.5 pJ/bit, which is orders of magnitude less

power than WiFi and BLE. A block diagram of the functionality of such a communication scheme is depicted in Fg. 1.3. A receiver/reader generates a carrier wave at a single frequency. The carrier wave travels to the device employing a high order backscatter modulator with a low-power RF switch. In Fig. 1.3, the switch can select between 4 different impedances that are used to terminate the antenna. When the antenna is terminated with a load, the incident wave on the BCI antenna is reflected with a phase and amplitude that depends on that particular load. Therefore, 4 different loads will reflect 4 different phase/amplitude combinations. By using this method, multiple bits can be encoded per reflected symbol, thus reducing the need for high clock speeds on the BCI-side and as a result, reducing the energy cost per bit.

However, the aforementioned benefits come at a cost: a more challenging communication channel. This is due to the fact that the carrier wave needs to travel twice the distance when compared to conventional radios, i.e., from the external system to the BCI where the CW gets modulated and back to the external system. Therefore, the losses are a function of the fourth power of the distance between the carrier emitter and backscatter modulator [21]. This effect creates additional limitations in extremely lossy implanted environments or in environments with extreme multipath such as metal animal cages. This work addressed these challenges effectively and developed high data-rate power-efficient miniaturized backscatter communication interfaces for BCIs.

1.2.3   Prior Art Comparison

Since low power dissipation is a critical constraint for BCIs, various non-traditional communication modalities have been explored. The most prominent examples in the literature include the aforementioned radio frequency (RF) modulated backscatter [22, 23, 24, 25], backscatter of ultrasound [12], and impulse radio ultrawideband (IR-UWB) transmission [26]. However, the combination of low power and minimal size with high data-rate and a simple implementation is unique to backscatter communication and highly desirable for the development of BCI uplinks.

This work integrates all the necessary components to develop fully functional BCIs for recording brain activity, including biorecording integrated circuits (IC), real-time receivers, biocompatible encapsulation, antennas, wireless power transfer (WPT) etc. Therefore, in this section, comparisons are made among systems that incorporate the same level of integration and achieve similar levels of functionality. A comprehensive comparison of all the competitive systems in the prior art is depicted in Table 1.2.

Table 1.2: Comparison table with the state of the art in wireless neural recording BCIs.

	Muller 2015 [7]	Seo 2016 [12]	Biederman 2013 [13]	Kiourti 2016 [15]	Szuts 2011 [27]	Borton 2013 [28]	Miranda 2014 [29]	This work [30]	This work [31]	Units
BCI type	Implant	Implant	Implant	Implant	External	Subcutaneous	External	**Implant**	**External**	
Custom ASIC	✓	✗	✓	✗	✓	✓	✗	✓	✗	
Dimensions (LxWxH)	6.4x6.4x0.7	0.8x3x1	0.5x0.25x0.5	15x16x0.8	60x30x30 [a]	56x42x11	38x38x51	**25 (diam) x 2.8**	**85 (diam) x 63**	mm
Noise Floor	1.2	180	6.5	63	4	8.6	5	**18**	**2.4**	μV_{RMS}
ADC res.	15	8	10	N/A	N/A	12	12	**11**	**16**	bits
Neural BW	0.5	30	10	5	2	8	10	**11**	**20**	kHz
# Simult. Ch.	64	1	4	1	64	100	32	**10**	**16/4**	#
Sampling rate	1	30	20	n.r.	20	20	30	**26.1**	**5/25**	ksps
Stimulation	✗	✗	✗	✗	✓	✗	✗	✓	✓	
WPT	✓	N/A	N/A	N/A	✗	✓(only charging)	✗	✓	**I.P.**	
Total DC power	12	0	0.01	0	645	90	142	**1.33**	**500**	mW
Comms type	RF Bac.	US Bac.	Inductive	Passive mixer	Active RF	Active RF	Active RF	**RF Bac.**	**RF Bac.**	
TX Freq.	300 MHz	1.85 MHz	1.5 GHz	2.4 GHz	2.4 GHz	3.8 GHz	3.8 GHz	**915 MHz**	**915 MHz**	
data-rate	1	0.5	1	N/A	12	24	24	**5**	**25**	Mbps
Range	0.6 mm	8.8 mm	0.6 mm	13 mm	60 m	1 m	20 m	**25 mm**	**>2 m**	
Comms power	n.r.	0	0	0	200	≥30[b]	30	**0.2**	**1**	mW
Energy/bit	n.r.	0	0	0	16,000	≥1,250[b]	1,250	**5.5**	**12.4**	pJ/bit
Test subject	Rat	Rat	Rat	Rat	Rat	NHP	NHP	**Bench/Human[c]**	**NHP**	

[a] Extrapolated from figure. Two-part system [b] Exact number not reported [c] EMG only was tested on human subject [n.r.]Not reported

Size

The systems developed in [12] and [13] are fully passive backscatter-based implants in the 1 mm^2-class. Although this class of implants demonstrates excellent form factor and power characteristics, size constraints do not allow for on-board stimulation and signal processing. We believe that the 1 cm^3 class devices are better suited for practical implanted BCIs, particularly for neural prosthesis. On the other hand, [7] developed a miniaturized implant that exhibits great form factor; however, as noted below, data-rate and neural sampling rate are lacking; so, the implant does not have stimulation capabilities. The reduced form factor also has a detrimental effect on the communication range. The form factor of the external devices in the prior art are comparable to the one developed in the course of this thesis.

Power Consumption for Communication

The advantages of using backscatter communication versus active RF transmission are quite evident; the communication modules of the devices that utilize backscatter consume 0 (for passive systems) to 1 mW in our work. On the other hand, [29, 28] and [27] utilize an active VCO for transmitting FSK signals and consume between 30 mW to 200 mW of power, i.e., 30 to 200 times higher than the ones in our work. Similar benefits can be measured with respect to the energy expenditure per bit. The backscatter communication systems developed for this work consume up to 100 times less energy per bit transmitted.

Communication Range

Amongst the fully implanted systems, the ones in our work [30] demonstrated the longest communication range. This is due to the utilization of a dual-band architecture with WPT to leverage good power efficiency in low frequencies and communication in higher frequencies to take advantage of the higher available bandwidth. Therefore, our device powers up in increased implant depths, unlike inductive links, and can communicate at an increased data-rate at the same time.

However, the tradeoff with backscatter communication and range is more prominent in external systems. The longest range is 60 m, reported from the external system that Szuts et al. [27] developed for mice. On the other hand, our BCI for NHPs described in [31] is limited to a communication range of less than a meter. It is important to note, however, that the system was designed, optimized, and tested inside a reverberant cavity with a much more challenging channel than free

space. Moreover, higher communication ranges were not required for the application that it was developed for.

Data-rate

The combination of high data-rate with low power is one of the novelties of this work. Among fully implanted systems, our work demonstrates an increase in data-rate up to five-times when compared to those in prior art. This allows for the implementation of a higher channel count and higher sampling rates. Notably, though work in [6] records from 64 channels, it is confined to only 1 ksps sampling rate, which is 20 times lower than the ones in this work. Finally, our work exhibits similar data-rate performance with active radio systems. In particular, HermesD, developed by Miranda et al., achieves a data-rate of 24 Mbps, while our work outperforms that system by achieving data-rates up to 25 Mbps.

1.3 Contributions

1.3.1 Original Contributions

This work developed fully integrated systems that demonstrate both the feasibility and the benefits of backscatter communication in a suite of BCI applications. Our original contributions can be summarized as follows:

1. Design and fabrication of a μ-power frequency translation interface for bio-signals to extend the frequency response of bio-recording systems. The interface enables new capabilities, such as the implementation of ECoG with ICs, which would otherwise be unusable for these purposes.

2. The first demonstration of a USRP-based backscatter communication testbed for the demodulation of backscattered signals from implantable devices with capabilities of real-time demodulation at 6.25 Mbps and offline demodulation at 25 Mbps.

3. The first demonstration of a complete backscatter-based implantable system operating at a data-rate of 5 Mbps or greater, including an off-the shelf external system HF WPT with 47% efficiency, which offers real-time recording of 10 neural and 4 EMG channels from a circular implant that measures 25 mm in diameter and consumes 1.06 mW.

4. A first-of-its-kind fully integrated wideband UHF DQPSK backscatter communication system designed for operation in reverberant cavity animal cage environments.

5. Design and implementation of a UHF backscatter communication RF interface that provides a self-jammer cancellation of 90 dB, 10 dB higher than similar systems in the extant literature.

6. A first-of-its-kind statistical characterization approach in the self-jammer cancellation system.

7. *In-vivo* measurements of neural data from an anesthetized NHP demonstrating the feasibility of the wireless BCI described in Chapter 4 to capture neural spikes at a rate of at least 20 ksps.

8. Complete integration of a backscatter modulator with the Neurochip 3 for data-rates up to 25 Mbps and a power consumption of less than 5 mW.

1.3.2   List of Publications

All publications to date are included below.

[1] **E. Kampianakis**, A. Sharma, James Rosenthal and M. S. Reynolds "Wideband UHF DQPSK backscatter communication in reverberant cavity animal cage environments", in *IEEE Trans. Antennas Propag., Special Issue on Wireless Healthcare Biotechnology* (Accepted).

[2] **E. Kampianakis**, A. Sharma, J. Arenas and M. S. Reynold, "A dual-band wireless power transfer and backscatter communication approach for real-time neural/EMG data acquisition," in *IEEE Journal of Radio Frequency Identification*, vol. 1, no. 1, pp. 100-107, March 2017.

[3] **E. Kampianakis**, A. Sharma, J. Arenas and M. S. Reynolds, "A dual-band wireless power transfer and backscatter communication approach for implantable neuroprosthetic devices," in *Proc. IEEE International Conference on RFID (RFID)*, Phoenix, AZ, 2017, pp. 67-72. **Best Poster Award, Best Paper Nomination.**

[4] **E. Kampianakis** and M. S. Reynolds, "A biosignal analog front-end leveraging frequency translation," in Proc., IEEE SENSORS, Glasgow, 2017, pp. 1-3.

[5] X. Fu, A. Sharma, **E. Kampianakis**, A. Pedross-Engel, D. Arnitz and M. S. Reynolds, "A low cost 10.0-11.1 GHz X-band microwave backscatter communication testbed with integrated planar wideband antennas," in *Proc., IEEE International Conference on RFID (RFID)*, Orlando, FL, 2016, pp. 1-4.

[6] A. Sharma, **E. Kampianakis**, and M. S. Reynolds, "A dual-band HF and UHF antenna system for implanted neural recording and stimulation devices," *IEEE Antennas Wireless Propag. Lett.*, vol. 16, pp. 493–496, Jun 2016.

[7] J. Rosenthal, **E. Kampianakis**, A. Sharma and M. S. Reynolds, "A 6.25 Mbps, 12.4 pJ/bit DQPSK Backscatter Wireless Uplink for the NeuroDisc Brain-Computer Interface," in *Proc. IEEE Biomedical circuits and systems conference (BioCAS)*, Cleveland, OH, 2018.

[8] J. Rosenthal, **E. Kampianakis**, A. Sharma and M. S. Reynolds, "A 25 Mbps, 12.4 pJ/bit Backscatter Data Uplink for the NeuroDisc Brain Computer Interface," in *IEEE Trans. Biomedical circuits and systems (TBioCAS)* (submitted).

1.3.3   Thesis Organization

The rest of this thesis is organized as follows: Each chapter represents a significant published accomplishment, and, collectively, they describe the development of novel brain computer interfaces that utilize backscatter communication to record brain signals with low power, small size, and high data-rate. Chapter 2 describes the first project that was conducted in the course of this dissertation. In particular, it concerns a BCI capable of frequency-translating the ECoG signals so that the existing biorecording infrastructure may be reused. During this project, we researched the nature of neurons as signal generators (impedance, frequency of operation, etc.) and developed the tool foundation for the BCIs that were consequently developed through the rest of this work. Chapter 3 develops a fully integrated implantable BCI for the recording of action potentials and EMG signals. The BCI employs a dual-band architecture for interfacing wireless power transfer and communication on a miniaturized implant board as well as a low-cost high data-rate receiver. Chapter 4 describes the development of a backscatter communication interface for the Neurochip 3 in order to enable neural plasticity experiments in freely behaving animals in their home cage. Chapter 5 describes a novel mixed signal approach for a self-jammer cancellation system that achieves the highest isolation among the prior art. Finally, Chapter 6 concludes this thesis and presents the proposed future work.

Chapter 2

μ-POWER ECOG SIGNAL FREQUENCY TRANSLATION

This chapter is a modified version of the work presented in [32]

2.1   Introduction

There are several challenges associated with ECoG measurements [8, 7]. ECoG signals typically occupy the frequency range of $0.5 - 100$ Hz, with amplitudes of $10 - 100$ μV. Large DC offsets on the order of a few mV are often present due to electrochemical effects at the brain-electrode interface [7, 33, 34]. Implanted recording devices are generally low-power devices with a low supply voltage (often less than 2 V) and correspondingly limited voltage headroom. Given the high gain required (i.e. > 40 dB), any DC offset needs to be mitigated in order to avoid amplifier clipping. Furthermore, ECoG electrodes have high impedances of $1 - 2$ MΩ or more, so the input impedance must be very high to avoid loading the electrode voltage, while still maintaining a high common mode rejection ratio (CMRR) of at least 80 dB [33]. The spectrum of the ECoG signal varies significantly with brain activity. For example, for sleep monitoring, alpha ($7.5 - 14$ Hz), beta ($14 - 40$ Hz), gamma (> 40 Hz), and delta ($0.5 - 4$ Hz) waves are of interest. On the other hand, integrated circuit (IC) designs are normally optimized for a single transfer function [35, 23] (e.g $12 - 1630$ Hz [23]) and fixed at the time of manufacturing.
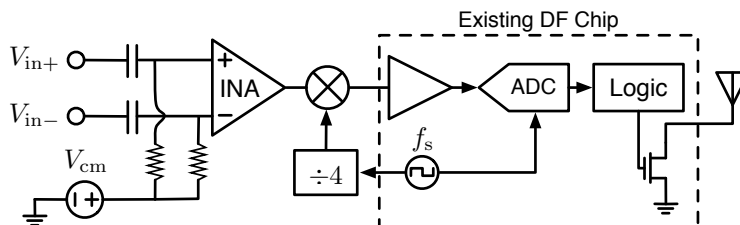

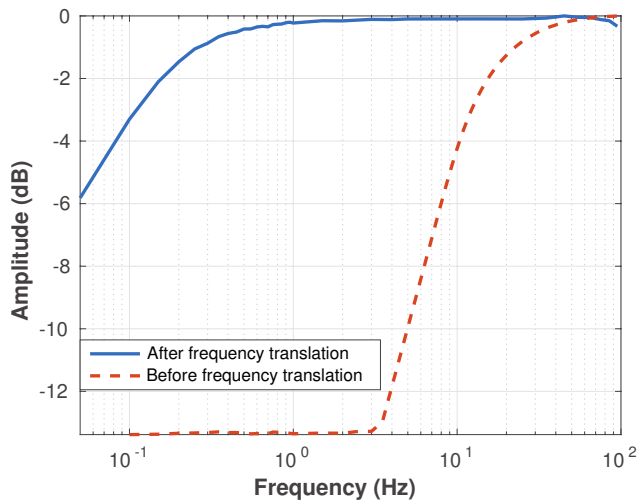**Figure 2.1:** Schematic of the proposed ECoG recording device.

Figure 2.2: Comparison of spectral response before and after frequency translation.

Since it is impractical to redesign existing ICs for each spectral response of interest, a method for changing the passband response of existing neural recording devices is highly attractive. This work approaches this problem by utilizing superheterodyne frequency mixing of the input neural signal after alternating current (AC) coupling and amplification.

As depicted in Fig. 2.1, the up-converted signal is sampled by an existing infrastructure IC that was initially developed for neural recording in dragonflies [23]. The IC has a passband of $12 - 1630$ Hz and will herein be referred to as the DF chip (abbreviation for dragonfly). In this work, front-end frequency translation is used to extend the DF chip low frequency cutoff from 12 Hz down to 0.5 Hz. Fig. 2.2 depicts the measured frequency response of the sensor before and after the frequency translation. The low side -3 dB cutoff has been extended from 12 Hz down to 0.15 Hz, enabling new applications such as ECoG sleep monitoring, which wouldn't have otherwise been feasible with this IC.

2.2 System Design

2.2.1 Existing Biorecording Infrastructure

The existing DF chip [23] is equipped with 2 DC amplifiers and 14 differential biopotential amplifier inputs as well as an 11-bit analog-to-digital converter (ADC) for signal digitization. It is clocked with a 20 MHz external quartz crystal. The chip is equipped with an RF power harvester that is
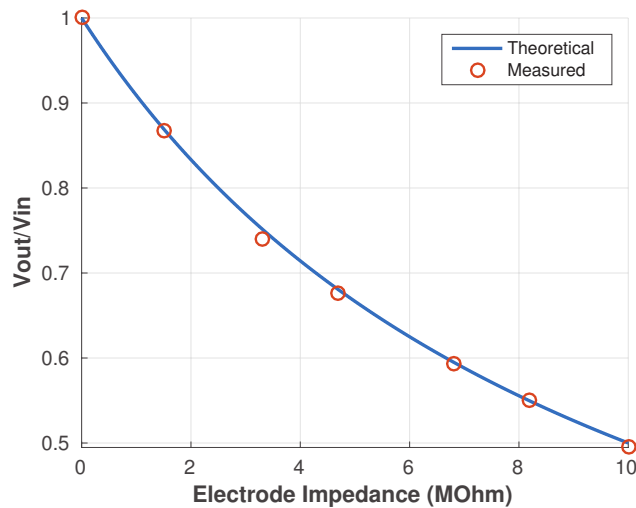
Figure 2.3: Input attenuation as a function of the electrode impedance; the theoretical voltage divider equation matches the measured response.

implemented with a 4-stage Shottky diode voltage multiplier. The output of the power harvester is connected to a low dropout regulator (LDO) that generates a 1.23 V power supply. The digitized inputs are Hamming(16,11)-encoded and backscattered to the external device with a rate of up to 5 Mbps using a binary shift keying (BPSK) modulation scheme.

2.2.2 Frequency Translating Front-End Design

To extend the low cutoff frequency of one channel of the DF chip, a frequency translating front-end was implemented using discrete components. Two 10 μF capacitors provide AC coupling in order to mitigate the DC offset from the electrodes, which can be up to a few hundred mV. Two 10 MΩ resistors provide a DC bias path for the amplifying stage and are also connected to a μ-power 0.4 V voltage reference (LT6650) that provides a common mode reference. The input resistors set the input impedance to 10 MΩ and realize a high-pass filter (HPF) with the AC-coupling capacitors that have a cut-off frequency of 0.15 Hz. Moreover, the input signal is subject to attenuation due to the voltage divider that is formed between the electrode impedance and the 10 MΩ resistors. Fig. 2.3 depicts the input attenuation as a function of the electrode impedance. One can observe that the theoretical voltage divider equation matches the measured response.

For the first amplifying stage, an Analog Devices AD8236 instrumentation amplifier (INA) was

utilized. This amplifier was selected due to its very low quiescent current consumption (40 μA), low noise (5 μVpeak at $0.1 - 10$ Hz), and low nominal operating voltage of 1.8 V. The INA is powered by a 1.23 V LDO output from the DF chip, and its reference input is driven by the 0.4 V voltage reference. The AD8236 is available in a tiny 1.57×2 mm wafer level chip scale package (WLCSP). The output of the amplifier V_{out} is as follows:

$$V_{\text{INA}} = G_{\text{INA}}(V_+ - V_-) + V_{\text{ref}}, \tag{2.1}$$

where G_{INA} is the amplifier gain, which is set by a single resistor to 50 V/V, V_+ and V_- are the voltages at the positive and negative inputs respectively, and $V_{\text{ref}} = 0.4$ V is the voltage at the "reference" terminal.

The output of the INA is connected to a frequency mixer that is implemented using the Intersil ISL43L220 μ-power *dual* single-pole/double-throw (SPDT) switch. One input of the first SPDT is connected to ground while the other is connected to the output of the INA. The control port of the switch is connected to a 407 Hz square wave signal. The latter is generated by a divide-by-4 clock divider circuit clocked by the 1628 Hz sampling clock (F_s) of the DF chip. The output of the first switch is an amplified biosignal modulated with a square wave as

$$V_{\text{sw+}} = V_{\text{INA}} \cdot \Pi(F_{\text{s}}/4), \tag{2.2}$$

where V_{INA} is given in (2.1) and $\Pi(F_{\text{s}}/4)$ is the square wave with a frequency $F_{\text{s}}/4 = 407$ Hz. The second SPDT of the ISL43L220 is used to modulate the $V_{\text{ref}} = 0.4$ V signal that drives the reference terminal of the INA. Hence, the second output of the switch is as follows:

$$V_{\text{sw-}} = V_{\text{ref}} \cdot \Pi(F_{\text{s}}/4). \tag{2.3}$$

The differential signal formed by $V_{\text{sw+}}$ and $V_{\text{sw-}}$ is connected to one of the input channels of the DF chip, so the common mode voltage output, V_{ref} of the INA, is subtracted at the DF chip's built-in amplifier, resulting in a final output, V_{DF}, which is given as:

$$V_{\text{DF}} = G_{\text{DF}} \ (V_{\text{sw+}} - V_{\text{sw-}}) \tag{2.4}$$

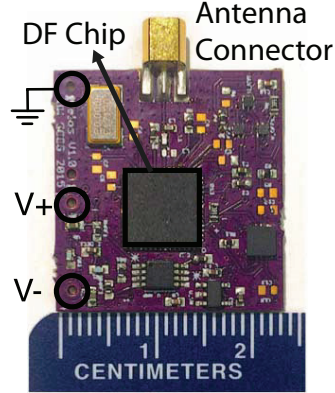$$= G_{\text{tot}} \ (V_+ - V_-) \ \Pi(F_{\text{s}}/4), \tag{2.5}$$

Figure 2.4: The prototype biosensor board (25 mm×23 mm×3 mm).

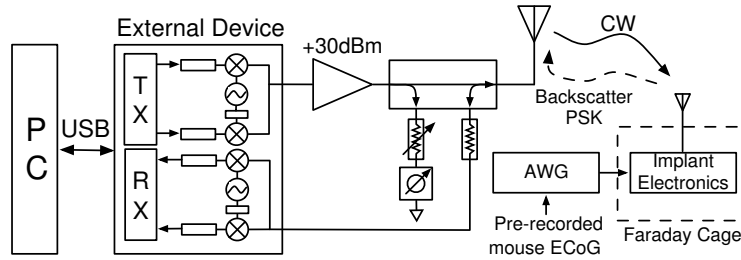**Figure 2.5:** Test setup for recording system.

where $G_{\mathrm{DF}} = 50$ V/V is the gain of the input amplifiers on the DF chip and $G_{\mathrm{tot}} = 2500$ V/V is the end-to-end gain of the system.

The sensor was fabricated on a 25 mm x 23 mm x 3 mm FR4 substrate, as depicted in Fig. 2.4. Its measured power consumption is 1.06 mW, which includes the front-end frequency translation. The front-end consumes just 56.6 μW, representing only 5.3% of the overall system power consumption.

2.2.3 External System Design

An external system similar to the one presented in [30] was utilized, as shown in Fig 2.5. An external power amplifier feeds RF power from a National Instruments USRP B210 software-defined radio to the external system antenna at up to +30 dBm. The output of the amplifier is connected to a self-jammer cancellation circuit [36]. The RF signals are downconverted to baseband using
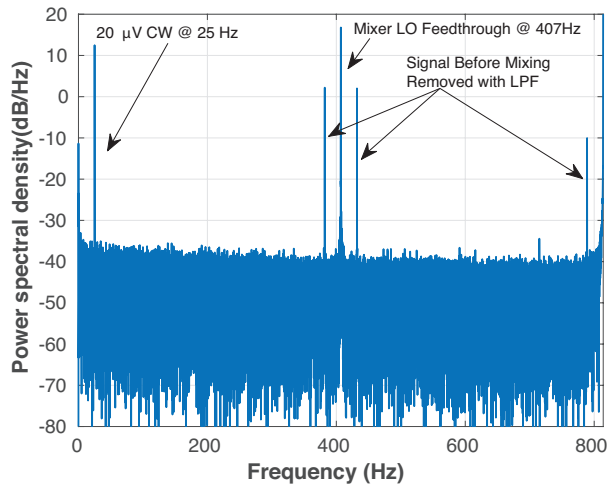
Figure 2.6: Left: The spectrum of a 20 μV sinusoid at 25 Hz after coherent digital down-conversion but before digital filtering.

a National Instruments USRP B210 and GNUradio and Matlab scripts that demodulate and de-interleave the packetized data. A more thorough description of the external system is provided in Chapter 3.

The original waveform is recovered using coherent digital downconversion simply by multiplying the telemetered signal with a pulse train of 407 Hz. As the mixer and the sampling clock are both derived from the same crystal oscillator, the harmonics that are produced from the modulation all fold to the same frequency bins so that there is no unwanted phase/amplitude drift. However, there is a residual local oscillator (LO) feedthrough at $F_\mathrm{s}/4$ that is caused by transient effects (charge injection at the SPDT switches) and a modulation of the offset voltage during switching. This can be filtered out with finite impulse response (FIR) low-pass filtering (LPF). Fig. 2.6 depicts the spectrum of a 20 μV sinusoid at 25 Hz after downconversion and before filtering.

2.3 Bench-top Experimental Results

The recording device was characterized in a custom Faraday cage to mitigate spurious coupling from unwanted sources (e.g. 60 Hz power line noise). An arbitrary waveform generator with its outputs connected to a resistor network that emulates the electrode impedance was utilized in order to feed the sensor with test signals.
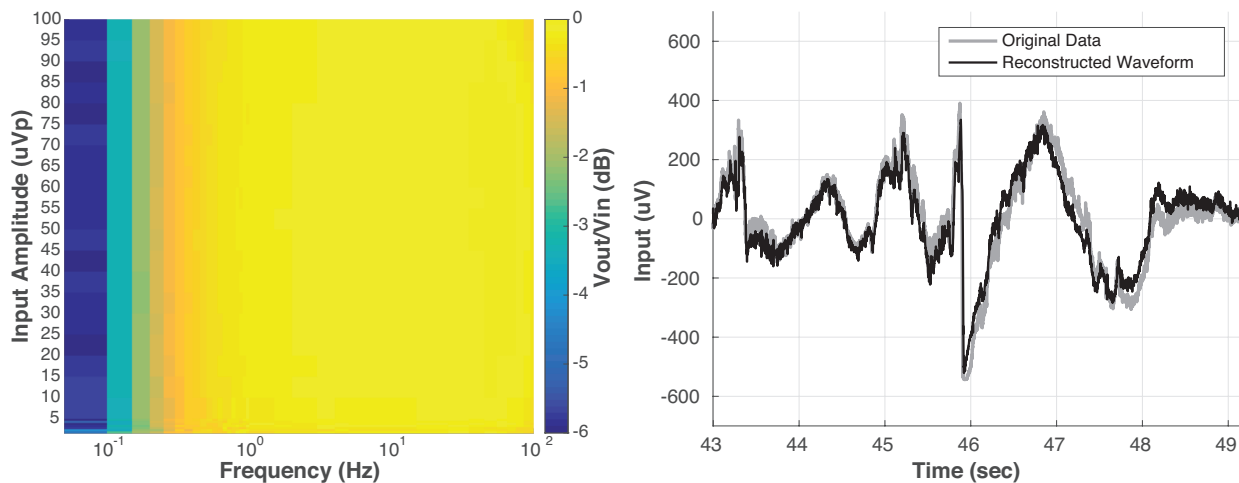
Figure 2.7: Left: Amplitude linearity over a frequency range of $0.1 - 100$ Hz and over an amplitude range of $1 - 100\mu$ Vpeak. Right: Comparison of the pre-recorded mouse ECoG signal to the reconstructed waveform after frequency translation.

To characterize the linearity of the system, a sinusoid with amplitude ranging from 1 μV to 400 μV and a frequency of $0.05 - 100$ Hz was fed to the recording device. The amplitude was estimated with periodogram techniques, and the measurements verified the HPF cutoff frequency of 0.15 Hz. The results are depicted in Fig. 2.7-left, where it can be observed that the gain is flat to within 1 dB over the passband of $0.5 - 100$ Hz and over an amplitude of $1 - 300$ μV.

The input-referred low-frequency noise in different stages of the recording device was characterized by grounding the inputs of the interface. An RMS noise of 0.59 μV and 0.988 μV was measured at the output of the INA and the output of the mixer respectively. The added noise is due to the switching effects of the mixer. However, the 0.398 μV RMS is a negligible difference in noise levels for the ECoG.

For the characterization of the system in a simulated recording, the arbitrary waveform generator was loaded with 120 sec pre-recorded ECoG data from a mouse. A 6 s portion of the original vs. reconstructed waveform is depicted in Fig. 2.7-right. The total root mean square error (RMSE) is on the order of 41 μV, which is essentially identical to the DF chip's original noise performance. Commonly, the collected brain signals are analyzed in the frequency domain by inspection. Hence, spectrum reconstruction capability is of primary importance. Fig. 2.8 depicts the spectrograms of
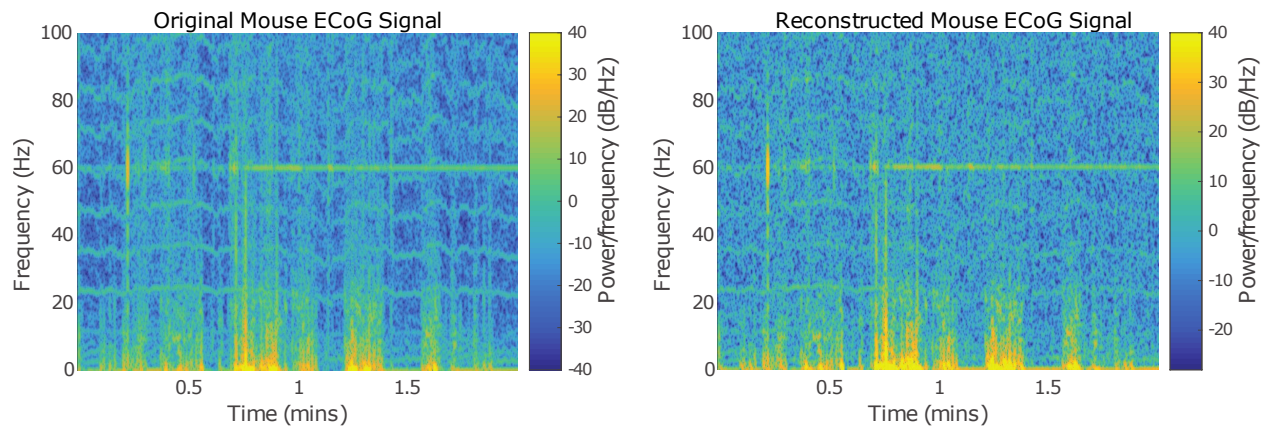
Figure 2.8: Left: spectrogram of a 120 sec ECoG signal from a mouse. Right: reconstructed signal using the developed biosensor.

the original and the reconstructed neural signals, wherein one can observe good agreement.

2.4   Conclusion

This chapter presents an approach for altering the frequency response of existing biosensor infrastructures in order to render them compatible in a broader range of applications. Particularly, an analog front-end that integrates an amplifying stage and a digital switching mixer in order to upconvert a low-frequency bio-signal to a higher spectrum band that is within the passband of the IC of interest was developed. After sampling the upconverted signal, the original signal can be reconstructed by utilizing synchronous demodulation in post-processing. To demonstrate the feasibility of the approach, a pre-recorded ECoG signal from sleeping mice, with a frequency range of $0.4 - 100$ Hz, was upconverted to an IF of 407 Hz and sampled using an existing IC that was originally developed for capturing neural signals from dragonflies. The original low frequency cutoff of 12 Hz was effectively reduced to 0.5 Hz and the signals were reconstructed with a minimal RMSE of 41 μV.

Chapter 3

5 MBPS BATTERY-LESS IMPLANTABLE COMMUNICATION SYSTEM

This chapter is a modified version of the work presented in [30]
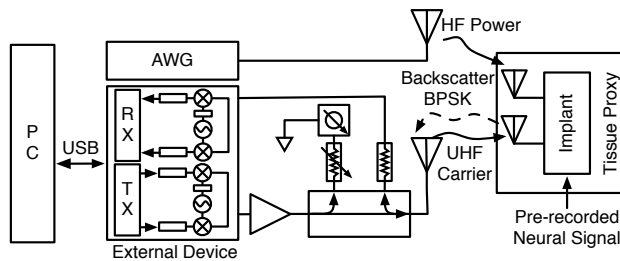
3.1 Introduction

Figure 3.1: High-rate implantable communication system testbed.

As mentioned at the introduction of this work, numerous research and industry teams are working to implement a new class of bioelectronic devices incorporating amplification, digitization, and wireless transmission of neural activity along with electrical and/or optogenetic stimulation of neurons. Despite promising early results, significant electronic, electromagnetic, thermal, and packaging challenges remain [25, 37]. In addition to the aforementioned communication challenges, efficient power delivery is also a significant issue, especially in chronic (long-term) implanted devices where battery exchange is undesirable. Wireless power transfer (WPT) using magnetic induction has been widely used for this purpose; many prior systems (including [38] and [39]) have shown high efficiency inductive WPT in the 13.56 MHz industrial, scientific, and medical (ISM) band.

An alternative WPT approach relies on near-field coupling of UHF energy; an integrated BCI system including both near-field UHF WPT and backscatter communication is described in [7, 25]. This work presents a 64-channel implantable neural recording system that uses the UHF band
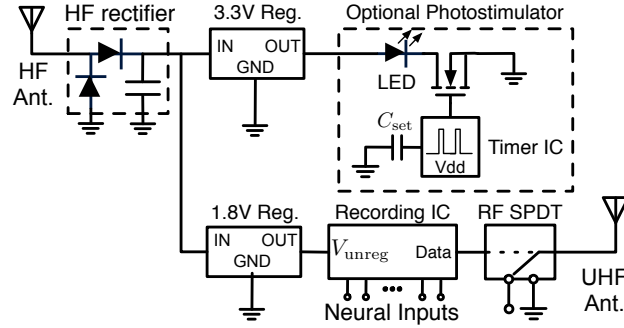
Figure 3.2: Implanted device schematic.

for both wireless power and backscatter communication. However, this system is limited to a communication rate of 1 Mbps and, thus, its sampling rate is confined to only 1 kHz per channel.

This work aims to combine high speed UHF modulated backscatter communication with efficient HF WPT in a single implantable system. The system is a combination of a custom implant device with a commercial low-cost software defined radio (SDR) platform serving as the external system. A block diagram of this system is shown in Fig. 3.1. The implanted device is powered by a 13.56 MHz WPT link and uplinks neural recording data at 915 Mhz using a binary phase shift keying (BPSK) backscatter modulator. The external SDR supplies a continuous wave (CW) carrier at 915 MHz and downconverts the backscattered signal to provide a host PC with baseband I/Q samples for software demodulation using GNUradio and MATLAB. An external self-jammer cancellation network suppresses the reflected carrier energy to greatly improve receiver sensitivity. To the best of our knowledge, this is the first demonstration of a complete backscatter-based implantable system operating at a data-rate of 5 Mbps or greater, which includes an off-the shelf external system, HF WPT, and offering multi-channel neural and electromyography (EMG) recording.

3.2 Implant design

A schematic of the envisioned implant is shown in Fig. 3.2. A dual-band antenna, described in [40], receives the incoming HF carrier, which is rectified and regulated to provide power to the implant. A previously developed neural/EMG recording integrated circuit (IC) [23] is used to digitize up to a total of 10 neural and 4 EMG inputs. The digital bit stream output from the recording IC drives an SPDT RF switch at the terminals of the UHF antenna to implement BPSK backscatter modulation.
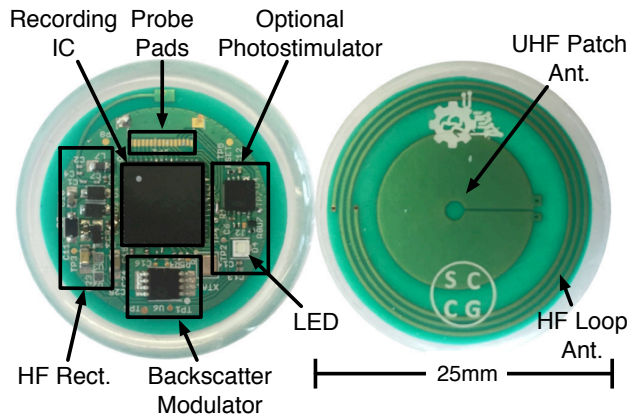
Figure 3.3: Implant prototype encapsulated in biocompatible silicone.

Additionally, the capability for optogenetic photostimulation is made available through pulse width modulation (PWM) of a blue light emitting diode (LED).

The antenna and the electronic components are encapsulated in a biocompatible silicone polymer (Dow Corning MDX4-4120). The encapsulation procedure uses centrifugation and vacuum curing to remove air bubbles and ensure a tight bond to the circuit. The implant prototype measures 25 mm diameter with a total thickness of 2.8 mm, which includes the substrate, antenna, all circuitry, and biocompatible silicone encapsulation, as depicted in Fig. 3.3.

3.2.1   Choice of Operating Frequencies

The 13.56 MHz HF industrial, scientific, and medical (ISM) band was chosen for the WPT application as it provides high coupling efficiency and low specific absorption rate (SAR) with a relatively small antenna size. The $902 - 928$ MHz UHF ISM band was selected due to the 26 MHz of bandwidth available and the readily available commercial hardware (e.g. the USRP platform) available in this band.

3.2.2   Dual-Band Antenna Subsystem

The implant antenna subsystem was previously described in [40]. The system contains a 25 mm diameter implant antenna, and an 85 mm diameter external antenna. The antenna system has been previously tested in a saline tissue proxy as well as *in vitro* animal tissue. The antenna structure and
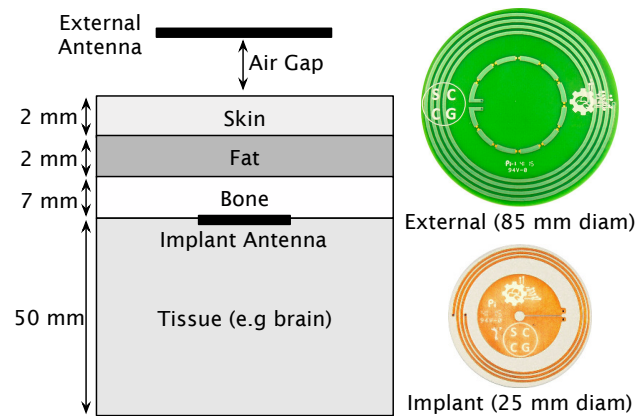
Figure 3.4: Implant antenna and layered tissue model used for simulations, from [40].

the layered tissue model used for full-wave electromagnetic simulation in CST Microwave Studio are shown in Fig. 3.4. In a saline tissue proxy, at an implant depth of 11 mm and an air gap of 5 mm, the measured HF power link efficiency is on the order of 17% and the insertion loss of the UHF communication link is on the order of 38 dB.

3.2.3   HF Wireless Power Transfer Receiver

A voltage doubling rectifier is used to convert the incoming HF WPT carrier at 13.56 MHz from the external system into DC power. The output of the rectifier is regulated using low-dropout (LDO) regulators to provide 3.3V and 1.8V rails. Significant effort was invested in component selection for small form factor, low power consumption, and over-voltage tolerance. Schottky diodes (1N5711, Diodes Incorporated) were selected due to their high reverse voltage rating of 70 V as well as their low forward voltage drop of 410 mV. Voltage regulators from the Texas Instruments (TI) LP5907 series were selected. A 3.3 V regulator powers the photostimulator and a 1.8 V regulator powers the recording IC. This regulator series was selected due to its package size of only 0.65 x 0.65 mm and low dropout voltage of 120 mV. Most importantly, these regulators have an unusually high measured power supply rejection ratio (PSRR) of approximately 20 dB at 13.56 MHz. This specification is critical in order to reduce the unwanted residual 13.56 MHz ripple coming from the rectifier. For most LDO regulators, the PSRR will be very high at frequencies within the loop bandwidth of the regulator (50 dB or more for frequencies up to e.g. 100 kHz), but the PSRR unfortunately decreases to near zero at frequencies of 1 MHz or above. In contrast, the measured high frequency
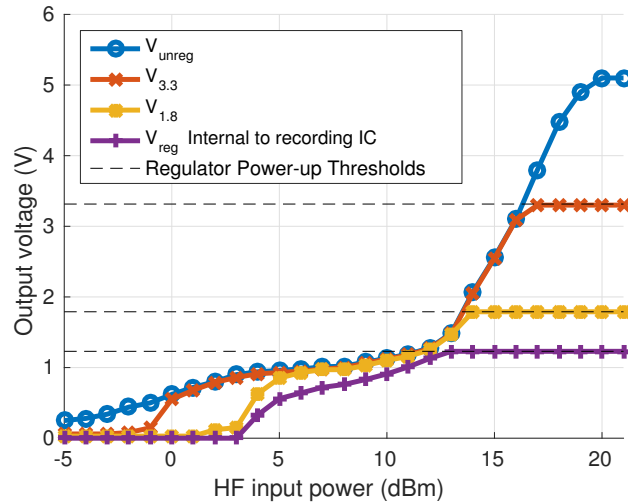
Figure 3.5: Regulator outputs vs HF input power. The implant powers-up at an input power of 13 dBm and the optional photostimulator circuit at 17 dBm.

PSRR of the LP5907 series is excellent.

In order to achieve maximum performance from the rectifier, proper matching to the antenna is necessary. The matching component values were calculated using the following procedure: the total dc power consumption of the system was measured and found to be 0.74 mA at 1.8 V (with the photostimulator disabled). A 2432 Ω load was therefore connected to the output of the LDO to emulate the system power consumption. The return loss (|S11|) at the rectifier input (prior to matching) was measured at 13.56 MHz over a range of input powers. The minimum |S11| value was used to calculate the corresponding components for a conjugate match. After matching, the rectifier exhibits 47% efficiency at this operating point. This is very close to the theoretical 50% efficiency that can be achieved with a conjugate match.

The HF WPT system was tested over different input powers in a saline tissue proxy with 1 cm implant depth and with the external antenna having an air gap of 0.5 cm. Fig. 3.5 depicts the output of the rectifier and the different board-level and chip-level supply voltages. The HF input power at the external antenna port for which the LDOs enter regulation are as follows:

- Recording IC, integrated 1.23 V LDO: +13 dBm.
- TI 1.8 V LDO: +14 dBm.
- TI 3.3 V LDO: +17 dBm.

Thus, a minimum HF drive power of +17 dBm must be supplied under these implant conditions.
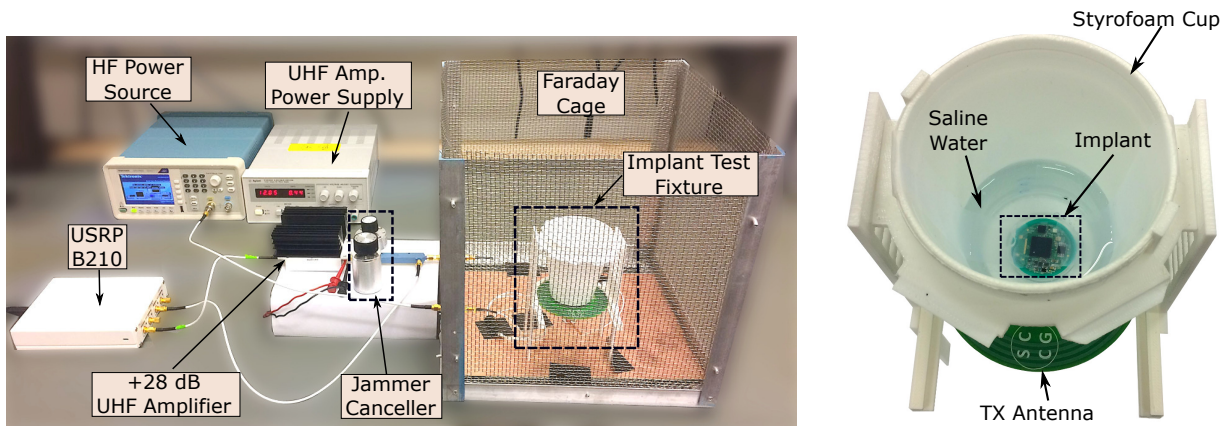
Figure 3.6: Left: Implanted communication system testbed. Right: 3D-printed fixture for varying the air-gap and implant depth.

A 5.1 V Zener diode is integrated into the rectifier circuitry (not shown in Fig. 3.2) to protect the implant from excess HF power.

3.3   External System

The commercial off-the-shelf (COTS) external system is depicted in Fig. 3.6. It is based on an Ettus Research, Inc. USRP B210, which is connected to an added RF front-end that consists of an additional power amplifier and a self-jammer cancellation subsystem.

3.3.1   Software defined radio subsystem

The USRP B210 is a low-cost ($1100) software-defined radio supporting carrier frequencies of $70 - 6000$ MHz and a baseband bandwidth up to 56 MHz. In our system, the USRP B210 is responsible for supplying the UHF communication carrier at 915 MHz and receiving the backscatter subcarriers containing uplink data from the implant. The USRP is connected to a PC with USB 3.0 to control the USRP and convey the baseband data to the PC. GNU Radio, an open source block-based signal processing software, was utilized. A custom GNU Radio flowgraph that sets up the USRP hardware at a baseband sampling rate of 20 Msps and processes the incoming I/Q symbols in real-time was designed.
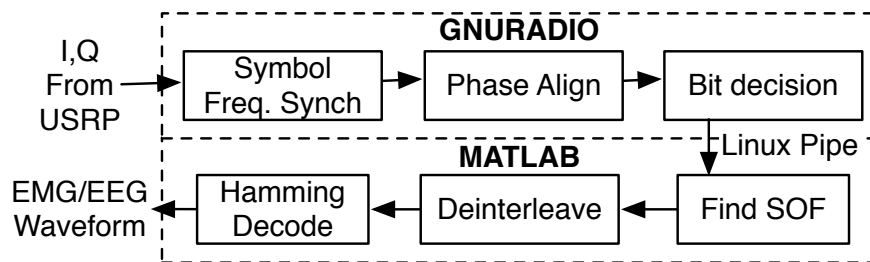
Figure 3.7: Proposed receiver pipeline

Fig. 3.7 depicts a simplified view of the proposed GNUradio receiver pipeline. First, a phase locked loop (PLL) exploits poly-phase filter banks [41] locks to the backscattered symbol frequency and downsamples accordingly. Next, another PLL that exploits the Costas-loop architecture [42] rotates the phase of the symbols onto the in-phase axis so that slicing can be implemented simply by checking the sign of each sample. Then, a bit decision block outputs a string of demodulated bits.

The PC that runs the demodulating software employs 16 GB of RAM and an Intel Core-i7 processor clocked at 3.8 GHz. For rates up to 1.5 Mbps, a Linux pipe can be utilized and the output of the flowgraph can be processed in near-real time from MATLAB using batch processing of 3000 frames at a time. At higher rates, a post-processing approach is used to circumvent the slow speed of MATLAB processing. Fig. 3.8 depicts an I/Q plot of 10000 samples that were collected after the phase alignment block. The symbols were generated at a rate of 5 Msps using the recording IC and then collected through the USRP-based external system.

The MATLAB script is responsible for post-processing the data generated by the GNU Radio flowgraph. Start-of-frame (SOF) synchronization is performed by correlating the Barker codes that are embedded in the data stream transmitted by the recording IC [23]. After frame synchronization, de-interleaving is performed to extract the 16-bit blocks containing the digitized neural/EMG data. The last step is a Hamming (16, 11) decoder that provides single error correction and double error detection (SECDED) functionality to extract the 11-bit neural/EMG samples.

3.3.2   RF interface

One of the challenges of backscatter communication systems is the reception and demodulation of the backscattered signals in the presence of a CW carrier (a self-jammer) that is typically much
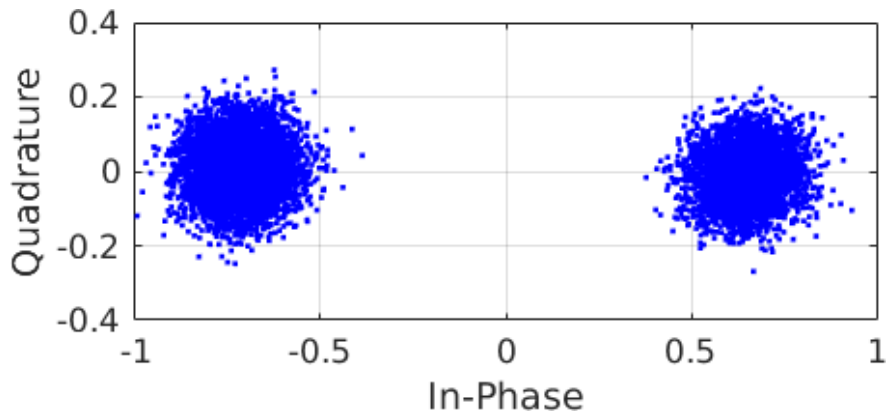
Figure 3.8: Measured I/Q samples after the phase-alignment PLL. The samples are synchronized in terms of symbol frequency and rotated in phase onto the in-phase axis.

stronger[43]. To address this challenge, numerous approaches to isolate the transmit and receive paths have previously been explored [36, 44, 45].

For the purposes of this work, we developed an RF interface that provides both amplification of the UHF CW as well as self-jammer cancellation; particularly, a Mini-Circuits ZRL-3500 amplifier increases the carrier power generated by the USRP up to +25 dBm. The output of the amplifier is connected to a self-jammer cancellation circuit, as shown in Fig 3.1. The latter comprises a Mini-Circuits ZX30-20-20BD+ 10 dB directional coupler, a Weinschel 980-2K variable phase shifter (having 100 degrees phase shift range) and a JFW 50R-019 1 dB step attenuator with 0-10 dB attenuation range. If the phase shifter and the attenuator is carefully adjusted, the signal that exits the output coupling port would contain the backscattered signal, with a carrier suppression of up to ≈ 39 dB, as shown in Fig. 3.9. Similar directional coupler-based self-jammer suppression networks can be found in [44, 46]. This system is a straightforward static self jammer cancellation system with just 2 components (the variable phase shifter and the variable attenuator). In Chapter 4, we present a more sophisticated self-jammer cancellation system with digital control that provides much better performance at the cost of increased complexity.

To provide the HF carrier that powers the implant, an Agilent 3350B arbitrary waveform generator (AWG) was utilized. The output HF carrier at 13.56 MHz can be provided with a power of up to +23 dBm, but as previously described, only +17 dBm is required at an 1 cm implant depth, with the external antenna having an air gap of 0.5 cm.
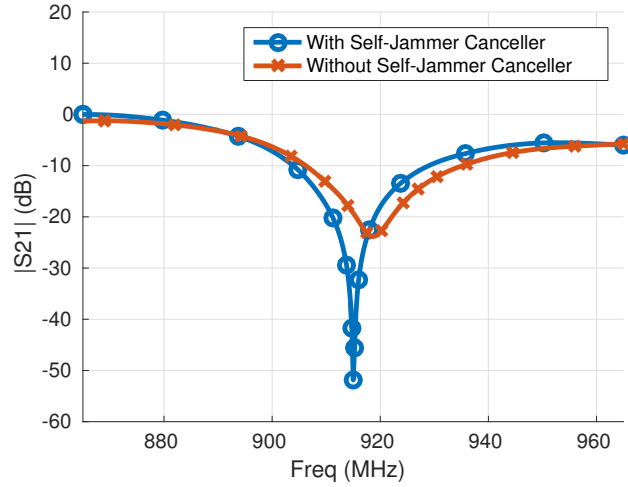
Figure 3.9: Measured self-jammer carrier suppression ratio with and without the self-jammer cancellation circuit. The self-jammer canceller reduces the carrier amplitude by $\approx$ 39 dB.

3.4 Measurement Results

As shown in Fig. 3.6, benchtop testing employs a 3D-printed fixture, allowing the adjustment of the air gap between the external antenna and the saline tissue proxy (0.91% w/v saline solution). The transmit antenna is placed beneath a styrofoam cup that contains the saline solution, and this fixture is placed in a Faraday cage in order to shield the experiment from external interference.

3.4.1 Sensitivity/Range characterization

To characterize the performance of the backscatter communication link, a benchtop setup with an air gap of 0.5 cm, an implant depth of 1 cm, and a saline water height of 6 cm was utilized. The in-channel power of the backscattered subcarrier was first measured with a spectrum analyzer at the output-coupled port of the directional coupler. With a +25 dBm carrier power from the external system, the received channel power was measured and found to be −40 dBm under the test conditions.

Variable attenuation in the receive path was used to reduce the available subcarrier power to measure the receive path link margin caused by the receiver's internally generated noise. Packet
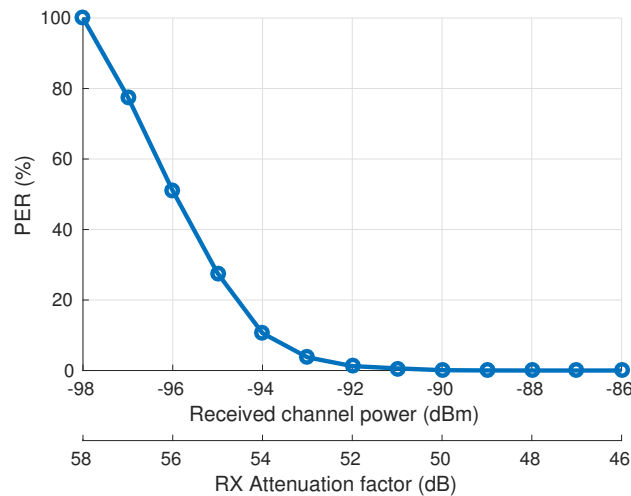
Figure 3.10: Packet error rate vs. receive-path attenuation factor and corresponding absolute channel power.

error rate (PER) measurements were first made as a function of the available channel power by counting cyclic redundancy check (CRC) errors, after Hamming decoding from 25000 packets for different RX attenuation factors. Fig. 3.10 shows the corresponding results. The receiver exhibits a PER of under 0.62 % for an input channel power of -91 dBm.

The system was also characterized for PER as a function of implant depth. In this experiment, the externally supplied carrier power was set to 0 dBm, and the PER was measured using the same method by which the implant depth was varied, with a fixed air gap of 0.5 cm. Fig. 3.11 depicts the corresponding results. We observed that the backscatter uplink exhibits a PER of better than 0.19 % at an implant depth of up to 3 cm. Lower carrier power is better for reducing the specific heat absorption rate (SAR) and the system's overall power consumption. Hence, a carrier power of 0 dBm was utilized for this experiment since it yields a sufficient implant depth. It is important to note that the time-domain simulations provided a peak UHF SAR value of 0.457 W/kg averaged over 1 g of mass [40]. This peak SAR value is 3.5 times lower than the regulatory limit of 1.6 W/kg.

3.4.2 Measured frequency response of neural/EMG channels

The neural/EMG recording IC [23] supports up to 10 neural and 4 electromyogram (EMG) channels with a sampling rate of 26.10 kHz for the neural channels and 1.628 kHz for the EMG channels.
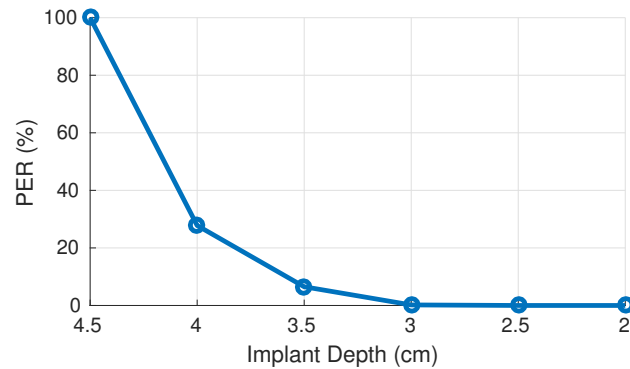
Figure 3.11: PER vs implant depth with a fixed UHF carrier power level of 0 dBm.

The EMG and the neural inputs are high-pass filtered at 5 Hz and 250 Hz respectively. Their frequency response was characterized by injecting a sinusoidal test signal at the input. Fig. 3.12 depicts the measured system response for the neural and EMG inputs.
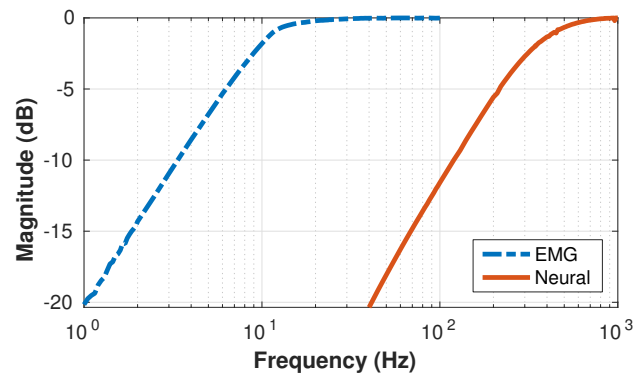

Figure 3.12: Measured frequency response of neural and EMG inputs.

3.4.3 Neural/EMG Measurements

The end-to-end acquisition and telemetry of neural and EMG signals were also characterized using the *in vitro* test setup. Pre-recorded electromyogram (EMG) and neural signals signal were fed into the implant from an Agilent 33500B arbitrary waveform generator (AWG) using an electrode simulator network and a high impedance attenuator.
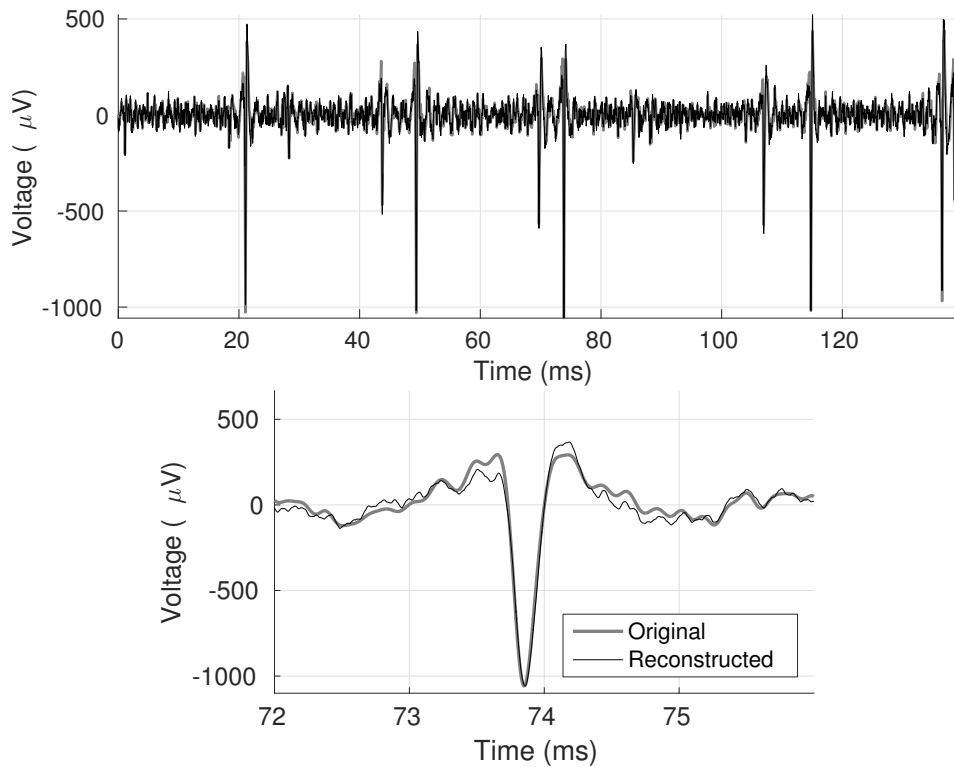
Figure 3.13: Original vs. reconstructed neural signal. Left: complete reconstructed and original waveforms. Right: zoomed-in depiction of one of the spikes that occur at approx. 74 ms

The testing of neural inputs used prerecorded neural signals that were acquired from the motor cortex of a non-human primate by our colleagues under an IACUC approved protocol. A total of 130 ms of data were captured from the forearm area of left primary motor cortex of a monkey Macaca nemestrina. The monkey was implanted with a Utah microelectrode array [9], and the signals were captured and digitized using the Neurochip platform [19] at a sampling rate of 21 kHz. This pre-recorded signal was filtered with a passband of 500-7000 Hz and loaded into the AWG for subsequent playback.

The proposed system was set up with the receiver recording in real time and the implant powered by HF wireless power. An implant depth of 1 cm and an air gap of 0.5 cm were used. A comparison between the pre-recorded signal and the signal obtained from the proposed system is seen in Fig. 3.13. The time domain representation of the entire 130 ms of data is plotted on the left
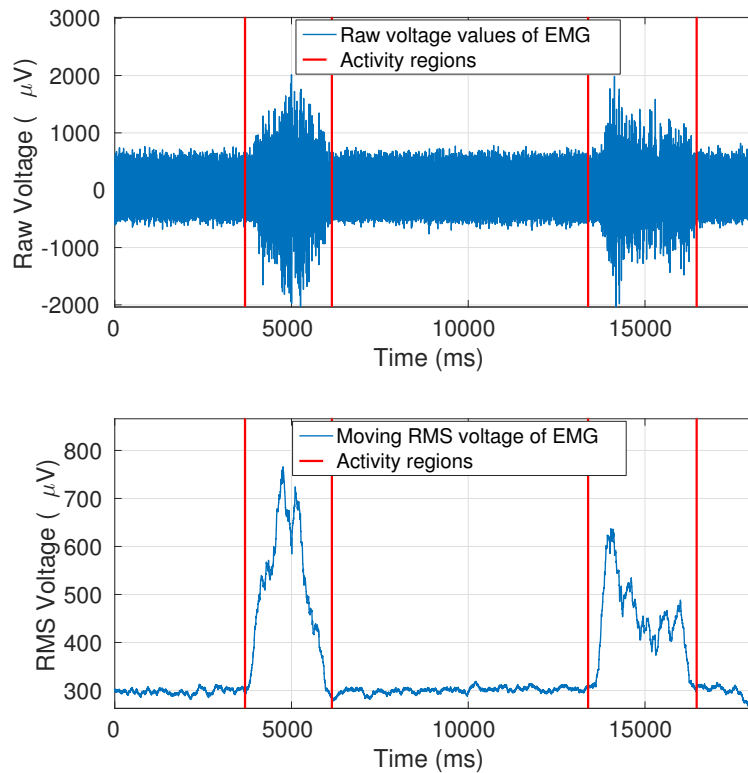
Figure 3.14: Measurements of the bicep brachii muscle activity on a human subject using one of the proposed system's EMG channels. Top: Raw EMG voltage values. Bottom: Post-processed data using a moving RMS filter with a window duration of 300 ms.

side of the figure, while on the right, a zoomed-in view depicts a single spike. Excellent agreement is observed between the two waveforms.

Lastly, the capability of the proposed system for detecting muscle activity was tested. For this experiment,the terminals of one of the EMG amplifier inputs were connected to commodity EMG electrodes. The electrodes were placed in adjacent positions on the left bicep brachii area of a human subject. Moreover, a reference electrode was placed below the wrist flexor of the subject and connected to the implant's ground. The proposed system was powered over the HF link and the receiver was set up to demodulate data in real-time for a total of 18 seconds. After initiating the recording, the subject was instructed to contract their muscles for 1 second at time intervals of 4 and 14 seconds.

The corresponding results are depicted in Fig. 3.14. The time periods during which the subject

contracted their muscles are designated with vertical red lines. The top part of the figure depicts the raw EMG voltage values. Spikes with amplitudes of up to 4 mVpp can be observed during the periods of muscle activity. EMG signals are typically processed using a moving RMS filter [47] in order to reduce high frequency noise and smooth the inherently spiked data. The bottom part of Fig. 3.14 shows the results of a moving RMS filter with a window duration of 300 ms applied on the raw data. After filtering, especially, muscle activity can be identified with excellent clarity.

3.5   Conclusion

This chapter presents a dual-band approach for HF wireless power delivery and UHF backscatter communication in implanted biomedical devices. A testbed, including a custom implanted device, as well as an external system based on a commercially available USRP B210 software defined radio (SDR) platform is presented. The implant integrates a BPSK backscatter uplink rate of 5 Mbps with an HF WPT link, delivering 1.33 mW at an efficiency of 47%. The implant, including the printed circuit substrate, dual-band antenna, all circuitry, and biocompatible silicone encapsulation, is 25 mm in diameter and 2.8 mm thick. It supports up to 10 neural and 4 electromyogram (EMG) channels with a sampling rate of 26.10 kHz for the neural channels and 1.628 kHz for the EMG channels. The communication link is shown to have 0% packet error rate at an implant depth of up to 2.5 cm.

Chapter 4

HIGH DATA-RATE UHF DQPSK BACKSCATTER COMMUNICATION FOR BCIS OPERATING INSIDE ANIMAL CAGES

This chapter is a modified version of the work presented in [31]

4.1 Introduction

The recording of neuronal activity in freely behaving monkeys has played a critical role in deciphering the complex processes in their motor cortex [48]. Significant amount of research has demonstrated correlations between the frequency of action potential firing to specific movement patterns [10, 49, 50, 51]. Most, if not all, of these experiments were conducted in a setting where the non-human primate (NHP) subject was placed in a seated position and, generally, with its movement constrained. Restraining the NHP facilitated the use of tethered equipment, reduced the noise of neural recording, and enabled a higher degree of control in the behavioral experiments while preventing the NHP from damaging the equipment or hurting itself. Unfortunately, restraining the subject may potentially lead to erroneous results and assumptions [10, 52, 53]. It is important to note that unrestrained experimentation with freely moving animals is an invaluable tool for unraveling the complex connections between electrophysiological response and motor control. Therefore, a BCI that is capable of telemetering electrophysiological digitized signals from multiple neuronal sites with sustained operation over multiple days will be an invaluable tool for enabling neuroscience research experimentation in animals that behave freely inside their cage [54, 19, 55, 56].

4.1.1 The Neurochip BCI

We present the development of an assembly that was developed to provide the Neurochip 3 (herein referred to as NC3) with wireless high data-rate backscatter communication capabilities. The NC3 is the latest version of the BCI that was developed by Zanos et al. in [19] and is employed for brain recording and stimulation in NHPs. The NC3 is depicted in Fig. 4.1 where one can observe
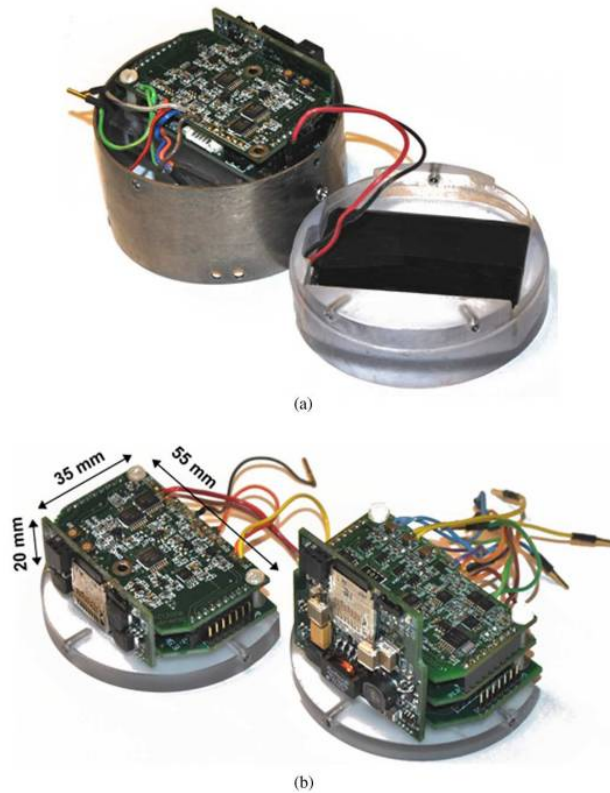
Figure 4.1: The Neurochip BCI: a) The circuitry is contained in a $35 \times 55 \times 20$ mm titanium tube and sealed with a Teflon cap. The whole device is installed on top of the NHP's skull. b) Circuitry of the NC3.

that the circuitry is contained in a 35×55 mm titanium tube that is sealed with a teflon cap. The complete setup including the case is installed on top of the subject NHP skull and is secured in place using surgically implanted titanium screws. The NC3 is powered by a 13 Wh battery pack and can record up to 64 neural channels at a sampling rate of up to 20 ksps and with 16 bits resolution, using an RHD2132 IC. Moreover, it stores the neural data in an SD card for post processing and incorporates an optical link that can communicate at a few kbps over a very close range (a few cm). The optical link is used for uploading settings and observing a single channel of neural data.
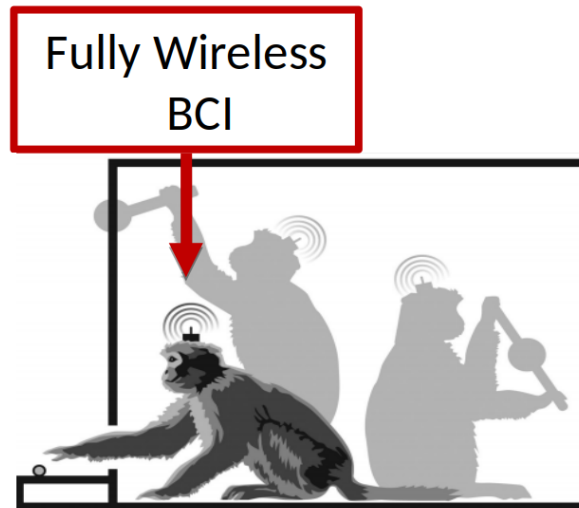
Figure 4.2: Problem sketch: the development of the wireless NC3 will allow uninterrupted experimentation on a freely moving animal inside its home cage. Figure credit Gregory Moore.

4.1.2 Problem statement

Neuroscientists have been using the NC3 for neuroscience research experiments and have presented significant findings. For example, Moritz et al. demonstrated a direct control of paralysed muscles by cortical neurons in NHPs [57] and McPherson et al. demonstrated that targeted, activity-dependent spinal stimulation produces long-lasting motor recovery in chronic cervical spinal cord injury [58]. However, the NC3 comes with significant limitations. Every time the neuroscientists need to extract data from the SD card or charge the battery, they have to sedate the monkey and interrupt the experiment. As a result, experiments that should ideally last for many days can only last for a few hours. Moreover, there is no way for validating the good functionality of the setup after it has been installed on the NHP and the experiment has already started. This often results in a failure of the experiment due to some error in the NC3 software, a bad connection, or other problems. These limitations significantly limit experimentation and, therefore, upgrading the NC3 with wireless charging and wireless low-power communication will be invaluable for neuroscience research.

As sketched in Fig. 4.2, what we developed in this work is a high data-rate communication

interface for the NC3 so that the NHP can freely behave inside its home cage while the BCI records its neurophysiological activity for extended periods of time. The specifications of the problem are as follows. Firstly, the communication environment is a metal primate cage. The particular environment is challenging because it acts as a chaotic reverberant cavity resonator and exhibits deep fading nulls throughout its volume. Moreover, the communication interface needs to transmit at least 16 channels of the NC3, sampled at 16 bits per sample at a rate of 20 ksps along with the appropriate frame markers, coding, packet counter, etc., that are required for reliable communication. Therefore, the aggregate bandwidth of the complete system is 25 Mbps. Finally, in order to avoid sacrificing battery life, the communication system needs to be as power efficient as possible.
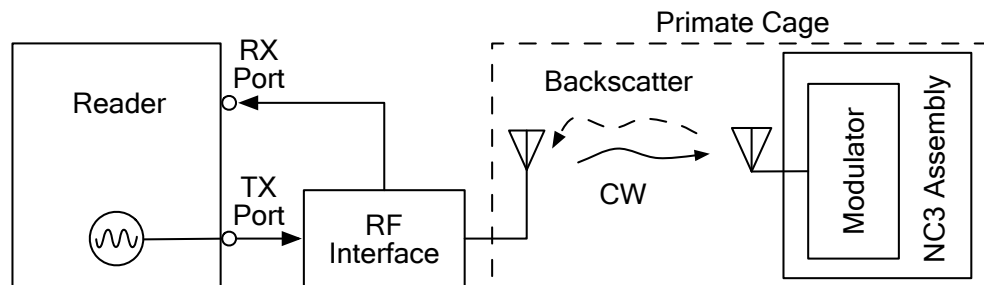
4.1.3   System Design

Figure 4.3: Backscatter data uplink system design.

The architecture of the proposed system is depicted in Fig. 4.3. Our approach is a differential quadrature phase shift keying (DQPSK) backscatter communication system at the UHF band and particularly at 923 MHz. In particular, we developed an external system that consists of a custom software defined radio (SDR) reader that generates an RF carrier and demodulates the backcsattered response. The RF carrier that is generated by the reader travels through a custom RF interface that implements full duplex communication so that we can use a single antenna for both receiving and transmitting[1]. The carrier is then emitted from an antenna that is installed on the cage and travels inside the cage and reaches the device shown in Fig. 4.3 as NC3 assembly. The NC3 assembly is a system that consists of a custom antenna developed by Apoorva Sharma,

---

[1]Chapter 5 contains a detailed description of the developed RF interface

a backscatter modulator, and the NC3 with its battery pack.

With this setup, we managed to transmit the neurophysiological data from the neurochip with a data-rate of up to 25 Mbps and a very low energy consumption of 12.4pJ/bit. Moreover, the receiver for this system is capable of demodulating data in near-real time. We also tested the system inside the metal animal cage and verified that communication can be achieved inside this particularly challenging environment. To the best of our knowledge, this is the first demonstration of a DQPSK backscatter radio system for BCIs that operate inside a metal primate cage.
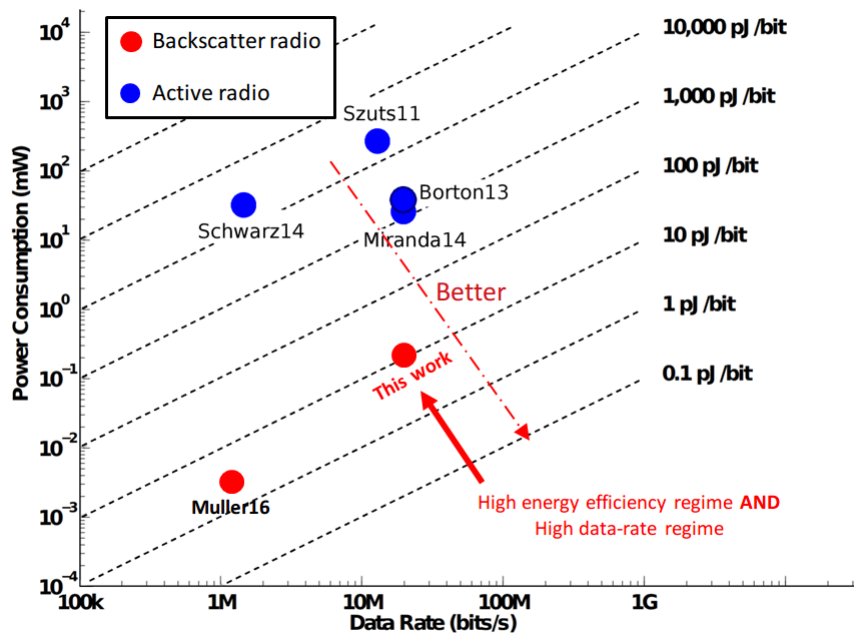
4.2 Prior Art

Figure 4.4: Comparison of prior art and this work. In contrast to the prior art, this work achieves both high energy efficiency *and* high data-rates. Figure credit James Rosenthal.

We compared our work with similar interfaces in the literature that were developed to transmit electrophysiological data from animals. The graph depicted in Fig. 4.4 illustrated the performance of the published papers in the literature with respect to the data-rate vs power consumption. The best performance works would be closer to the bottom right corner. The blue points denote the

communication interfaces with active radio modules whereas the red points denote communication interfaces with backscatter radio modules.

One can observe that most of the literature utilizes active radio modules. In particular, one of the higher data-rate systems, namely HermesD, developed by Miranda et al. [29] can transmit with a data-rate of 24 Mbps using active transmission of frequency shift-keying symbols. However, its energy consumption is on the order of 1250 pJ/bit. The highest data-rate *backscatter* communication system found in the literature is an implant developed by Muller et al. [7], which can transmit data at 1 Mbps with an energy consumption of 2.4 pJ/bit. However, its range, since it was optimized for implanted operation, is limited to a few cm.

The contribution of our work is that it is positioned in the high energy efficiency *and* high data-rate regime. In particular, our work can transmit at a data-rate of 25 Mbps with an energy consumption of 12.4 pJ/bit and at a distance of over a couple of meters. This is more than 100 times less energy cost per bit than the most competitive active radio system in the literature and more than 6 times higher data-rate than the most low-power systems. Table 4.1 lists in detail the specifications of our system and the state of the art.

Table 4.1: Comparison table with the state of the art in wireless neural recording interfaces for BCIs.

	Muller 2015 [7]	Schwarz 2014 [17]	Szuts 2011 [27]	Borton 2013 [28]	Miranda 2014 [29]	**This work [31]**	Units
BCI type	Implant	External	External	Subcutaneous	External	**External**	
Sampling rate	1	n.r.	20	20	30	**5/25**	ksps
Stimulation	✗	✗	✗	✗	✗	✓	
Num. of Channels	64	512	8	64	24	**64**	Mbps
Comms type	RF Bac.	Active RF	Active RF	Active RF	Active RF	**RF Bac.**	
TX Freq.	300 MHz	2.4 GHz	2.4 GHz	3.8 GHz	3.8 GHz	**923 MHz**	
data-rate	1	1.33	12	24	24	**25**	Mbps
Range	0.6 mm	3 m	60 m	1 m	20 m	**>2 m**	
Comms power	264	0	200	≥30[b]	30	**1**	mW
Energy/bit	2.4	1250	16,000	≥1,250[b]	1,250	**12.4**	pJ/bit
Test subject	Rat	Rat	Rat	NHP	NHP	**NHP**	

[a] Extrapolated from figure. Two-part system [b] Exact number not reported [c] EMG only was tested on human subject [n.r.] Not reported
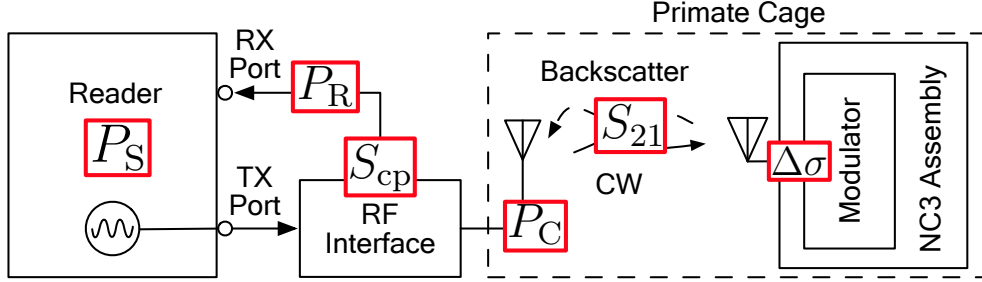
Figure 4.5: System design labelled with link budget variables on the corresponding system components.

4.3 Link Budget

To evaluate the performance of the proposed communication system, we calculated the link budget as follows:

$$P_\mathrm{R} = P_\mathrm{C} - 2\ S_{21} + \Delta\sigma + S_\mathrm{cp}\ , \tag{4.1}$$

where P_R is the received power at the RX port (as seen in Fig. 4.3 and P_C is the transmit carrier power. S_{21} are the path losses that are accounted for twice due to the fact that the backscatter signal needs to travel from the reader to the BCI and back. Finally, $\Delta\sigma$ is the differential radar cross section (RCS) [59], and S_cp is the coupling factor of the RF interface. The coupling factor of the RF interface that includes cable and connector losses is measured as

$$S_\mathrm{cp} = -12\ dB. \tag{4.2}$$

Moreover, in order to communicate reliably, the received backscatter power needs to be higher than the receiver sensitivity P_S, i.e.,

$$P_\mathrm{R} > P_\mathrm{S}\ . \tag{4.3}$$

Fig. 4.5 is an updated version of Fig. 4.3 and portrays each variable of 4.1 on the overall system design. Particularly, the sensitivity (P_S) and the transmit power (P_C) is determined by the reader. The coupling losses (S_cp) are determined by the RF interface. The environment, i.e., the primate
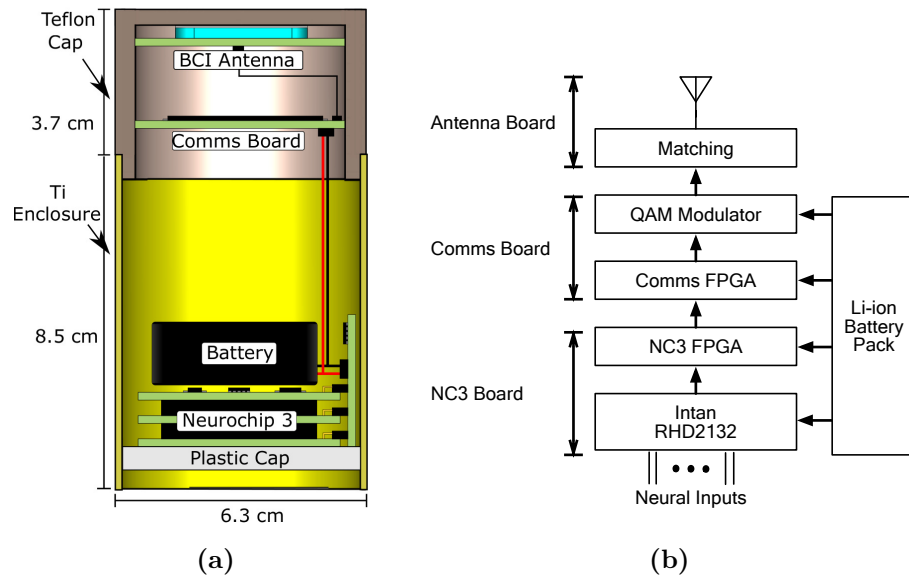
Figure 4.6: (a) Stack up of the NC3 components inside the titanium (Ti) enclosure and the Teflon cap. Figure credit Apoorva Sharma. (b) Block diagram and of the NC3 assembly setup.

cage, will determine the roundtrip path losses S_{21}. Finally, the antenna and the modulator will determine the differencial RCS ($\Delta\sigma$). In order to successfully communicate, all the components of the system had to be carefully designed. In the upcoming sections, we are going to break down the system to its constituent pieces and introduce the challenges and the contributions of each component.

4.4 NC3 Assembly

The block diagram and a layered model of the NC3 assembly is depicted in Fig. 4.6. As described in Sec. 4.1.1, the NC3 is enclosed inside a titanium tube and sealed with a teflon cap. We developed two custom boards to implement backscatter communication. In particular, we developed a board that contains a custom UHF antenna that was designed by Apoorva Sharma and a communications board (herein referenced to as comms board) that was developed by the author and James Rosenthal. It contains the RF and control electronics. One of the significant contributions of this approach lies in how seamlessly we integrated the backscatter communication module into the existing BCI infrastructure. Therefore, neuroscientists won't have to change already developed structures to
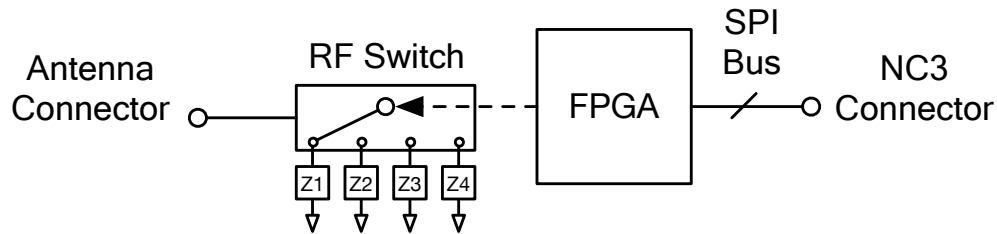
Figure 4.7: Comms board block diagram: An FPGA receives data from the NC3 via SPI bus and controls an RF switch to implement DQPSK backscatter modulation. A UMCX-type RF connector is utilized to connect the comms board with the custom antenna through a miniaturized coaxial cable.
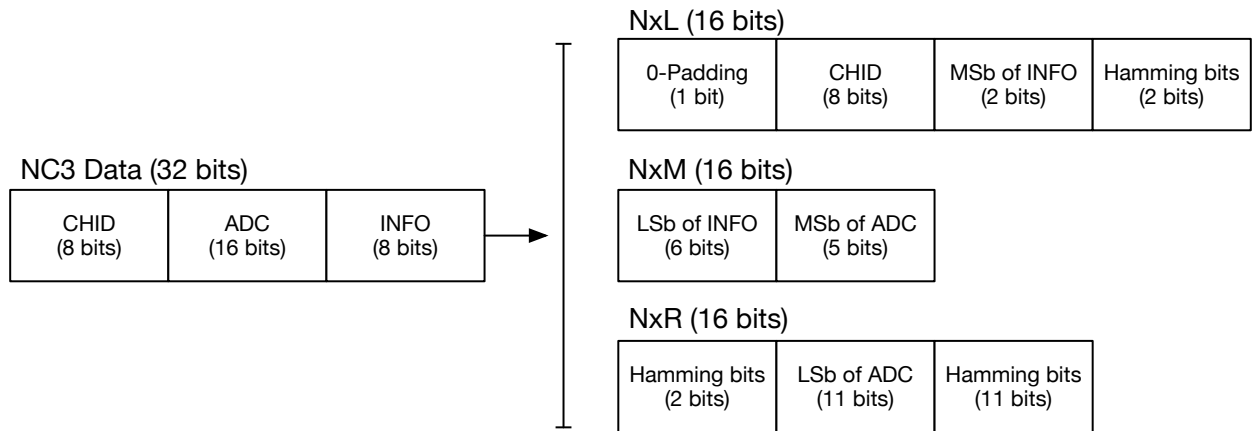
accommodate the adapted NC3.
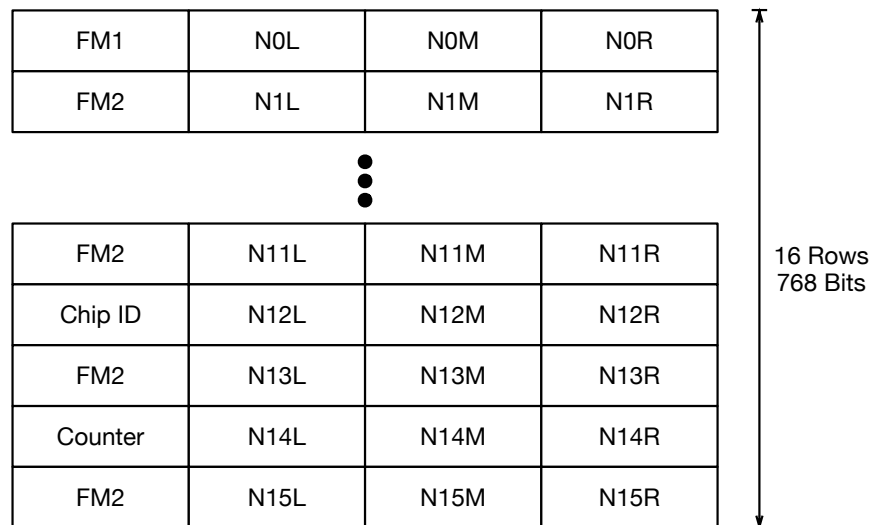
4.4.1 Comms board and packet structure

Fig. 4.7 depicts the system design of the comms board. The latter utilizes an Altera MAX10 field-programmable gate array (FPGA) clocked at 50 MHz to receive and packetize information from the NC3 via a serial peripheral interface (SPI) bus. An Analog Devices ADG904 RF single-pole-4-throw switch (SP4T) is something that has 4 fixed impedances connected to its terminals and is controlled by the FPGA and utilized as the DQPSK backscatter modulator. Moreover, the comms board employs a UMCX-type RF connector that is utilized to connect the RF switch with the custom antenna through a miniaturized coaxial cable. This board consumes 198 mW at 3.3 V mainly due to the relatively large and power-hungry FPGA.

The data from the NC3 is processed from the FPGA in the manner that is depicted in Fig. 4.8-(a). More specifically, the NC3 generates a bitstream of data that contains the corresponding 8-bit channel ID (denoted as CHID), the digitally converted 16-bit sample recorded from the on-board Intan RHD2132 (denoted as ADC), as well as 8-bits of information and debug data (denoted as INFO) that the include stimulation conditions, and the NC3 Status code, among others. The data is streamed serially, and each group of channel ID, ADC, and INFO is split into 3 16-bit words (denoted as NxL, NxM, and NxR).

The packet that contains the encapsulated NC3 data along with the appropriate frame marker

NxL (16 bits)

0-Padding (1 bit)	CHID (8 bits)	MSb of INFO (2 bits)	Hamming bits (2 bits)

NC3 Data (32 bits)

CHID (8 bits)	ADC (16 bits)	INFO (8 bits)

NxM (16 bits)

LSb of INFO (6 bits)	MSb of ADC (5 bits)

NxR (16 bits)

Hamming bits (2 bits)	LSb of ADC (11 bits)	Hamming bits (11 bits)

(a)

FM1	N0L	N0M	N0R
FM2	N1L	N1M	N1R

⋮

FM2	N11L	N11M	N11R
Chip ID	N12L	N12M	N12R
FM2	N13L	N13M	N13R
Counter	N14L	N14M	N14R
FM2	N15L	N15M	N15R

16 Rows
768 Bits

(b)

Figure 4.8: a) Row Structure: The NC3 data is streamed serially and each group of channel ID, ADC, and INFO is split into 3 16-bit words (denoted as NxL, NxM, and NxR) (b) Frame structure. Each row contains a sample from each channel, and the 768-bits frame is transmitted serially row-by-row.
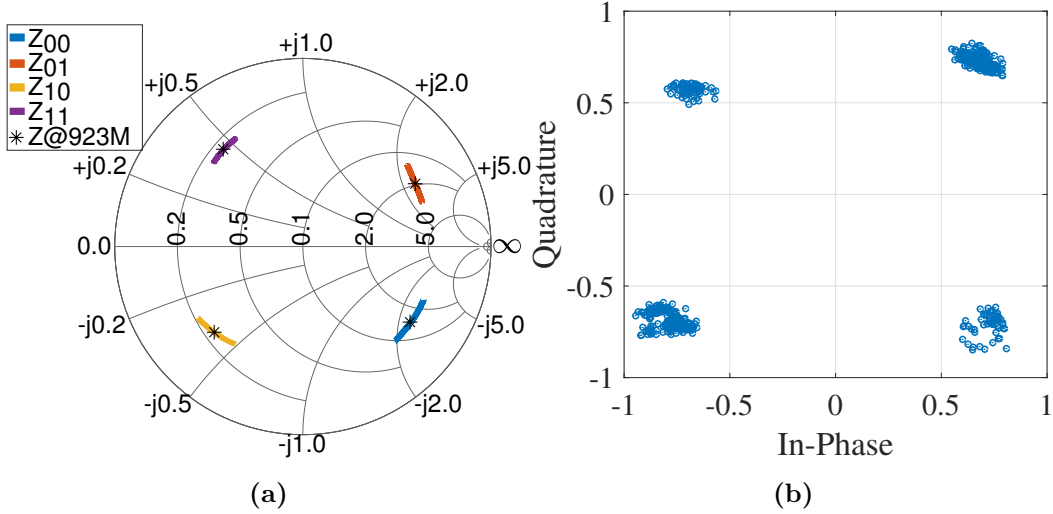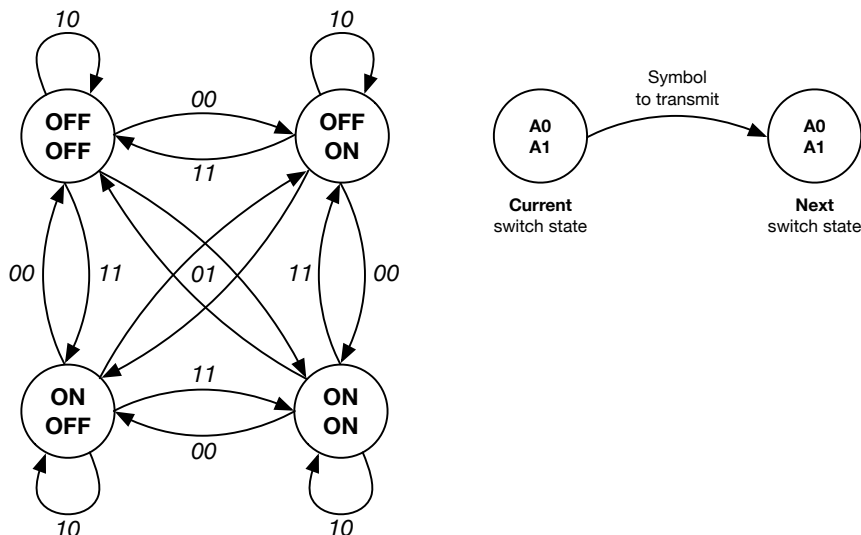
Figure 4.9: (a) S11 measurements of the DQPSK backscatter modulator for 4 different impedance states. (b) Symbol constellation recorded over 5,000 symbol periods.

prefixes are utilized so that that the reader can find the start of each packet. In order to increase the robustness of the backscatter link, we encapsulated the NC3 data encoded with a Hamming(16,11), an encoding scheme that provides single error correction and double error detection.

The complete frame structure is depicted in Fig. 4.8-(b). Each row contains a single sample of NC3 data that is split according to the method described above. The rows also contain 16-bit frame markers (denoted as FM1 and FM2) to facilitate frame synchronization during demodulation and decoding on the receiver. The values of the frame markers are as follows:

$$FM1 = [\,0\;1\;0\;1\;0\;1\;0\;1\;0\;1\;0\;1\;0\;1\;0\;1\,] \tag{4.4}$$

$$FM2 = [\,0\;0\;0\;0\;0\;0\;0\;0\;1\;1\;1\;1\;1\;1\;1\;1\,] \tag{4.5}$$

Moreover, a 16-bit identification number (denoted as Chip ID) and a 16-bit frame counter (denoted as Counter) are encapsulated in every frame and are utilized for error detection during decoding.

4.4.2 DQPSK Backscatter Modulation

We selected a DQPSK backscatter modulation that is implemented using an Analog Devices ADG904 RF single-pole-quadruple-throw switch connected to 4 carefully chosen impedances that

Figure 4.10: (a) S11 measurements of the DQPSK backscatter modulator for 4 different impedance states. (b) Symbol constellation recorded over 5,000 symbol periods.

yield the 4 symbol states as described in [23]. The DQPSK modulation was employed because it can be implemented with a small form factor components that consume less than 10 μW and is twice as spectrally efficient than a typical binary modulation. The differential symbols facilitate the demodulation process by eliminating the phase ambiguity created by device movement within the reverberant cavity environment. The transition diagram for the DQPSK modulation that is encoded on the FPGA firmware is shown in Fig. 4.10.

Fig. 4.9 (a) depicts the measured S_{11} values across the UHF ISM band, looking into the RF switch using a calibrated VNA. One can observe that the reflection coefficients of the 4 different switch states form a constellation on the Smith chart, corresponding to the 4 different symbol phases of the QPSK signal [23].

To measure the error vector magnitude (EVM) of the backscatter modulator, we collected 5,000 symbols using the receiver pipeline inside the NHP cage. The symbols, which are depicted in Fig. 4.9 (b), were compared to an ideal QPSK constellation and an EVM of 9.7% was calculated. The resulting EVM is primarily due to the tolerances of the passive components installed on the backscatter modulator.

Differential RCS

The differential RCS or $\Delta\sigma$ for a pair of reflection coefficients is calculated as follows:

$$\Delta\sigma = \frac{\lambda^2\ G^2}{4\ \pi}|\rho_1 - \rho_2|^2, \tag{4.6}$$

where λ is the wavelength of the carrier frequency, G is the antenna gain, and $\rho_{1,2}$ are the values complex reflection coefficients for which RCS is calculated. An RCS value can be calculated for every possible pair of reflection coefficients. However, the most important $\Delta\sigma$ is the one between the two closest reflection coefficient points on the smith chart (in this case, Z_{00} and Z_{01}) since it is going to determine the bit error rate. This is due to the fact that the larger the minimum differential RCS, the larger the minimum distance between the received backscattered symbols. As shown in [59], the bit error rate is determined by the minimum distance between symbols. For this system, we calculate:

$$\Delta\sigma = -24 \text{ dBsqm.} \tag{4.7}$$

4.5   Software-defined radio reader

To receive the incoming backscattered DQPSK signals, we expand the capabilities of the receiver that we developed in [30], and this aims to accommodate the higher order modulation (DQPSK instead of BPSK).

4.5.1   Hardware

A block diagram of the reader hardware is depicted in Fig. 4.11. The hardware components of the receiver include the Ettus USRP B210, a low-cost ($1100) software defined radio (SDR). The USRP is used to generate the CW carrier at 923 MHz that is backscattered by the NC3 assembly. The USRP downconverts the backscattered signal to baseband and samples the baseband. The sampled I/Q symbols are sent to an Intel Core i7 PC with a 3.8 GHz clock rate and 16 GB of memory. This PC supports the processing of 200 packets at a time in real time using GNUradio and MATLAB software and stores the reconstructed neural data to a hard-disk drive (HDD). The USRP has programmable transmit and receive gains. Specifically, our reader is capable of producing up to 30 dBm output power by making use of a Minicircuits ZRL-3500+ UHF amplifier.
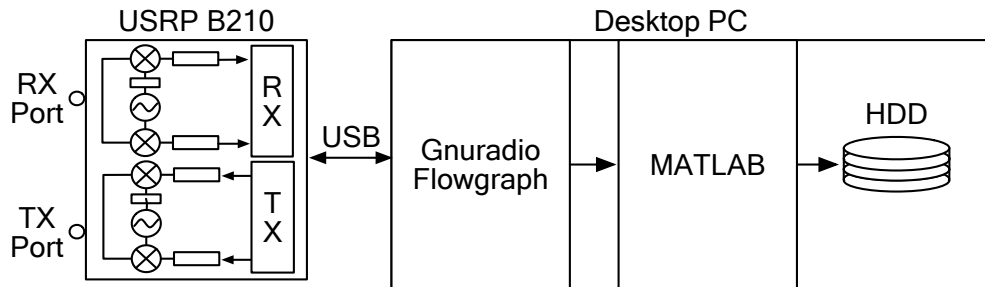
Figure 4.11: Reader hardware: A USRP B210 downconverts the backscattered signals to baseband and sends it to a PC for processing. There, a GNUradio flowgraph followed by a Matlab script are utilized to reconstruct neural data that is subsequently stored to a hard disk drive for post-processing.
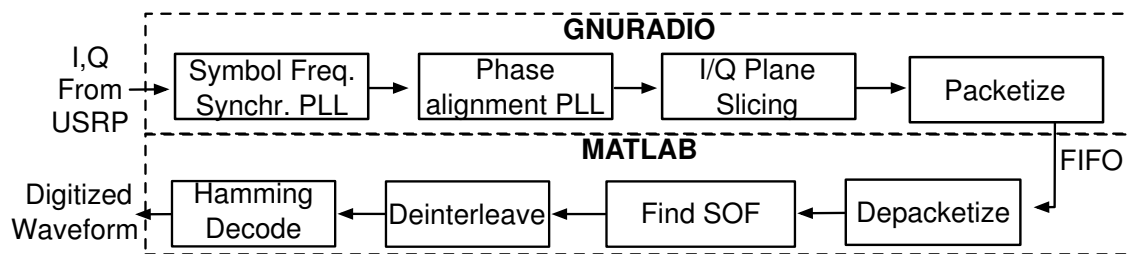

Figure 4.12: Receiver pipeline. GNUradio and Matlab scripts are responsible for demodulating the incoming I/Q data from the USRP.

Our approach has a significant contribution: By utilizing low cost open source hardware and software, the neuroscientists that are going to use our device won't have to purchase rare custom made equipment equipment. Rather, they can replicate this work with materials that are low-cost and off-the-shelf.

4.5.2 Software

Fig. 4.12 depicts the receiver pipeline. A GNUradio flowgraph implements symbol frequency synchronization, phase alignment, and slicing of the incoming I/Q symbols from the USRP. The resulting data is transferred to a MATLAB script using a Linux pipe, where start-of-frame synchro-
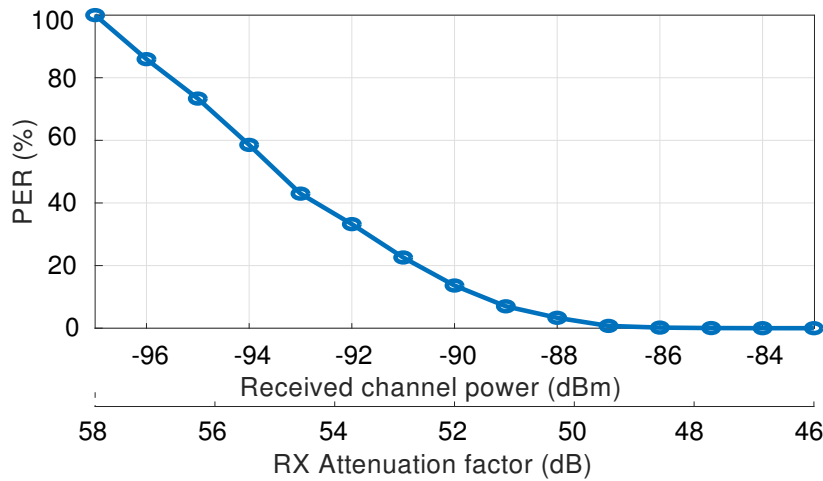
Figure 4.13: PER vs absolute received channel power and receive path attenuation. The receiver exhibits a PER of less than 0.2% at an input backscatter power of -86 dBm.

nization is conducted using the Barker codes embedded in the backscattered packets. Finally, de-interleaving and Hamming decoding is performed to extract the corresponding neural data stream, and the resulting waveform is plotted and saved to the disk for further analysis.

To characterize the reader sensitivity, we used a connectorized setup, introducing a variable attenuator to reduce the channel power available to the receiver in 1 dB steps from 46-58 dB of attenuation. This corresponds to an absolute channel power range of -83 dBm to -96 dBm. Using this setup, we collected a total of 10^6 frames for each RX path attenuation value and measured how many of these packets were erroneous by checking the fixed "Chip ID" that is transmitted with each frame. Subsequently, the packet error ratio (PER) was calculated by dividing the number of dropped frames by the total number of collected frames. As shown in Fig. 4.13, the receiver system exhibits a PER of less than 0.2% at an input backscatter channel power of -86 dBm and a PER of 100% at an input backscatter power of -97 dBm.

It is important to note that the GNUradio script without the Matlab processing can remodulate bits with a data-rate of up to 25 Mbps. When the matlab script is added to the flow, this rate drops to up to 6.25 Mbps due to the fact that Matlab is inherently slower than C++, the language in which the GNUradio flowgraph is compiled. Another one of our contributions is that, to the best of our knowledge, this is the fastest SDR backscatter receiver that can demodulate bits (and not just record I/Q symbols) in the literature.

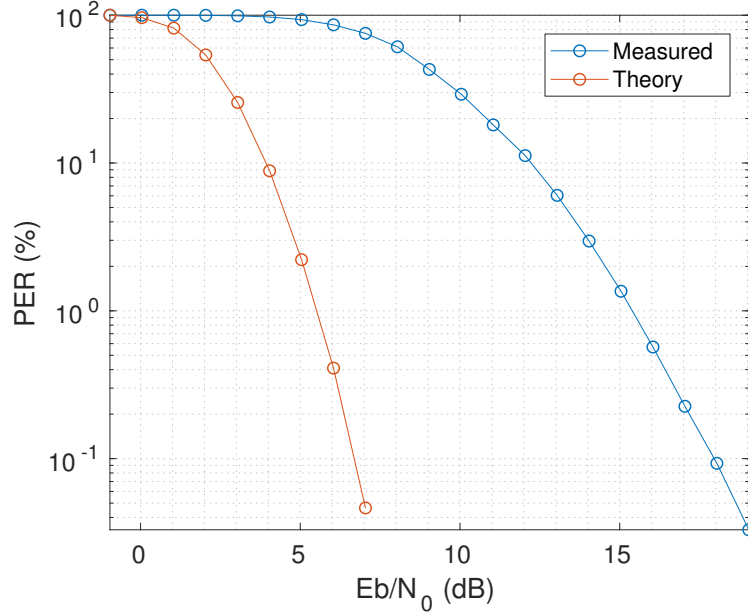## 4.6   Receiver performance comparison with theory

Figure 4.14: Theoretical vs measured Packet error ratio curves. The receiver performs approximately 12 dB worse than the analytical model due to non-idealities in the components of the system.

The PER vs signal to noise ratio (SNR) performance of the proposed receiver was compared against the theoretical performance of an ideal DQPSK receiver. Particularly, in [60], the probability of symbol error for an ideal DQPSK receiver was derived and is given as:

$$P_s = 2\, Q\left(\sqrt{\frac{2\, E_b}{N_0}}\right) \left[1 - \frac{1}{2}\, Q\left(\sqrt{\frac{2\, E_b}{N_0}}\right)\right], \tag{4.8}$$

where E_b is the received energy/bit, N_0 is the noise power spectral density, and Q is the tail distribution function of the standard normal distribution.

We selected PER as the comparison metric. However, since the theoretical curves are given in terms of probability of symbol error, we generated a function that provides the corresponding PER for a given probability of symbol error. Specifically, we fed the receiver with a 10^6 frames with

no errors. Subsequently, we increased P_s by introducing uniformly distributed symbol errors in simulation and measured the corresponding PER by feeding the receiver with the erroneous symbol stream. We used the resulting data to create a calibration function that maps PER to P_s and used this function to produce the corresponding theoretical PER vs E_b/N_0 curve.

The USRP I/Q data are un-calibrated ADC values that are generated by the on-board Analog devices AD9361 radio frequency integrated circuit (RFIC). Therefore, a conversion of ADC units to real values units was necessary. To find the noise floor of the USRP, we injected a 923 MHz CW with -50 dBm power from a calibrated signal generator to the receive port of the USRP. Subsequently, we configured the USRP to record I/Q samples to a file and set the RX gain to 65 dB. Finally, we calculated the root mean square power (RMS) of a total of 10 seconds of I/Q samples recorded at a sampling rate of $F_s = 12.5$ MHz, and to convert ADC units to Watts, we calculated a factor $G_{\text{W-ADC}}$ as follows:

$$G_{\text{W-ADC}} = \frac{P_{\text{W}}}{P_{\text{ADC}}}, \tag{4.9}$$

where P_{W} is power measured in Watts, P_{ADC} is the RMS power of the I/Q samples, and G_{ADC} is a factor that is used to convert Watts to ADC units. At an RX gain of 65 dB, we found that $G_{\text{W-ADC}} = 3.1937 \times 10^9$.

Subsequently, to estimate the noise floor of the USRP in Watts, we terminated its RX port and recorded a total of 10 seconds of I/Q samples, calculated the RMS power of the I/Q samples (in ADC units), and calculated the noise floor in Watts by utilizing 4.9. To verify the accuracy of the measurement, we calculated the noise figure at the specific gain and bandwidth as follows:

$$N_F = P_N - 10 \ \log_{10}(K \ T_0 \ 1000) - 10 \ \log_{10}(B), \tag{4.10}$$

where N_F is the noise figure in dBm, P_N is the noise floor in dBm, $K = 1.38 \times 10^-23$ Joules/Kelvin is the Boltzmann's constant, $T_0 = 298$ Kelvin is the room temperature, and $B = 12.5$ MHz is the instantaneous detected bandwidth. We measured a P_N of -99 dBm at a gain of 65 dB and at a carrier frequency of 923 MHz. From 4.10, we found that $N_F = 5$ dB, which verifies the official noise figure value from Analog devices [61]. Finally, we calculated $N_0 = -170$ dBm/Hz using:

$$N_0 = 10 \log 10(\frac{P_N}{B}). \tag{4.11}$$

To estimate the energy per bit of the backscattered symbols, we measured the channel power without the leaked carrier with an Agilent N9010A signal Analyzer and divided it with the instantaneous bandwidth:

$$E_b = \frac{P_{\text{ch}}}{B},\tag{4.12}$$

where P_{ch} is the channel power in Watts.

Finally, in order to produce the PER vs Eb/N_0 curve, we measured the PER by collecting a total of 10^6 frames using the USRP and executing the complete receiver pipeline as outlined in the previous section. To emulate different Eb values, we utilized an attenuator on the receive path with a 1 dB step. A comparison between the ideal receiver and the one developed for this work is shown in Fig. 4.14. It can be observed that the implemented receiver exhibits worse performance by 12 dB. This is due to the fact that the theoretical curves assume ideal demodulation. In other words, the effects of the leaked self-jammer, the non-ideal symbol frequency synchronization, EVM, non-ideal start-of-frame synchronization, etc., are not taken into account in the theoretical curves. These crucial non-idealities play an important role in the performance of the receiver, and a more comprehensive analytical framework is part of the future work.

4.7 Characterization of the animal cage

4.7.1 Antenna selection, design, and simulation

For the experimental setup, we utilized an actual metal NHP cage used by researchers in the primate center at the University of Washington. In the cage, we employed a monostatic backscatter communication setup with a cage-side antenna connected to the external receiver system and the BCI antenna embedded in the NC3 assembly.

Particularly, the cage-side antenna that was installed on top of the animal cage is an off-the-shelf Laird Technologies S9028PCR right-hand circularly polarized patch with a -10 dB bandwidth of 902-928 MHz and a gain of 8 dBic. With its plastic casing, it measures 25.8 cm x 25.8 cm x 3.2 cm (length x width x height). The choice of a circularly polarized antenna was driven by the fact that a BCI-antenna on the head of a freely moving NHP could have any orientation with respect to the cage-side antenna. Therefore, circular polarization would minimize the average polarization mismatch-losses.
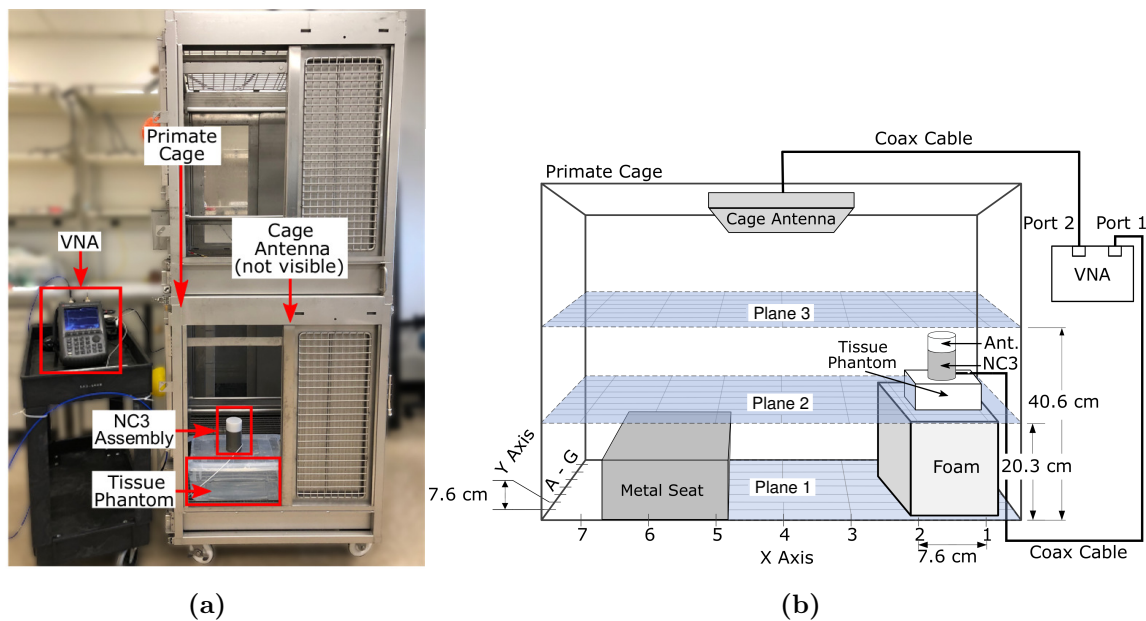
Figure 4.15: (a) Photo of the test setup used to characterize the wireless channel of the non-human primate cage. (b) Block diagram and of the test setup. Figure credit James Rosenthal.

The BCI antenna was designed by Apoorva Sharma and is thoroughly described in [31]. Particularly, it is a semi-custom design that consists of an Abracon APAE915R2540ABDB1-T ceramic patch antenna installed on a two-layer 1.6 mm PCB with a copper thickness of 30 μm. This particular antenna was selected due to the good combination of size and gain that it provides. The PCB contains a carefully designed circular ground plane with 1.5 cm ground plane that lies underneath the ceramic patch antenna element. The patch antenna is routed through an appropriate matching circuit and a Balun to a UMC coaxial connector for connecting the antenna board with the comms board.

EM Simulations that involve the complete NC3-Assembly inside the cage, enclosed with the teflon cap, were conducted. The results indicated a gain of -0.4 dBi and a bandwidth of 1 MHz, both realized at a center frequency of 923 MHz. Moreover, specific absorption rate (SAR) simulations were conducted in multiple positions inside the cage. For the simulations, a CW of 30 dBm (1 W) at 923 MHz was transmitted from the cage-side antenna, and a saline phantom was utilized to emulate the electromagnetic properties of an NHP. A maximum SAR of 0.6 W/kg averaged over

1 g of saline mass, which is 2.6 times lower than the 1.6 W/kg limit that is imposed by the Federal Communications Commission (FCC).

4.7.2 Measurement setup

We conducted EM measurements across the whole volume of the bottom compartment of the cage, as depicted in Fig. 4.15-(a), which measures 93 cm $\times$ 93.4 cm $\times$ 77 cm (height $\times$ width $\times$ length). The cage is made out of a square metal mesh with a mean side of 2.5 cm. The structure of this mesh is a boundary for EM waves since the operating frequency of 923 MHz has a wavelength of 32.5 cm, which is more than 10 times greater than the gap in the wall. However, the cage is not a fully enclosed Faraday cage since there is an EM-permeable window made out of clear plastic with dimensions of 60.7 cm $\times$ 23.4 cm (length $\times$ width) on one of the side walls of the cage.

To emulate the presence of a male macaque monkey in our measurements, we utilzed a saline phantom that consists of 7 L of saline solution with 0.91 g sodium chloride (NaCl) per liter of distilled water [40]. The saline is poured into a plastic box measuring 41.8 cm $\times$ 27.8 cm $\times$ 16.5 cm (length $\times$ width $\times$ height). On top of the plastic container with the saline phantom, we placed the aforementioned NC3 assembly and measured the link performance in multiple points inside the animal cage using a vector network analyzer (VNA). Particularly, we divided the volume of the cage into 3 planes, and each plane was subdivided to a square 2D grid consisting of 7.6 by 7.6 cm tiles. The tiles for the vertical direction were labeled with tags ranging from A-G, and for the horizontal direction, the tiles were labeled with numbers ranging from 1-7 for Planes 2 and 3 and 1-4 for plane 1. This measurement setup accounts for a total number of 126 measurement points; 49 points for Planes 2,3 and 28 for Plane 1.

4.7.3 EM Measurements

The 3-dB bandwidth (BW) and the insertion loss (IL) performance of the link was characterized inside the cage using the methodology described in the previous section. The results that we collected from all the planes are depicted in Fig. 4.16. The heatmaps in Fig. 4.16 is an aggregate of the measurements for each plane and uses lighter colors for larger BW or lower IL. Moreover, the mean BW was measured at 6.56 MHz, 6.50 MHz, and 6.70 MHz for Planes 1, 2, and 3 respectively. However, since the cage acts as a cavity, the BW changes greatly from location to location, ranging from 3.4 MHz to 22 MHz. In addition, mean measured IL was measured at 27.6 dB, 28.7 dB, and
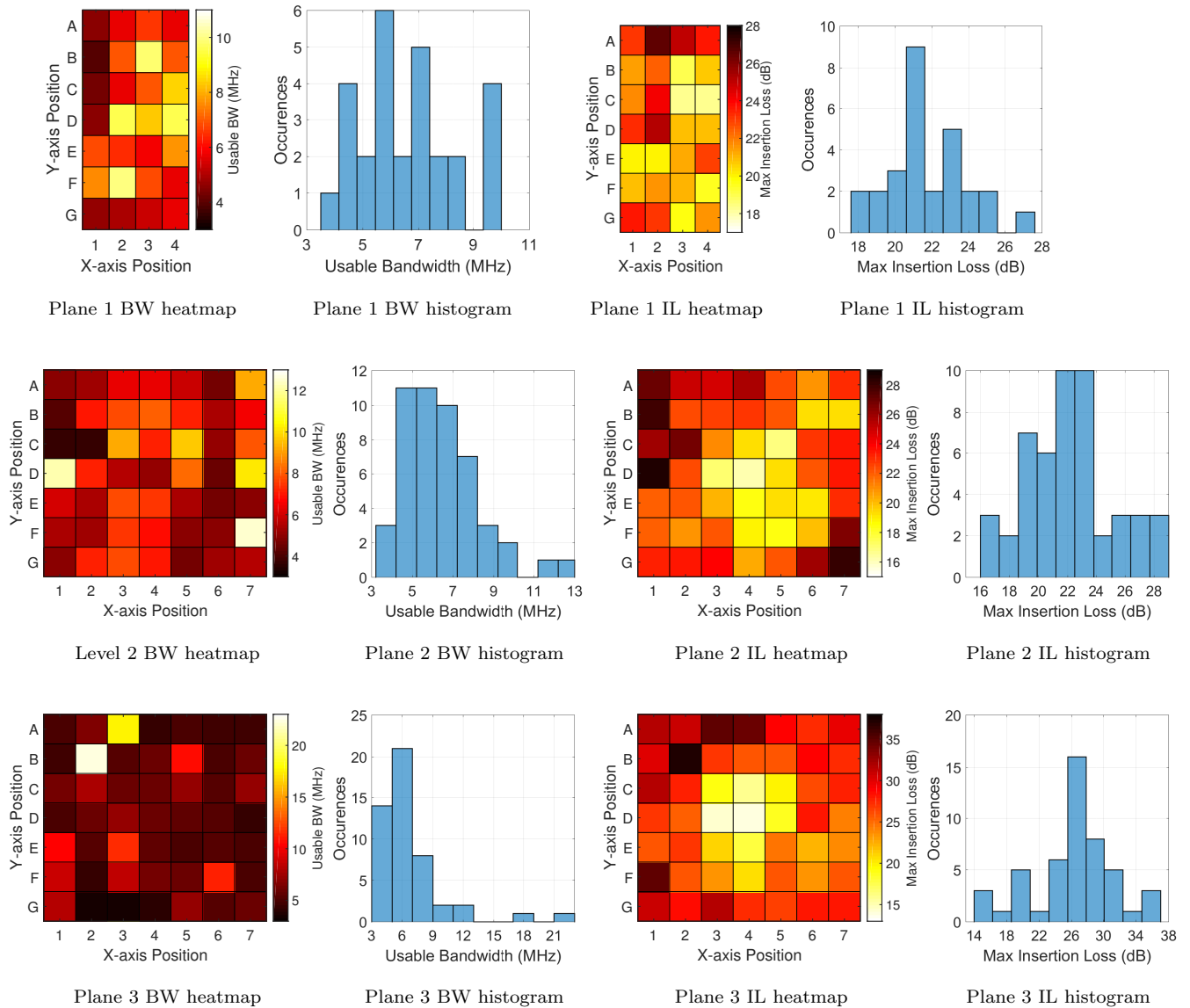
Figure 4.16: Experimental results for all Planes showing heatmaps and histograms derived from data for usable bandwidth (BW), and maximum insertion loss (IL). In all heatmap images, darker colors indicate worse performance. Figure credit Apoorva Sharma.

37 dB for Planes 1, 2, and 3, respectively, and, similarly, due to cavity effects, the IL ranges from 14 dB to 37 dB inside the cage, with the center of the cage exhibiting the smaller IL values.

The large variations in BW and IL are prominently due to the effect of heavy multipath inside the animal cage and reveal the necessity for a sophisticated system design that employs channel equalization in order to tackle this challenging communication channel. The next chapter describes the communication system that was developed and utilizes a conservative symbol rate of 3.125 MHz in order to establish a reliable datalink across the whole volume of the cage. Future work involves accommodating higher data-rates by taking the multipath effects into account.

4.7.4   Link Budget Revisit

Having collected the information regarding all of the components of the communication system, we can now compile the link budget equation by replacing all the variables with measured values. A summary of the parameters is listed in Table 4.2

Table 4.2: Experimentation parameters for NHP cage characterization.

Parameter	Value
P_C	10 dBm
P_S	-86 dBm
S_{21}	Measured, see Fig. 4.16
$\Delta\sigma$	-24 dBsqm
S_cp	-12 dB

In order to determine the minimum path loss for reliable communication, we solve Eq.4.1 for $P_\mathrm{R} > P_\mathrm{S}$ by substituting the values in Table 4.2, i.e.,

$$P_\mathrm{R} > P_\mathrm{S} \Leftrightarrow$$
$$-2\,S_{21} - 26 > -86 \Leftrightarrow$$
$$S_{21} < 30 \text{ dB,}$$
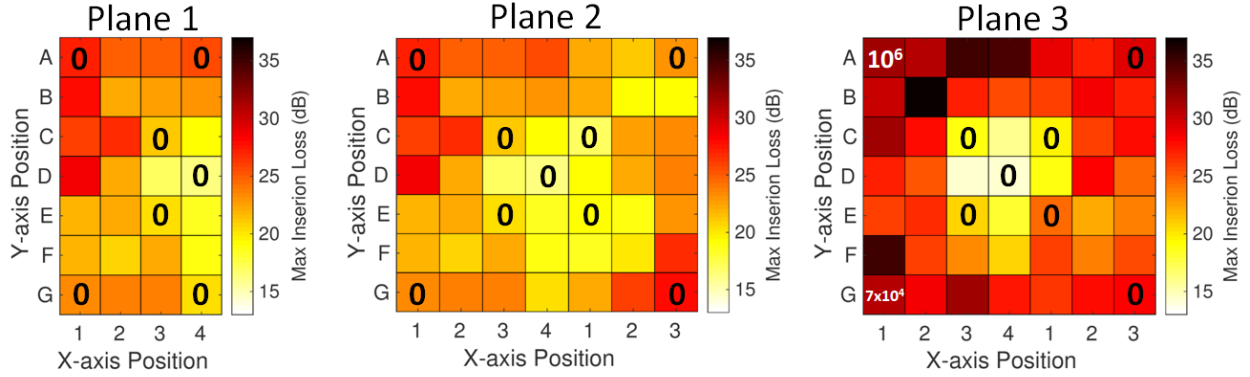
Figure 4.17: Packet error rate (PER) measurements for different locations inside the NHP cage. Measurements at Plane 3 demonstrate that the deep nulls affect the receiver's performance, as expected from the link budget.

which means that to have reliable communication, the path losses need to be less than 30 dB, and any losses above that value will inevitably result in packet drops.

4.7.5   PER measurements in the NHP cage

Finally, we conducted PER measurements inside the NHP cage to evaluate the end-to-end performance of the system throughout the entire cage volume. For this wireless setup, the USRP was programmed to output a 923 MHz carrier yielding a power of $P_C = 10$ dBm at the output of the coupler. Subsequently, a total of 10^6 packets were collected for each position. Fig. 4.17 depicts the collected data where the insertion loss measurements across the three different planes are overlaid with the number of dropped packets from the total 10^6 packets collected. It can be observed that a reliable link can be established in all but one corner location (Plane 3, position A1). The high PER at this position is due to a deep null in the channel with an insertion loss of 33 dB, as shown in Fig. 4.16. As expected from the return link budget, the link margin is inadequate in this location.

4.8   In-vivo measurement campaigns

To validate the interface of the NC3 assembly in combination with the high data-rate wireless receiver and the self-jammer canceller, we conducted in-vivo measurements using an anesthetized

NHP. We utilized the setup that was described in the sections above; this is depicted in Fig. 4.18. All the equipment was loaded on to a portable cart and transferred to the Washington National Primate Research Center in Seattle, WA, USA. All experimental procedures were formerly approved by the University of Washington (UW) Institutional Animal Care and Use Committee.
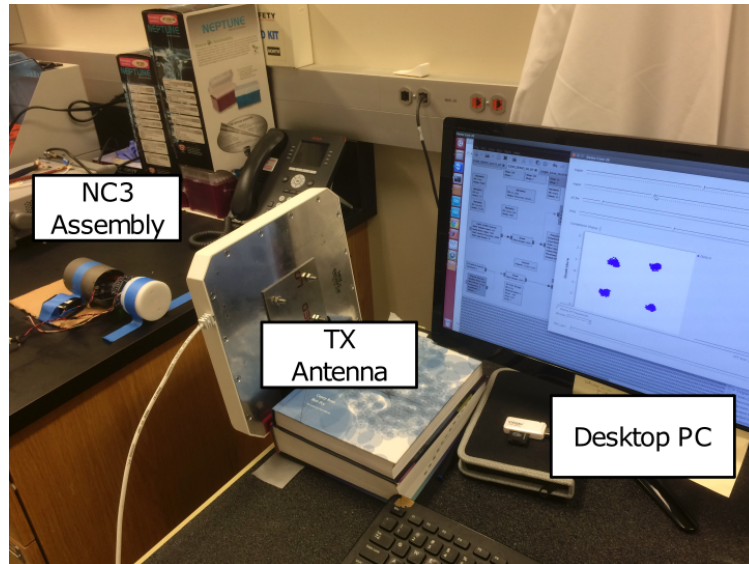
Figure 4.18: Experimentation setup for the in-vivo measurement campaign.

We conducted 2 rounds of experiments with basically identical setups but with a gap of 2 months between one other. In both experiments, the NHP subject was a pigtail macaque (*Macaca nemestrina*) that was already chronically implanted in the primary motor cortex (M1) with a 96-channel Utah Array from Blackrock Microsystems [62]. During the experiments, the NHP was anesthetized and placed on a surgical table with the NC3 assembly neural connectors wired to the Utah Array with a 10 cm custom-made shielded cable. The antenna of the NC3 was placed in line-of-sight from the TX antenna at a distance of 0.35 m, as shown in Fig. 4.18.

The first experiment was conducted to verify that the neural data received from the backscatter module are identical to the neural data captured by the NC3. For this experiment, the NC3 was configured to sample at 20 kHz with a band-pass filter with cutoff frequencies of 1 Hz – 7.5 kHz and a digital high-pass filter with a cutoff frequency of 1.6 Hz. The data was stored in its SD card memory and also transmitted via SPI to the backscatter modulator board. We set the receiver to demodulate data at 6.25 Mbps and store the recorded IQ data in the hard disk for post processing.

The recorded data exhibited a packet error rate of 0.008%, which is, as expected, negligibly low.

To extract the recorded neural data, we postprocessed the IQ signal output of the receiver with the software that was described above. The resulting neural signals were then compared to the neural signals that were stored on the SD card of the NC3. The results are depicted in Fig. 4.19-top where we observe low frequency fluctuations that correspond to local field potentials (LFP) as well as high frequency signals that correspond to action potentials (AP). Moreover, we see that there's good agreement between the recorded SD card data and the backscattered data. To highlight the recording of the action potentials, we filtered the data using a 10-th order Parks Mckellan bandpass filter with a bandpass region of 300-3000 Hz. We observed that the AP activity is even more prominent after filtering.

Moreover, we parsed the data through a spike sorting algorithm to validate that the recordings contain biologically relevant signals. The spike sorting algorithm that was used is described in [63] and the implementation was developed in MATLAB by James Rosenthal. Several spike clusters were identified and one of the clusters is depicted in Fig. 4.19-bottom. In this figure, we can observe that the action potentials of that particular cluster are recorded with very high fidelity.
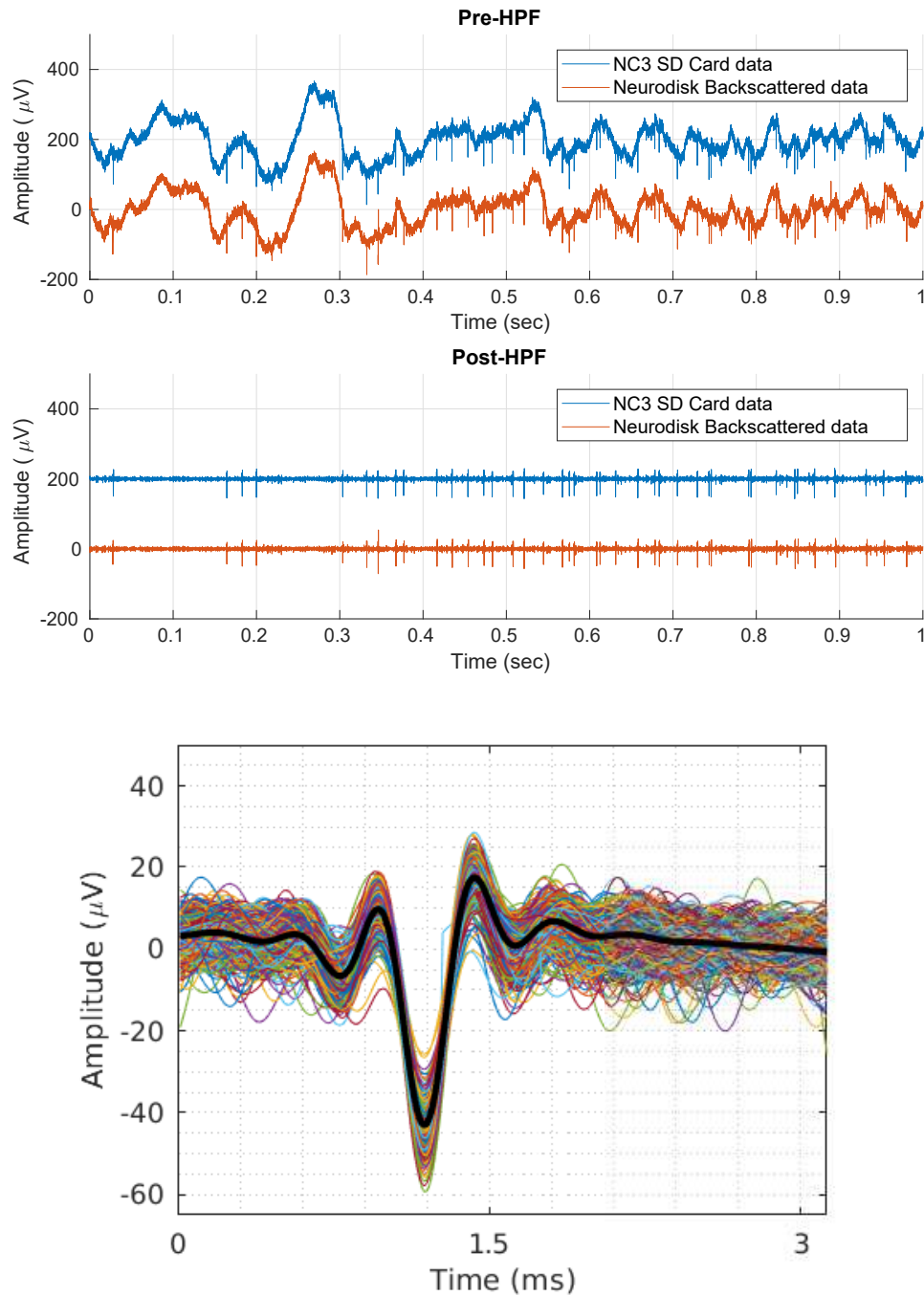
Figure 4.19: Top: Results from the first round of experiments taken at 6.25 Mbps. Comparison plot of neural data shows good agreement between recorded and backscattered data. Bottom: Results from the spike sorting algorithm that was described in [63] and was written in MATLAB by James Rosenthal. We observed that the action potential activity is recorded with high fidelity.
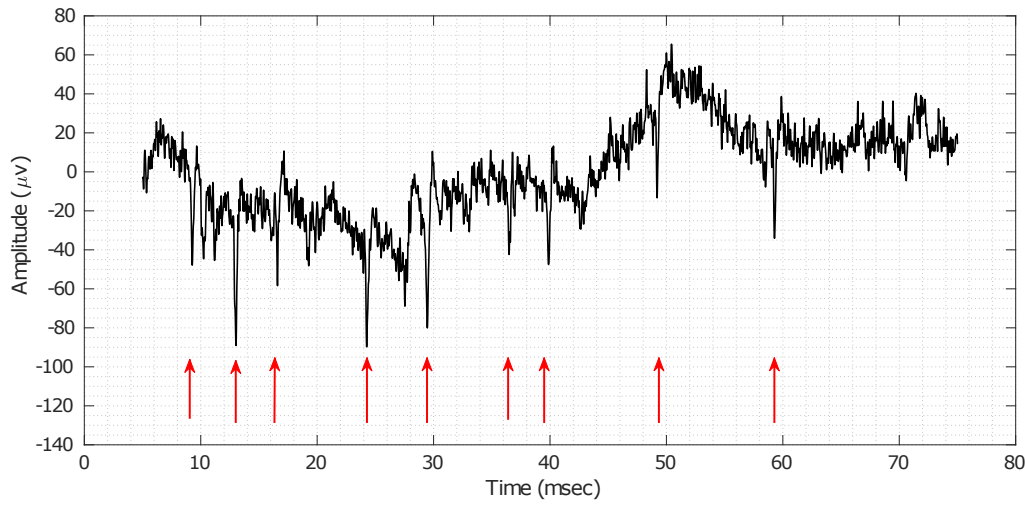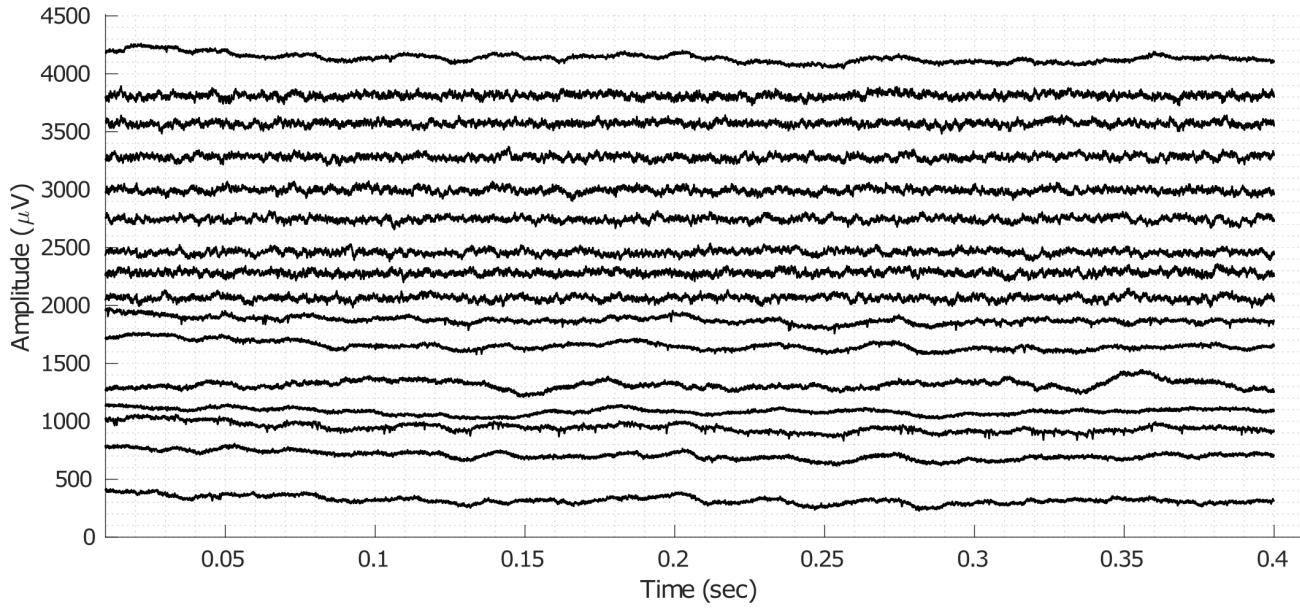
Figure 4.20: Top: neural data from all 16-channels collected at 25 Mbps. Bottom: zoomed-in view in the region of the data that is designated with a red box; LFPs and action potentials can be observed.
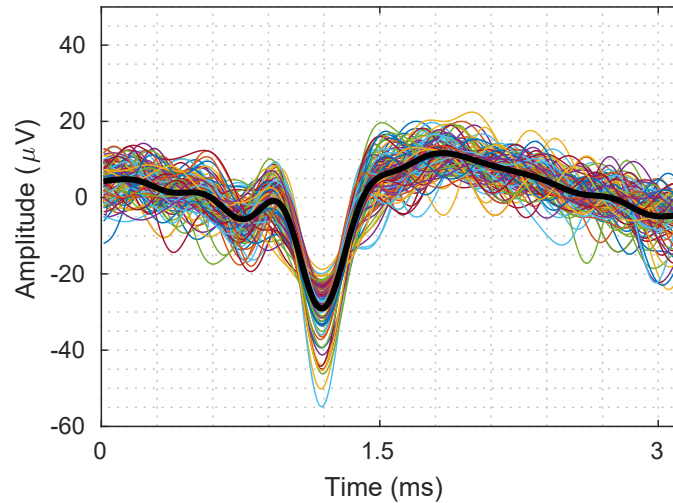
Figure 4.21: Spike sorting algorithm result that designates good AP activity that was recorded in the second round of experiments.

The second measurement campaign took place to validate the high data-rate capabilities of the system in a real-world scenario. In this case, 16 channels of the neurochip were sampled, with a rate of 20 ksps and a resolution of 16 bits. The aggregated data-rate, including the appropriate frame markers and error correcting codes, was on the order of 25 Mbps. The receiver was set to its maximum baseband sampling rate of 40 Msps and the resulting DQPSK symbols were recorded to the PC hard disk drive for post processing.

The recorded results from all 16 channels are depicted in Fig. 4.20. However, during the second round of experiments, some of the channels exhibited lower signal to noise ratio. As a result, 6 channels were not showing either the LFP activity or AP. That could be attributed to neural cell loss or glial scarring as a result of the chronically implanted micro-electrode array. Nonetheless, 8 out of 16 channels demonstrated good neural potential activity. For example, neural activity can be seen in Fig. 4.20-bottom, where we zoomed in on the third to last channel (designated with a red box) and pointed out the AP signals with red arrows. Finally, we ran the same spike sorting algorithm that was described above and plotted one of the identified clusters in Fig. 4.21. The signal fidelity in this round of experiments was slightly worse than the signal fidelity in the first one, but AP activity was identified nonetheless.

4.9   Conclusion

This chapter described the development of a wireless uplink for BCIs that are used to acquire neural data from NHPs. The uplink is implemented with a backscatter communication interface that employs a custom comms board with a DQPSK backscatter modulator cabable of transmitting data with rates up to 25 Mbps and a custom UHF antenna for the 923 MHz ISM band. Moreover, an external system composed of a USRP-based software-defined radio captures and demodulates the backscattered signals from the communication system in real-time. A PER of 0% was demonstrated for 124/126 positions inside the NHP cage that demonstrates that an uplink backscatter communication is a viable and attractive solution even for the challenging channels of an animal cage that exhibit deep fading nulls due to the reverberant cavity effects. Finally, we demonstrated with *in-vivo* experimentation that the system is operational in a real-world scenario and showed that the wireless data collection can be implemented seamlessly using this approach.

Chapter 5

A MIXED SIGNAL APPROACH FOR SELF-JAMMER CANCELLATION

5.1 Introduction

One of the idiosyncrasies of backscatter communication is that the reader is responsible for emitting a strong carrier wave while simultaneously receiving the backscattered response from the corresponding transponder [43]. However, due to the roundtrip path losses and losses from the differential RCS, as shown in Sec. 4.3, the backscattered response is much weaker than the CW. For example, channel measurements in Chapter 4 indicate average losses of 23 dB inside the primate cage. By accounting for the path losses twice and along with a $\Delta\sigma$ of -24 dBsqm, the backscatter response according to the link budget of 4.1 will be 70 dB smaller than the emitted CW. In essence, the strong CW acts as a self-jammer and the backscatter receiver needs to adapt to it with increased dynamic range and/or by isolating transmit and receive paths.

In monostatic systems, a single antenna is employed on the reader and a coupler or a circulator is utilized to isolate the transmit and receive paths. On the other hand, bistatic systems employ two antennas for transmit and receive path, respectively, while physical separation of the antennas is utilized for isolation [43]. In either case, however, a significant portion of the CW is leaked into the receiver. But this needs to be canceled in order to reduce the dynamic range requirements of the system. This chapter will focus on the development of a self-jammer canceler in monostatic systems.

5.1.1 Problem statement

We illustrate the importance of the self-jammer cancellation with an example that is based on the components of the system that was developed in Chapter 4. Particularly, we used a 10 dB coupler from Pasternack and a Laird Technologies S9028PCR antenna with a measured return loss of 10 dB at 923 Mhz. As illustrated in Fig. 5.1, if a carrier wave with 10 dBm is injected to the input of the coupler and transmitted using the particular antenna, the resulting CW power at the output-couple
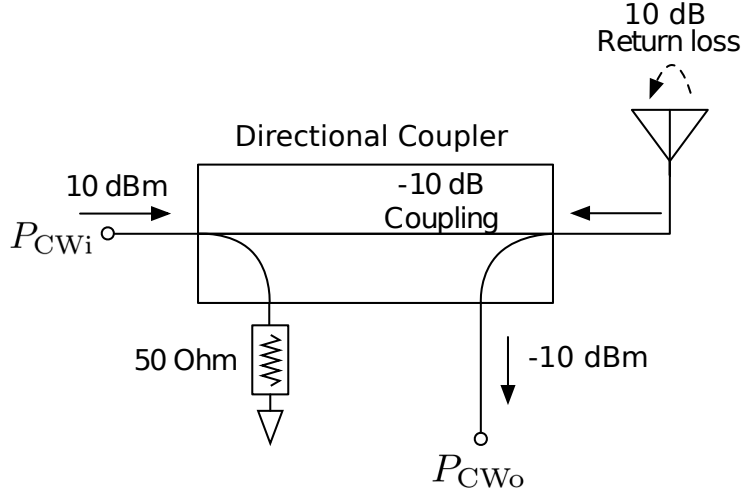
Figure 5.1: Example of isolation circuit using a directional coupler. At a 10 dBm output power and an antenna with 10 dB return loss, the leaked carrier is -10 dBm.

port that is connected to the receiver is on the order of -10 dBm. Transmit-to-receive isolation is typically defined as the difference between the transmitted carrier power that is injected at the input of the coupler and the carrier received at the output-couple port of the coupler [36]:

$$S_{\mathrm{iso}} = P_{\mathrm{CWi}} - P_{\mathrm{CWo}}, \tag{5.1}$$

where S_{iso} is the transmit-to-receive isolation in dB, P_{CWi} is the transmitted carrier power in dBm, and P_{CWo} is the received carrier power in dBm.

An important metric to determine the maximum allowed receive power is the 1-dB compression point of the LNAs at the receiver. Any input higher than that point will saturate the LNAs, which will cause extreme distortions of the recorded RF signals and severely hinder data demodulation. We measured the 1-dB compression point for different RX gain values of the USRP B210 that was utilized throughout this thesis. Specifically, we injected a CW at the RX port of the USRP and increased its transmit power until we observed a 1-dB non-linearity. The results from this process are shown in Fig. 5.2 where one can observe that for an input power of -10 dBm, the maximum RX gain that can be utilized without compromising the receiver's linearity is limited to only 20 dB out of the maximum 76. Aside from the fact that we could amplify the useful signal by more than 55 dB, the noise figure of the USRP at such low RX gains is on the order of 30 dB, 25 dB higher
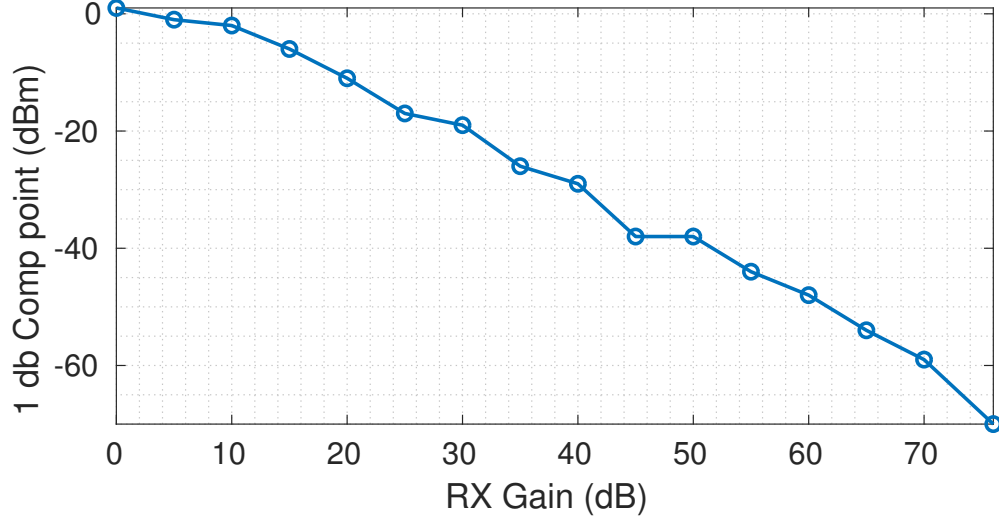
Figure 5.2: Measured USRP B210 1-dB compression point. The maximum RX gain before entering the USRP's non-linear region is limited by the input power.

than the NF exhibited in RX gains higher than 60 dB [61]. It is evident from this example that a self-jammer cancellation system would greatly improve the performance of the receiver by several orders of magnitude.

5.2 Theory of operation

A very effective method for implementing self-jammer cancellation is by using a bidirectional coupler with a matched load connected to its input-coupled port [36]. A block diagram with the functionality of this method is outlined in Fig. 5.3. A CW with power P_1 is injected at the input (Port 1) of a coupler and an antenna with a reflection coeffictient. Γ_A is connected at the output of the coupler (Port 2). In an ideal coupler, the S-parameters are as follows:

$$S_{21} = S_{12} = S_{34} = S_{43} \triangleq S_\mathrm{T}, \tag{5.2}$$

$$S_{42} = S_{31} \triangleq S_\mathrm{C}, \tag{5.3}$$

$$S_{41} = S_{32} = 0. \tag{5.4}$$
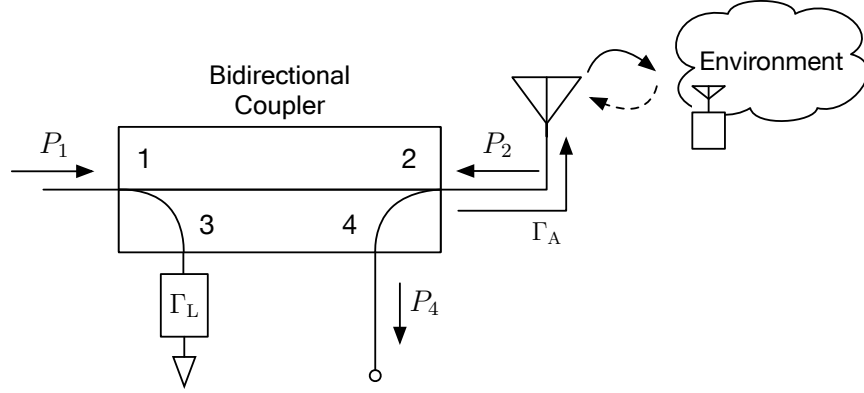
Figure 5.3: Self-jammer cancellation with matched load on input-couple port.

Finally, the power of the leaked carrier due to antenna mismatch and reflections of the CW from the environment as seen at the output-coupled port (Port 4) is given as:

$$P_4 = P_2 \ S_{42} + P_1 \ (S_{21}\Gamma_A \ S_{42} + S_{31} \ \Gamma_L \ S_{43}), \tag{5.5}$$

where Γ_L is the reflection coefficient of a load connected to the input-couple port (Port 3). By substituting 5.2, 5.3 and 5.4 to 5.5, we get:

$$P_4 = P_2 \ S_{S_C} + P_1 \ S_C \ S_T \ (\Gamma_A + \Gamma_L), \tag{5.6}$$

It can be easily observed that when the reflection coefficient of the load connected to Port 3 is symmetrical to the antenna's reflection coefficient, i.e., $\Gamma_A = -\Gamma_L$, the self-jammer is completely canceled from the received signal and 5.6 is reduced to:

$$P_4 = P_2 \ S_C. \tag{5.7}$$

It is important to note that by utilizing this method, the phase generated by the carrier wave generator is canceled along with the sinusoid at the center frequency [36].

5.2.1   Sinewave cancellation

The signal on the receiver can be written as follows [36]:

$$S_{\text{RX}} = S_{\text{TAG}}(t) + \sum_k S_{\text{Jammer}}k(t) = \tag{5.8}$$

$$= A_{\text{TAG}}(t)\cos(\omega\ t + \phi_{\text{TAG}}(t)) + \sum_k A_k(t)\cos(\omega\ t + \phi_k(t)), \tag{5.9}$$

where S_{RX} is the aggregate signal from the receiver, $S_{\text{TAG}}(t) = A_{\text{TAG}}(t)\cos(\omega\ t + \phi_{\text{TAG}}(t))$ is the tag's backscatter response, i.e., the carrier wave that reflects a time-varying phase and amplitude and $\sum_k S_{\text{Jammer}}k(t) = \sum_k A_k(t)\cos(\omega\ t + \phi_k(t))$ represents the sum of the self-jamming signals that include reflections from the environment, leakage due to the coupler, and antenna mismatch. The latter is the undesired signal that we're trying to cancel. Assuming a quasi-static channel with no or slowly moving objects, the self-jamming signals can be simplified to a single sinusoid, i.e.:

$$\sum_k S_{\text{Jammer}}k(t) = A_k \cos(\omega\ t + \phi_k) \tag{5.10}$$

By modulating the impedance of the load connected to Port 3, the phase and amplitude of the sinusoidal wave that is coupled to Port 4 (herein referred to as the cancelling wave) is modulated and added to the jamming wave. When these two waves have exactly the same amplitude and 180 degrees shifted phase, the self-jammer is cancelled. The RMS power of the resulting wave after the addition of the self-jamming and the cancelling wave can be written as:

$$P_{\text{res}} = 10\log 10\Big(\lim_{T\to\infty} \sqrt{\frac{1}{T}\int_0^T \Big(A_k\cos(\omega\ t + \phi_k) + A_{\text{canc}}\cos(\omega\ t + \phi_{\text{canc}})\Big)^2 \, dt}\Big), \tag{5.11}$$

where P_{res} is the power of the resulting wave in dBV, A_{canc} and ϕ_{canc} is the amplitude and the phase of the cancelling wave, respectively. The latter can be adjusted by utilizing an appropriate load on the input couple port of the coupler. Fig. 5.4 depicts the residual signal after adding two sinusoids, with one of them acting as the cancelling wave with varying phase and amplitude values. Without loss of generality, it is assumed from this figure that the self-jamming wave has zero phase and an amplitude of 1. As expected, when the two waves have equal amplitudes (unity gain) and the cancelling wave is 180 degrees phase-shifted with respect to the self-jamming wave, cancellation is optimal.

As one can observe in Fig. 5.4, the cancellation null is extremely sharp. This imposes a significant challenge on this approach: the system is extremely sensitive to changes, and tuning of the phase and amplitude requires very high resolution in order to achieve high cancellation.
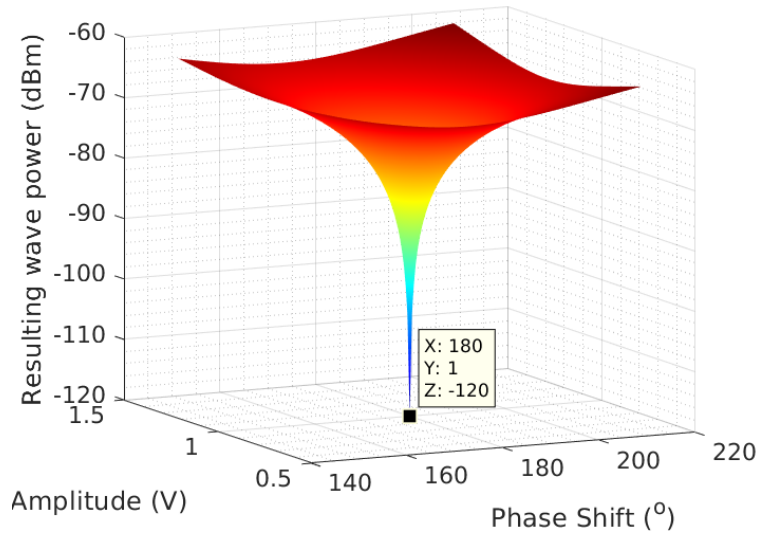
Figure 5.4: Resulting wave RMS power simulation using a phase-shifted and amplitude-scaled wave; a sharp null is exhibited when the cancelling wave has 180 degrees phase shift, which exhibits the same amplitude as the self-jamming wave. RMS power values larger than -60 dBm were omitted from the results.

5.2.2 Resolution vs Cancellation

In a real-world scenario, the communication channel will change over time, thus altering the phase and amplitude of the self-jamming wave. Therefore, controlling the load that modulates the phase and amplitude of the cancelling wave is essential for practical cancellation. A popular and effective way of implementing adaptive self-jammer cancellation is by controlling the variable impedance value that is connected to the input-couple port of the coupler based on power at the TX/RX antenna [36]. An illustration of this functionality is given in Fig. 5.5: An RF splitter separates the received signal to a path that goes to the receive port and to a path that goes to a power detector. The power detector measures the power of the incoming signal and outputs a DC signal that is measured by a controller (typically an MCU with an embedded ADC). The controller, by using some form of algorithm, then scans different loads on the variable impedance load and selects the one that minimizes the received power based on the output of the power detector. Several algorithms and components can be selected to implement this functionality.
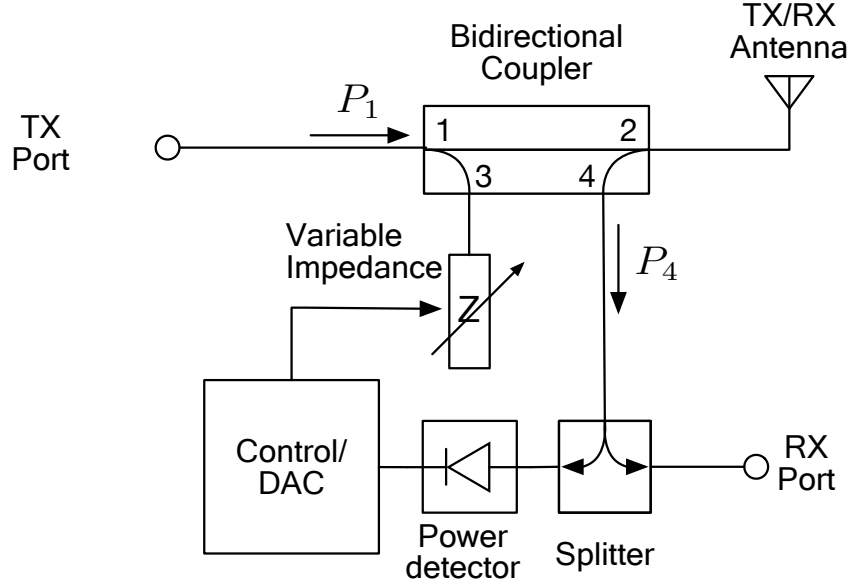
Figure 5.5: Adaptive self-jammer cancellation using a power detector and a variable impedance module.

Phase Sensitivity

The variable impedance load can be implemented with a phase shifter in series with a variable RF attenuator or with tunable capacitors [45]. Such components are available as commercial off-the-shelf modules and can be controlled either digitally [64, 45] or with an analog signal [65]. We will now show that such a system is extremely sensitive with respect to phase and attenuation changes. We calculated the received power of the resulting wave after cancellation and assuming matched amplitudes as follows.

$$P_{\text{res}} = 10 \log_{10} \left(\lim_{T \to \infty} \sqrt{\frac{1}{T} \int_0^T \left(\sin(\omega\ t + \phi_k) + \sin(\omega\ t + \phi_{\text{canc}}) \right)^2 dt} \right), \qquad (5.12)$$

where $P_r es$ is the RMS power of the resulting wave in dBV after the addition of cancelling and self-jamming wave with phases ϕ_k and ϕ_{canc} and same frequency ω. By utilizing the following identity,

$$\sin \theta + \sin \phi = 2\ \sin \left(\frac{\theta + \phi}{2} \right)\ \cos \left(\frac{\theta - \phi}{2} \right), \qquad (5.13)$$

equation **??** is rewritten as:

$$P_{\text{res}} = 10 \log_{10} \lim_{T \to \infty} \sqrt{\frac{1}{T} \int_0^T 2 \left(\sin(\omega \ t + \frac{\phi_k + \phi_{\text{canc}}}{2}) \ \cos(\frac{\phi_k - \phi_{\text{canc}}}{2}) \right)^2 dt} \tag{5.14}$$

$$= 10 \log_{10} \left(\sqrt{2} \ \cos(\frac{\phi_k - \phi_{\text{canc}}}{2}) \right). \tag{5.15}$$

Then, if we define ϕ_a as

$$\phi_a = \frac{\phi_k - \phi_{\text{canc}}}{2}, \tag{5.16}$$

when

$$\phi_a = n \ \pi + \pi/2 \qquad n \in \mathbb{Z}, \tag{5.17}$$

the self-jammer is canceled optimally and $P_{\text{res}} = -\infty$. Therefore, the closest the load impedance comes to a value that will result in a cancelling wave with the appropriate phase, the highest the cancellation factor will be. However, this process is extremely sensitive with respect to phase, i.e., the system has a very high Q.

To evaluate the sensitivity of the system with respect to phase changes, we calculated the derivative of 5.15 with respect to ϕ_a, as follows:

$$\frac{dP_{\text{res}}}{d\phi_a} = \frac{d10 \log_{10} \left(\sqrt{2} \ \cos(\phi_a) \right)}{d\phi_a} \tag{5.18}$$

$$= - \tan(\phi_a) \frac{10}{\log_2 (10)}, \tag{5.19}$$

and we plot both 5.19 and 5.15 in Fig. 5.6. We can see that as we approach the optimal $\phi_a = 90^o$ that the resulting wave is canceled with extreme sensitivity. For example, close to 88 degrees, the cancellation is more than 100 dB/degree. Therefore, any small change in the phase (for example due to temperature change) when the self-jammer canceller is tuned will result in extreme changes in cancellation.

Impedance Resolution

One of the fundamental differences between this work and prior art is that we utilized a mixed signal approach where a 12-bits resolution DAC generates the analog control signals for the variable
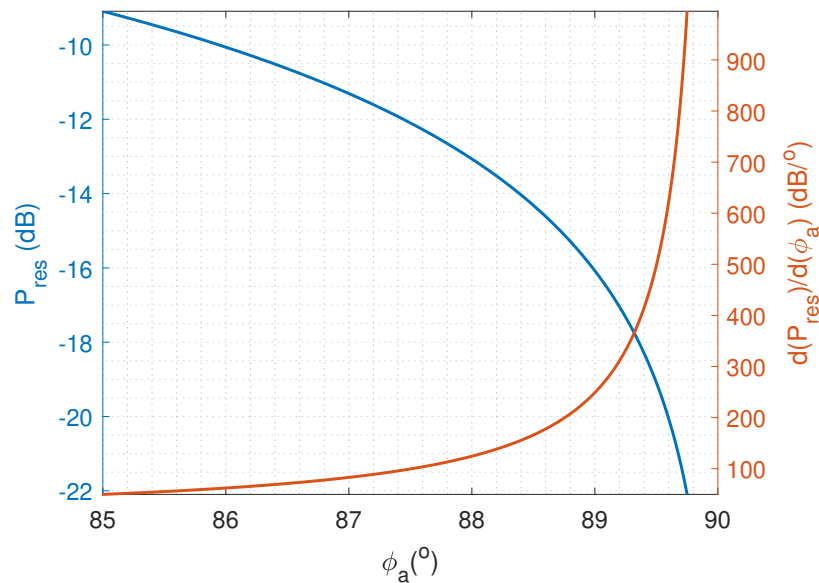
Figure 5.6: Cancellation vs phase and cancellation sensitivity vs phase. When tuned, the system is extremely sensitive to small phase changes (e.g. due to temperature).

impedance load. Therefore, much higher resolution that utilizes COTS modules and is limited to a maximum of 6 bits is achieved when compared to the ones in prior art, and as a result, more efficient cancellation is produced.

This is because, in essence, such a self-jammer canceler system samples the waveform depicted in Fig. 5.4 in the amplitude and phase dimensions. Intuitively, a higher resolution will provide higher accuracy for locating the phase and amplitude values that provide optimal cancellation. However, the possible impedance values is limited by the control signal resolution and, in the general case of digital control, the number of bits.

Assuming a fixed, unity amplitude for both the carrier wave and the cancelling wave, the waveform that the self jammer canceller needs to sample is a slice of the deepest null from Fig. 5.4. To demonstrate the importance of the control resolution, Fig. 5.7 depicts the cancellation factor vs the phase of the cancelling wave when a 6,10 and 16 bits resolution is utilized. In the figure, it is assumed that the phase of the self-jamming wave is 0, that is $\phi_k = 0$. It can be observed that as the resolution increases, the cancellation factor is improved dramatically as the cancellation waveform is sampled with higher fidelity.

It is important to note that the initial phase difference before the cancellation is applied will play an important role in the cancellation as it will provide an offset that will move the sampling operation, thus potentially resulting in a perfect cancellation even in low resolutions. As an example, if $\phi_k = 60^o$ exactly and there is a state on the phase shifter that allows for a phase shift $phi_{\mathrm{canc}} = 120^o$, even if the phase shifter has a resolution of (say) 3 bits, the phase will be canceled optimally for this scenario. However, a crucial specification for adaptive system is to be able to adapt to a variety of conditions. As a result, the phase shifter as well as the attenuator should be able to cover a high range of impedances *with high fidelity*.
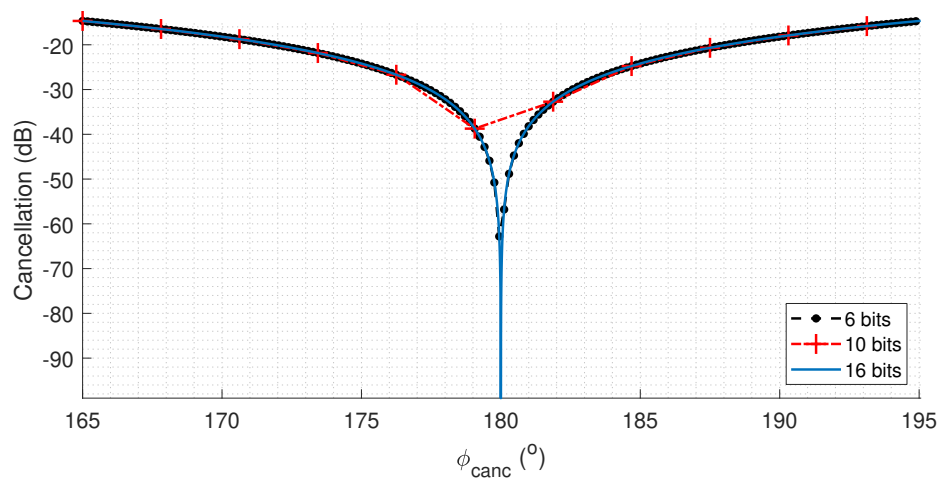
Figure 5.7: A slice from Fig. 5.4 that depicts the cancellation only with respect to phase. Assuming equal amplitudes and a $\phi_k = 0$, the self-jamming wave is cancelled optimally when $\phi_{\mathrm{canc}} = 180^o$. Phase shifters with better resolution provide better results in cancellation.

The relative phase between the cancelling and self-jamming wave is a random variable and in order to evaluate the contribution of increased resolution in the average and worst-case scenario cancellations, we conducted simulations that estimate and visualize the resolution-vs-cancellation. We simulated adding two sinusoids with one of the sinewaves acting as the cancellation wave with varying amplitude and phase, and the other was the self-jamming wave that had a constant phase of 0 degrees and an amplitude of 1. Then we scanned the amplitude and phase of the cancelling wave, added it to the self-jamming wave, and calculated the resulting power for each phase/attenuation pair. Finally, we simulated random initial phase/amplitude between self-jamming and cancelling

wave and proceeded to find the optimal cancelling phase, assuming a full-search algorithm [36] for different phase resolution levels, measured in bits.
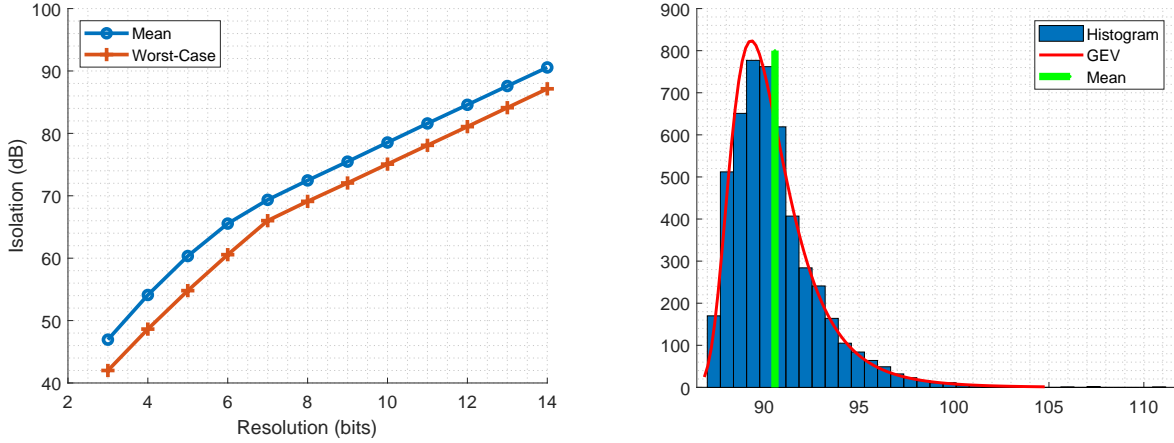
Figure 5.8: Left: Based on simulations, the average and worse-case-scenario cancellation (assuming a full- search algorithm) increases by up to 6 dB/bit Right: Distribution of the isolation for 12-bit resolution showing cancellation exhibits a GEV distribution.

The average cancellation and the worst case scenario for each resolution level among 10^5 iterations was found and the results are depicted in Fig. 5.8-left. The significance of the resolution is prominent: the average and the worst case cancellation increases by almost up to 6 db/bit. It is important to note again that every extra dB of cancellation that is achieved is directly translated in dB of RX gain and/or TX gain and a greatly reduced noise floor (see Fig. 5.2). This finding is very significant because it gives us a knob to tune and dramatically increase the performance of the receiver in a predictable manner.

The distribution of the isolation performance for a 12-bit resolution is shown in Fig. 5.8-right. Analysis using MATLAB's tool histfit revealed that the data exhibited a generalized extreme value (GEV) distribution [66]. The probability density function for the generalized extreme value distribution has 3 parameters: the location parameter μ, the scale parameter σ, and the shape parameter ξ and is defined as:

$$f(z) = \left(\frac{1}{\sigma}\right)\exp\left(-1(1+\xi z)^{-1/\xi}\right)\left(1+\xi z\right)^{\frac{-1}{\xi}-1},\tag{5.20}$$

where

$$z = \frac{x - \mu}{\sigma}, \quad x > \mu - \frac{\sigma}{\xi} \quad \text{for } \xi > 0. \tag{5.21}$$

Moreover, we estimated the distribution's parameters using MATLAB's gevfit() function as follows:

$$\xi = 0.112, \quad \sigma = 1.537, \quad \mu = 89.5. \tag{5.22}$$

It will be shown below that the measured results also exhibit a GEV distribution with the same mean but with higher spread. We postulated that the smaller spread in the simulation is due to the lack of noise and non-idealites such as the non-linearities of the analog RF components. Regardless, knowing the distribution of the performance, data points give us an important tool to understand the system better and improve it in the future.

5.3 Implementation

We implemented a self-jammer cancellation system using the approach described in the previous chapter. In particular, we implemented our system with a phase shifter and an attenuator in series that create a complex, variable impedance module that is controlled by a microcontroller. A detailed block diagram of the system is shown in Fig. 5.9, and a photo of the actual system is shown in Fig. 5.10.

5.3.1 Component selection

Careful research from a broad spectrum of components and architectures for each submodule was conducted for the final design. For the power detector, we utilized the Minicircuits ZX47-60+ RF amplifier and the Minicircuits ZX47-60+ power detector. The amplifier is used to increase the sensitivity of the detector from 60 dBm to a measured sensitivity of more than 90 dBm. This was a crucial improvement in order to detect the deep null that is a result of the wave cancellation described above. Intuitively, the self-jammer canceller would only be able to achieve a cancellation as low as the power that it can detect.

Two important components include the VLM-33-S+ [67] limiter and the ZX75BP-942+ [68] bandpass filter. The limiter cuts off any signal larger than 10 dBm and protects the sensitive circuits of the USRP. This is particularly useful when tests are conducted with the output-couple port of the coupler open/short or when the channel conditions are such that the received reflected
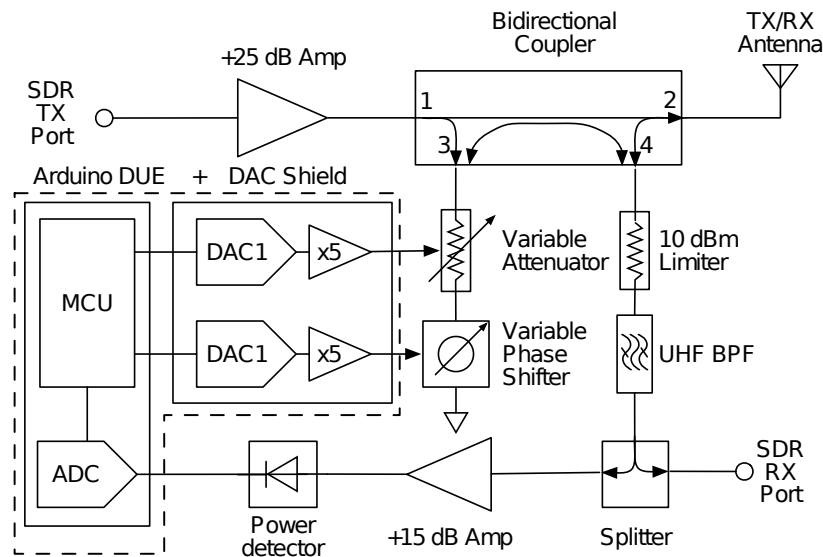
Figure 5.9: Self jammer-canceller implementation block diagram: An Arduino board controls the variable impedance load that is implemented with a phase shifter and an attenuator. The output couple port passes through a 10-dBm limiter for protection and a UHF BPF for rejecting harmonics from the USRP and out-of-band interference. The RX signal is then split and its power is measured and fed to the microcontroller for processing.

power is high. The band-pass filter with a pass-band of 875-1010 MHz is important so that the out-of-band noise and interference (e.g. from WiFi) is cut off and so as to eliminate the spurious harmonics from the USRP.

We also selected the Mini Circuits JSPHS-1000+ [65] voltage-variable phase shifter with a 180° range and a typical insertion loss of only 1.4 dB [65]. The phase shifter doesn't need to have 360° range due to the fact that the cancelling wave would have to travel twice inside the module. Thus, the phase shifting will be double. Moreover, the ZX73-2500+ [69] voltage-variable attenuator that was selected features a minimum insertion loss of approximately 3.3 dB [69] and a broad range of attenuation ranging from 3.3 dB-40 dB. Both components were selected due to their relatively low price and low insertion loss when compared to the competition. More importantly, they are both voltage-variable and not digitally controlled components. Therefore, we can control the phase and attenuation with arbitrarily low resolution depending on the DAC modules that are connected
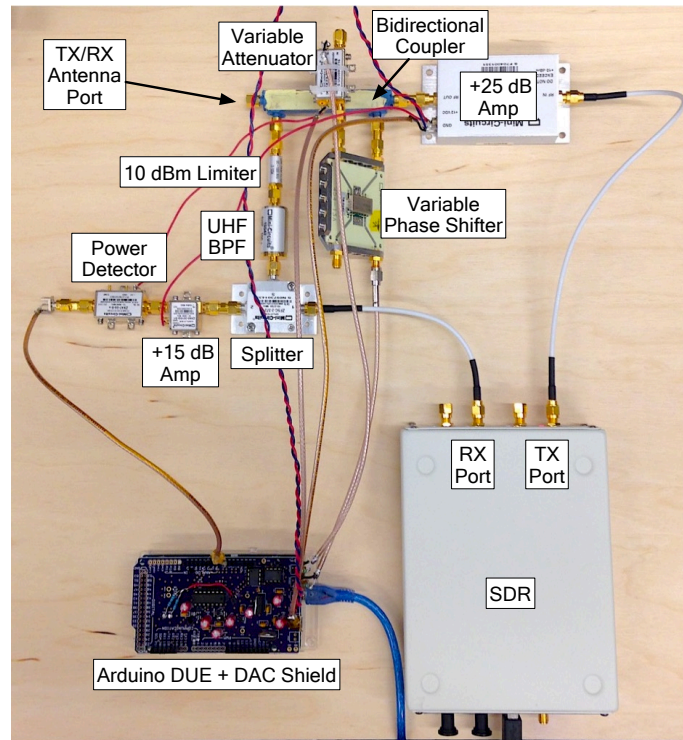
Figure 5.10: Implementation of the self-jammer canceller circuit connected to the USRP receiver.

at their inputs. Finally, the variable impedance load is terminated with a "short" load with an insertion loss of less than 1 dB.

For controlling the variable phase shifter and attenuator, we developed a custom Arduino shield that contains two MCP4725 12-bit digital-to-analog converters; one for controlling each RF module. However, the maximum output of the particular DACs is confined to 5.5 V and the RF modules require up to 15 V control and a current draw of up to 30 mA. Therefore, we incorporated on the shield appropriate non-inverting amplifier topology with a gain of x5 to accommodate the high voltage requirements. We also added buffers at the output of the gain amplifiers using the robust OPA604 for providing enough current to the RF modules. For the gain amplifiers, we utilized the TLC2274 amplifier and the OPA604 opamps as the buffers. The shield also contains three low drop out regulators (LDO) that generate the following signals: a 15 V signal that feeds the rails of the amplifiers, a 5 V signal that is used to power the Arduino board, and a 3.3 V signal that supplies
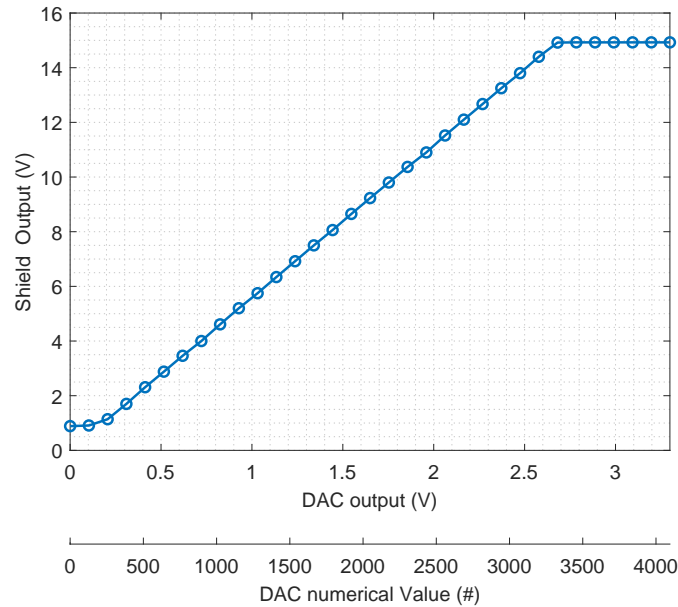
Figure 5.11: Characterization of the power custom driver shield. Due to resistance tolerances and limitations with the amplifiers, the DAC ENOB is reduced to 11.67 bits.

the DAC modules.

Fig. 5.11 shows the output of the custom driver with respect to the DAC output (both numerical and voltage). We can observe that the realized gain is actually x5.6, which is a result of the manufacturing tolerances in the feedback resistors. We can also observe that the output voltage starts from around 0.8 V and its maximum value is 1.48. This is because the amplifiers that were utilized are not rail-to-rail (neither output or input). As a result, the output of the driver limits the effective number of bits from 12 to 11.67.

Finally, we selected an Arduino DUE board that features an Atmel SAM3X8E ARM Cortex-M3 to implement the software for the control of the canceller. The particular microcontroller kit was chosen for its high clock speed of 86 MHz, which would allow for rapid tuning and an easy programming interface. The SAM3X8E ARM Cortex-M3 incorporates two embedded 12-bit DAC modules that were initially our choice for the signal conditioning. However, these DAC modules are not buffered and thus are very sensitive. After accidentally damaging the DAC modules on a couple of boards, we decided to utilize the more robust MCP4725.

5.3.2 Software implementation

One of the critical components of this work was the software that controls the circuitry described above. The software specifications that we optimized the software for are the speed of tuning and the self-jammer cancellation performance. The software was written using the Aruino language; a HAL for the ARM Cortex-M3 that is written in C/C++.

We implemented a simple but robust two-step full-search algorithm for fine tuning the impedance circuit. The algorithm is initialized to search within a limited range of phase-attenuation pairs that are determined based on experimentation in the particular environment that the communication link is established. For example, the environment of the Faraday cage described in the 3 is highly reflective, so a smaller attenuation is required to match the amplitude of the cancelling wave with the reflective wave. On the other hand, in an open-space environment, the attenuation of the cancelling wave needs to be higher since the self-jamming wave is typically weaker. Our algorithm contains predefined initialization settings for different environments based on our experimentation. Finally, we determined by measurement that the phase shifter exhibits a range larger than 180°; so we omitted unnecessary DAC outputs from the search to further speed up tuning.

The first step of the algorithm involves a coarse search to find the phase/attenuation pair that minimizes the received input power. Coarse searching reduces the execution time by reducing the sample space that the algorithm needs to search for the optimal phase/attenuation pair, among the $2^{12} \times 2^{12} = 16777216$ possible pairs. The step size is important - too small and the algorithm takes too long to execute, too large and the probability of missing the right window increases. In our case, a step size of 256 DAC (4 MSBs) values was determined experimentally to provide a good tradeoff between execution time and accuracy.

After finding the right phase/attenuation pair, the algorithm searches within a window around the identified pair using a finer step. In this step, the window size is important and exhibits a similar tradeoff as the coarse step size, i.e., a large window means higher execution time but smaller probability of missing the ideal phase/attenuation pair. After the optimal point is found, the algorithm can be executed again to adapt to potential channel changes. In quasi static channels, this solution works extremely well and, to the best of our knowledge, it achieves the best isolation performance when compared to prior art. It is important to note that a faster and more dynamic tuning is possible by continuously executing the search over a small moving window of phase/attenuation pairs. This way, non-static channels can be accommodated.

5.4   Experimental Results

We conducted extended measurements to characterize the self-jammer canceller and evaluate its performance. In particular, we characterized the achieved attenuation and phase resolution that are described as critical for the performance of the system. Moreover, we ran experiments to quantify the performance of the system over time and over multiple tuning iterations.

5.4.1   Performance of the RF modules
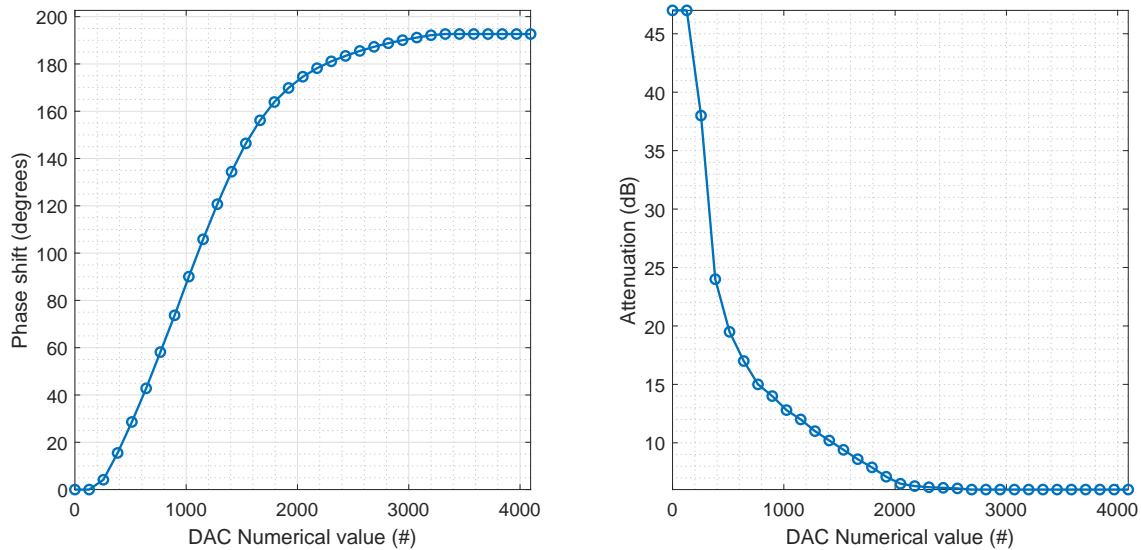
Figure 5.12: Phase and attenuation of the RF modules vs the DAC output.

We characterized the behavior of the RF modules with respect to the DAC output, and the results are shown in Fig. 5.12. The non-linear behavior of the circuits is prominent. However, since our software only needs to know the received power and does not require knowledge of the absolute phase or attenuation on any components of the system, the non-liner behavior of the phase shifter and the attenuator was not an issue. As long as the function of voltage vs phase/attenuation is monotonous, our system is able to tune.

As expected, the phase/attenuation resolution of the modules changes with input voltage. To evaluate the resolution, we measured the difference in phase/attenuation between each step of
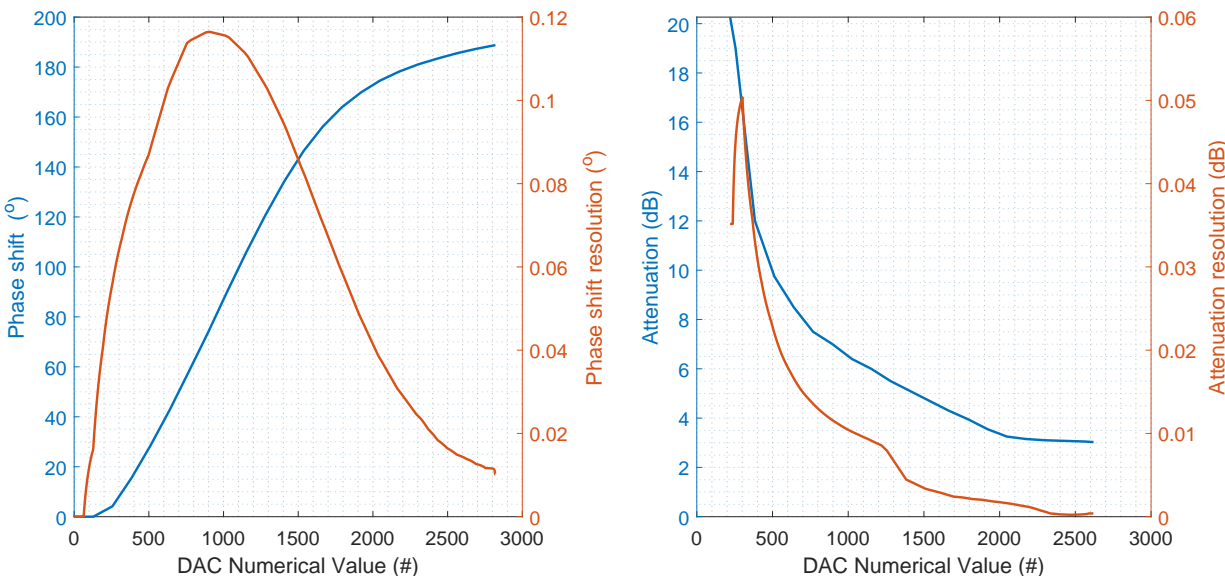
Figure 5.13: Effective Phase and attenuation of the RF modules vs the DAC output. The resolution for each module is also plotted, which is a function of the absolute phase/attenuation value.

the DAC across its full range and plotted the results in Fig. 5.13. In the figure, we omitted the DAC values for which the amplifiers have already hit the rails and values that aren't useful for the canceller, such as phase shifts larger than 180° and attenuation values higher than 20 dB (for most practical purposes, more than 20 dB is not used). As expected, the resolution changes with respect to the DAC output: for the phase shifter, the resolution range is from $0.015^o - 0.12^o$ and for the attenuator, it ranges from 0.12 dB in the 20 dB range and down to 0.0005 dB in the 3-5 dB range. Therefore, the absolute performance of the isolation module will change depending on the particular channel characteristics and more specifically, depending on the relationship between the cancelling and self-jamming wave.

A characterization plot for the power detector is depicted in Fig. 5.14. As mentioned earlier, we are utilizing a preamplifier to enhance the sensitivity of the power detector. The plot depicts the DC Voltage output of the detector vs the input power that was measured with the Arduino board. The benefit of using a preamplifier is obvious: the detector's minimum detectable power is decreased from approximately -60 dBm to approximately -87 dBm.
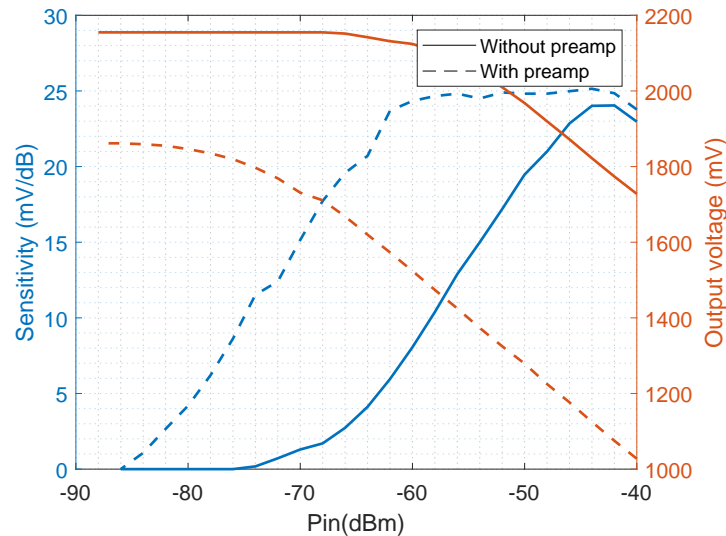
Figure 5.14: Characterization of the power detector with and without the preamplifier connected. The input power vs the ADC raw value as measured by the Arduino board is shown. It can be observed that the minimum detectable power decreased from approximately -60 dBm to -87 dBm.

5.4.2   System Performance Evaluation

As discussed in the previous sections, in order for optimal isolation to be achieved, the reflection coefficient of the variable load needs to be matched to the reflection coefficient of the antenna. Therefore, a broad range of impedances is important to be available to the canceler so that it can optimally perform tuning. Since this system was developed for use in an animal cage environment, we evaluated the performance of the variable load in the animal cage that was described in Chapter 4. Fig. 5.15 depicts the in blue 20000 out of the possible 2^24 antenna impedances that can be matched using the proposed system. The size of the occupied area is dependent on the cumulative insertion loss of the load that was measured at 6 dB. The lines in the plot show the measured impedance of the cage-side antenna over the full UHF band (902 MHz-928 MHz) with the saline tank that emulates the NHP installed on different levels. Moreover, there is an extra measurement (green line) that shows the S11 of the cage side antenna when the author was touching it to simulate potential contact between the monkey with it.
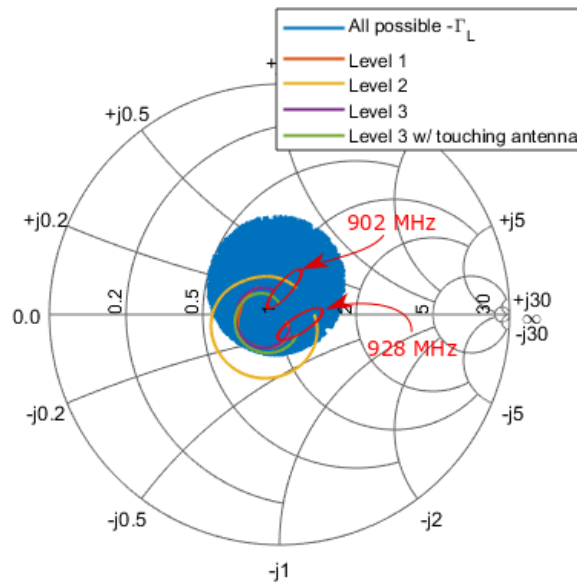
Figure 5.15: Measurements of reflection coefficient inside the animal cage for the entire UHF band (902 MHz-928 MHz).

We can observe that, aside from Level 2, for the rest of the configurations, the variable load is able to cover the necessary impedance to tune optimally. In Level 2, however, the user of the reader may select a CW with frequencies among the ones where the yellow line falls into the blue area (e.g 902 MHz) or install an attenuator before the antenna to bring the reflection coefficients closer to the center. This may seem like a counter-intuitive approach, but if we can have optimal isolation at the cost of only 1 dB attenuation, as described above, it can provide orders of magnitude and better receiver performance.

Repeatability results

We discussed in the above sections that the relationship between the self-jamming wave and the cancelling wave can determine the isolation performance. We provided an example for this wherein even a very low-resolution canceler may be able to cancel the self-jammer as the phase of the cancelling wave happened to be exactly the right value. We also discussed the importance of the resolution in the self jammer's performance and provided results that show the *average* and *worst-*

case cancellation in a simulation environment. This section provides characterization of real-world measurements to visualize and evaluate the statistical properties of the self-jammer canceller. To the best of our knowledge, this is the first time a self-jammer canceller is characterized in this way.
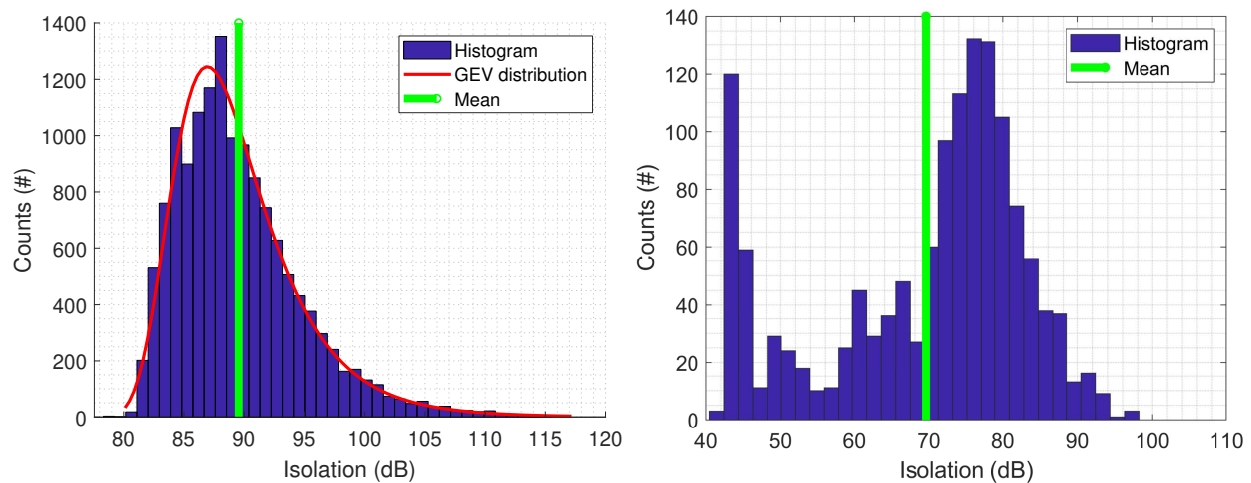
Figure 5.16: Repeatability measurements of the self-jammer canceller. Left: the canceller was terminated using a 50 Ohm load. Right: Repeatability measurements taken inside a mock animal cage with the appropriate cage-side antenna.

We began by characterizing the system with a 50 Ohm load connected instead of the antenna. This way, the static tuning of the system could be evaluated. We set the self-jammer canceller to tune the impedance of the load and implement the self-jammer cancellation repetitively. At the end of every tuning cycle, we measured the achieved isolation with a spectrum analyzer connected in place of the USRP RX. With known transmit power, we were able to measure the exact isolation by subtracting the transmitted from the received power.

Fig. 5.16-left depicts a histogram of the measurements; the data, as expected, fall into a GEV distribution similar to the one depicted in Fig. 5.8-right. The parameters of the distribution of the measured data were estimated using MATLAB's gevfit() function as

$$\xi = 0.047, \quad \sigma = 3.87, \quad \mu = 86.6 \tag{5.23}$$

The mean isolation is very close to the simulated results (87.6 dB) but the spread (σ) is higher. We believe that the difference in spread is due to the fact that we assumed no noise in the control

signals or the power detection and excluded non-idealities and non-linearities from the simulation of the RF components.

Moreover, Fig. 5.16-right shows a histogram of 1380 data points taken with the exact same procedure, but this time, the measurements were taken inside a mock cage made out of aluminum foil that was constructed to simulate the NHP cage. The channel inside the mock cage exhibits very chaotic behavior, so any small changes in the environment, including temperature changes, etc., result in severe changes in the reflection coefficient of the antenna. In a lot of these cases, the resulting reflection coefficient of the antenna was such that the isolation couldn't be optimal, since the variable impedance couldn't cover the specific impedance. This results in suboptimal tuning and is the reason for the occurence of this large spike of low isolation values on the left of Fig. 5.16-right.

Stability results
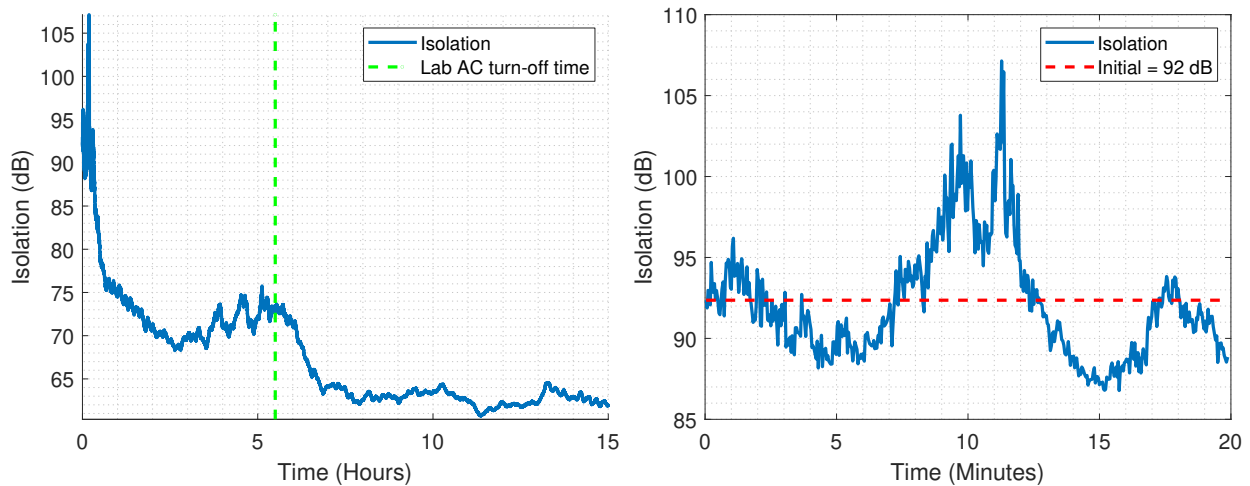
Figure 5.17: Stability measurements. Left: Measurements over 15 hours. Right: Zoomed-in view of the first 20 minutes.

The stability of the system over time was also characterized. As explained above, tuning is very sensitive to changes in phase that can occur even from environmental sources such as changes in temperature.

We evaluated the stability of the system by tuning the self-jammer canceller once using a 50 Ohm load in place of the antenna to exclude channel changes from the measurement. Using a 910 MHz CW at 15 dBm, we then measured the resulting isolation with the SA every 2.67 seconds over 16.09 hours, resulting in a total of 21666 data points. The data is depicted in Fig. 5.17.

Initially, the isolation was tuned to 92 dB. After around 10 minutes into the experiment, the isolation rose to approximately 107 dB (see Fig. 5.17)-right. This is due to the fact that the parasitic change in phase/attenuation from environmental changes and drift in the electronic components induced a *positive* effect on the isolation. However, after the first 10 minutes, the isolation started to drop dramatically, resulting in a drop to 75 dB from 107 -dB after around 40 minutes. Moreover, at hour 5, the isolation dropped to an average of 62 dB and stabilized. Around $t = 5$ hours, the AC in the laboratory that the experiment was taking place was turned off, resulting in a change in phase/attenuation and a reduction in isolation.

The overall change in isolation was from an initial of 107 dB to a minimum of 60 dB, i.e., a change of 47 dB. However this change was induced over a period of 15 hours. On Fig. 5.17-right, we can observe that the isolation is always above 86 dB for the first 20 minutes and it was also stable within 0.5 dB for the first 30 seconds. We can conclude then that in a quasi-static channel, we can safely tune every few seconds to achieve stable isolation over time.

5.4.3   Prior Art

As demonstrated above, self-jammer cancellation is one of the fundamental challenges with backscatter communication systems due to the detrimental effect that the self-jammer signal can have on the performance of the receivers. As a result, significant research efforts have been taken to address the problem in various applications, including radio frequency identification (RFID) tag industry [70, 71, 44, 72, 73, 74, 75, 76, 77, 78], radar [79, 80], and full duplex wireless communication [81, 82, 83]. A comprehensive survey of the prior art on self-jammer cancellation is provided in [36].

A few notable contributions primarily from the UHF RFID literature and a comparison with the system from this work are summarized in Table 5.1.

Authors of [36] developed a similar architecture with the one presented in this work, employing a reflective load at the input-couple port of the directional coupler. However, they only employed a static manually-tuned reflective load that confines the isolation to only 50 dB.

In [75], the CW is modulated using a vector modulator IC and injected into the RX path so as to cancel the leaked carrier. Similar methods are employed frequently in the literature with

Table 5.1: Self-jammer cancellation literature review. Adapted from [36].

Reference	Application	Type	Isolation (dB)
This work	BCI backscatter	Digitally controlled reflective load	average 90
[36]	UHF RFID	Coupler w/ static reflective load	up to 50
[80]	FMCW Radar	Continuous adaptive cancellation	41-46
[75]	UHF RFID	Vector modulation of carrier	up to 70
[74]	UHF RFID	Vector modulation PLL	up to 80
[84]	Full duplex radio	Qhx220 Interference canceller	45
[76]	UHF RFID	2x Active vector modulators	73

promising results. However, one fundamental drawback of such approaches is that the modules that are utilized for vector modulation are active and they introduce their own noise figure into the system. In our work, the modules that are utilized to control the phase and the attenuation of the carrier are passive (in the RF path) so they don't introduce extra noise in the receive path.

Finally, one can observe that our work outperforms similar systems in the literature by at least 10 dB. Like we mentioned earlier, this is due to the higher resolution in the control of the load impedance when compared to the results in the literature on increased performance. Moreover, to the best of our knowledge, the analysis regarding the statistical properties of the isolation with respect to the resolution or results regarding stability and repeatability are unique in the literature and are one of the important contributions of this thesis.

5.5 Conclusion

This section presented the development of a novel self-jammer cancellation system. The system consists of a bidirectional coupler with its input coupled port terminated with a variable impedance load that reflects a portion of the transmitted CW into the output-couple port. This operation results in the cancellation of the self-jammer wave by tuning the variable impedance load.

The variable impedance load is controlled by an Arduino DUE board that runs at an 80 MHz clock. The Arduino board runs a full-search algorithm and is connected to a custom shield that powers and controls the variable impedance load using commercial of the shelf 12-bit DACs. The variable impedance load is implemented with a voltage-variable phase shifter and a voltage-variable

attenuator.

One of the fundamental advantages of this approach is that the self-jammer canceller has a high resolution for tuning the variable impedance load and thus achieves a high cancellation performance. Analyses and simulations of the resolution vs the average and worst-case cancellation are provided. Moreover, the system was characterized in terms of its stability and repeatability in realistic environments and its performance demonstrated good agreement between simulation and measurement.

Finally, our work features the highest reported self-jammer cancellation performance in the literature. Furthermore, to the best of our knowledge, this work is the first to provide measured repeatability and stability results along with analyses and measurements of the resolution vs cancellation.

5.5.1   Future Work

The components of the self-jammer cancellation system can be utilized for the development of a novel backscatter communication testbed. The variable impedance load in combination with the custom controller and Arduino shield could be utilized to emulate complex backscatter communication modulations since the load can be tuned to virtually any impedance inside the circle of the smith chart plot, as shown in Fig. 5.15. For example, M-ary backcatter constellations for high-data-rates [20] or pulse shaping of the reflected carrier could be tested with ease [85].

Finally, the software flexibility of the Arduino firmware as well as its high computation performance allows for the implementation of various fast algorithms such as gradient descent and others. Such algorithms would improve the performance of the receiver inside the metal animal cage environment like the one described in Chapter 4, because the self-jammer canceller needs to adapt rapidly to channel changes due to the chaotic nature of the cage.

Chapter 6

CONCLUSION AND FUTURE WORK

6.1   Conclusion

This work presents the development of a suite of brain-computer interfaces leveraging backscatter communication. Particularly, in the first chapter, we elaborate on the necessity of high data-rate backscatter wireless communication systems that serve to miniaturize and lower the power consumption of brain-computer interfaces. We showed through comparative reviews that there are little to no examples of wireless BCIs that demonstrate small size, low power *and*, high data-rate uplink performance.

We proceed in the second chapter to describe a system that leverages frequency translation techniques in order to re-use existing neural acquisition IC infrastructure for recording ECoG signals. Particularly, we demonstrated a frequency translation method that reduces the 3-dB cutoff from 12 Hz to 0.015 Hz, which can be achieved with only 56 μW with no cost or added noise. The development of this system facilitated an understanding of the nature of neural signals from an electrical engineering standpoint. Moreover, while working on the frequency translation, we developed testbeds and receivers for low-power, wireless neural signal acquisition that laid the groundwork for developing more advanced BCIs, as discussed below.

In Chapter 3, we described the development of a fully integrated wireless implantable BCI that leverages backscatter communication. Particularly, the developed system utilizes a dual-band antenna and circuitry to implement both a 5 Mbps uplink at the UHF band and a 50% efficient wireless power transfer link at the HF band. The backscattered signals are demodulated in real-time from a custom SDR receiver at a rate of up to 5 Mbps. The implant was tested using emulated tissue using saline proxy and we demonstrated a PER of less than .5% at a depth of 3 cm; the highest reported in the literature for backscatter BCI systems at this frequency was this.

Chapter 4 proposes a wireless BCI for acquiring neural signals from non-human primates (NHP) inside their home cage. The developed BCI upgrades the Neurochip 3 to add wireless backscatter communication at 25 Mbps. More importantly, a characterization of the reverberant cavity channel

inside the animal cage was conducted using real-world measurements. Specifically, we demonstrated that only 1 out of the 126 measurement points exhibit a non-zero PER. This result indicates that backscatter communication can be utilized for reliable and high data-rate communication inside the cage despite the deep fading nulls that are introduced due to cavity effects from the metal structure of the cage. Finally, we validated the practical useability of the system by conducting a series of in-vivo experiments, which indicated that the proposed approach can be utilized for acquiring LFP and high frequency AP signals from live animals.

In Chapter 5, we proposed a novel mixed signal approach for self-jammer cancellation approach. The system we developed utilizes a classic self-jammer cancellation architecture with a bidirectional coupler and a reflective load for matching the reflection coefficient of the transmit antenna and cancelling the self-jamming wave. However, in contrast to prior art, our approach utilizes analog components for the reflective load that are controlled by 12-bit resolution DACs. The high control resulting resolution allows for an average isolation performance on the order of 89 dB, which is 10 dB higher than similar approaches in the literature. Moreover, unlike in prior art, the system was characterized using a statistical approach instead of taking just one measurement.

The methods and systems that are developed for this thesis, along with the corresponding results, were published in IEEE peer-reviewed conferences and journals that validate the novelty and value of the proposed approaches.

6.2   Future Work

Research groups around the world are collaborating to develop more sophisticated backscatter communication systems, and the field of brain computer interfacing is exhibiting an exponential growth. The future is bright and exciting. There are numerable applications and future directions that the work of this thesis can be expanded to. We are going to outline just a small subject of the exciting realm of possibilities in this section.

6.2.1   Backscatter comms-enabled BCI ASIC

The most straightforward way to enhance the work of this thesis would be to implement a large set of the functions developed throughout it on a single application-specific integrated circuit. For the implant system developed in Chapter 3, we could expand the capabilities of the already implemented ASIC to integrate DQPSK backscatter capabilities and higher data-rates and neural stimulation. The new ASIC could be then utilized with the system developed in Chapter 4 to develop a much

smaller BCI for neural monitoring in primates. Moreover, the whole self-jammer canceller system developed in Chapter 5 could also be integrated into a single ASIC that includes control and RF circuitry for a more compact fast and effective approach.

6.2.2 Higher data-rates

As outlined in the introduction of this thesis, higher data-rate are of primary importance in BCIs. This work has paved the road for low-power communication systems in BCIs, but a lot more work needs to be done to improve data-rates. Using higher-order (e.g. 16 QAM) constellations similar to the ones developed in [20], we can achieve data-rates on the orders of hundreds of Mbps with under 100 pJ/bit. This will come at the cost of a less favorable link quality due to the losses that a smaller modulation factor will introduce. As a result, a more sophisticated receiver that can process much higher instantaneous bandwidth would have to be employed with higher sensitivity.

6.2.3 Backscatter Bluetooth/WiFi BCIs

Recently, researchers at the University of Washington demonstrated that backscatter communications can be utilized with commodity communication systems such as WiFi [86] and Bluetooth [87]. This new technology can be utilized to develop BCIs that will not require custom readers such as the one developed for the purposes of this work. In contrast, neuroscientists would be able to utilize off-the-shelf receivers to demodulate neural data, thus further facilitating neuroscience research and particularly the use of wireless BCIs.

BIBLIOGRAPHY

[1] N. Bhadra and K. L. Kilgore, "High-frequency electrical conduction block of mammalian peripheral motor nerve," *Muscle & Nerve*, vol. 32, no. 6, pp. 782–790, 2005.

[2] K. Birmingham, V. Gradinaru, P. Anikeeva, W. M. Grill, V. Pikov, B. McLaughlin, P. Pasricha, D. Weber, K. Ludwig, and K. Famm, "Bioelectronic medicines: a research roadmap," *Nature Reviews Drug Discovery*, vol. 13, no. 6, pp. 399–400, 2014.

[3] L. R. Hochberg, D. Bacher, B. Jarosiewicz, N. Y. Masse, J. D. Simeral, J. Vogel, S. Haddadin, J. Liu, S. S. Cash, P. van der Smagt *et al.*, "Reach and grasp by people with tetraplegia using a neurally controlled robotic arm," *Nature*, vol. 485, no. 7398, p. 372, 2012.

[4] A. B. Ajiboye, F. R. Willett, D. R. Young, W. D. Memberg, B. A. Murphy, J. P. Miller, B. L. Walter, J. A. Sweet, H. A. Hoyen, M. W. Keith *et al.*, "Restoration of reaching and grasping movements through brain-controlled muscle stimulation in a person with tetraplegia: a proof-of-concept demonstration," *The Lancet*, vol. 389, no. 10081, pp. 1821–1830, 2017.

[5] J. L. Collinger, B. Wodlinger, J. E. Downey, W. Wang, E. C. Tyler-Kabara, D. J. Weber, A. J. McMorland, M. Velliste, M. L. Boninger, and A. B. Schwartz, "High-performance neuroprosthetic control by an individual with tetraplegia," *The Lancet*, vol. 381, no. 9866, pp. 557–564, 2013.

[6] R. Muller, "Low-power, scalable platforms for implantable neural interfaces," Ph.D. dissertation, University of California, Berkeley, 2013.

[7] R. Muller, H.-P. Le, W. Li, P. Ledochowitsch, S. Gambini, T. Bjorninen, A. Koralek, J. M. Carmena, M. M. Maharbiz, E. Alon, and J. M. Rabaey, "A Minimally Invasive 64-Channel Wireless μECoG Implant," *IEEE J. Solid-State Circuits*, vol. 50, no. 1, pp. 344–359, 2015.

[8] G. Schalk, "Can electrocorticography (ECoG) support robust and powerful brain-computer interfaces?" *Frontiers in Neuroengineering*, vol. 3, pp. 9–10, Jan 2010.

[9] E. M. Maynard, C. T. Nordhausen, and R. A. Normann, "The Utah intracortical electrode array: A recording structure for potential brain-computer interfaces," *Electroencephalography and Clinical Neurophysiology*, vol. 102, no. 3, pp. 228 – 239, 1997.

[10] A. Jackson, J. Mavoori, and E. E. Fetz, "Correlations between the same motor cortex cells and arm muscles during a trained task, free behavior, and natural sleep in the Macaque monkey," *Physiology*, vol. 97, no. 1, pp. 360–374, Jan. 2007.

[11] I. H. Stevenson and K. P. Kording, "How advances in neural recording affect data analysis," *Nature Neuroscience*, vol. 14, no. 2, pp. 139–142, 2011.

[12] D. Seo, R. M. Neely, K. Shen, U. Singhal, E. Alon, J. M. Rabaey, J. M. Carmena, and M. M. Maharbiz, "Wireless recording in the peripheral nervous system with ultrasonic neural dust," *Neuron*, vol. 91, no. 3, pp. 529–539, 2016.

[13] W. Biederman, D. J. Yeager, N. Narevsky, A. C. Koralek, J. M. Carmena, E. Alon, and J. M. Rabaey, "A fully-integrated, miniaturized (0.125 mm^2) 10.5 μW wireless neural sensor," *IEEE J. Solid-State Circuits*, vol. 48, no. 4, pp. 960–970, April 2013.

[14] H. N. Schwerdt, W. Xu, S. Shekhar, A. Abbaspour-Tamijani, B. C. Towe, F. A. Miranda, and J. Chae, "A fully passive wireless microsystem for recording of neuropotentials using RF backscattering methods," *J. Microelectromechanical Systems*, vol. 20, no. 5, pp. 1119–1130, Oct 2011.

[15] A. Kiourti, C. W. L. Lee, J. Chae, and J. L. Volakis, "A wireless fully passive neural recording device for unobtrusive neuropotential monitoring," *IEEE Trans. Biomedical Engineering*, vol. 63, no. 1, pp. 131–137, Jan 2016.

[16] J. Charthad, M. J. Weber, T. C. Chang, and A. Arbabian, "A mm-sized implantable medical device (IMD) with ultrasonic power transfer and a hybrid bi-directional data link," *IEEE J. Solid-State Circuits*, vol. 50, no. 8, pp. 1741–1753, Aug 2015.

[17] D. A. Schwarz, M. A. Lebedev, T. L. Hanson, D. F. Dimitrov, G. Lehew, J. Meloy, S. Rajangam, V. Subramanian, P. J. Ifft, Z. Li *et al.*, "Chronic, wireless recordings of large-scale brain activity in freely moving rhesus monkeys," *Nature methods*, vol. 11, no. 6, p. 670, 2014.

[18] J. F. Ensworth and M. S. Reynolds, "BLE-Backscatter: Ultralow-power IoT nodes compatible with bluetooth 4.0 low energy (BLE) smartphones and tablets," *IEEE Transactions on Microwave Theory and Techniques*, vol. 65, no. 9, pp. 3360–3368, Sept 2017.

[19] S. Zanos, A. G. Richardson, L. Shupe, F. P. Miles, and E. E. Fetz, "The Neurochip-2: an autonomous head-fixed computer for recording and stimulating in freely behaving monkeys," *IEEE Trans. Neural Syst. Rehabil. Eng.*, vol. 19, no. 4, pp. 427–435, 2011.

[20] S. J. Thomas and M. S. Reynolds, "A 96 Mbit/sec, 15.5 pJ/bit 16-QAM modulator for UHF backscatter communication," in *Proc. 2012 IEEE Intl. Conf. RFID (RFID 12)*, Apr. 2012, pp. 185–190.

[21] J. D. Griffin and G. D. Durgin, "Complete link budgets for backscatter-radio and RFID systems," *IEEE Antennas and Propagation Magazine*, vol. 51, no. 2, pp. 11–25, April 2009.

[22] J. S. Besnoff and M. S. Reynolds, "Near field modulated backscatter for in vivo biotelemetry," in *Proc. 2012 IEEE Intl. Conf. RFID (RFID 12)*, Apr. 2012, pp. 135–140.

[23] S. J. Thomas, R. R. Harrison, A. Leonardo, and M. S. Reynolds, "A battery-free multichannel digital neural/EMG telemetry system for flying insects," *IEEE Trans. Biomed. Circuits Syst.*, vol. 6, no. 5, pp. 424–436, Oct 2012.

[24] J. Charthad, M. J. Weber, T. C. Chang, and A. Arbabian, "A mm-sized implantable medical device (IMD) with ultrasonic power transfer and a hybrid bi-directional data link," *IEEE J. Solid-State Circuits*, vol. 50, no. 8, pp. 1741–1753, Aug 2015.

[25] M. M. Maharbiz, R. Muller, E. Alon, J. M. Rabaey, and J. M. Carmena, "Reliable next-generation cortical interfaces for chronic Brain-Machine interfaces and neuroscience," *Proc. of the IEEE*, vol. 105, no. 1, pp. 73–82, Jan 2017.

[26] H. Ando, K. Takizawa, T. Yoshida, K. Matsushita, M. Hirata, and T. Suzuki, "Wireless multichannel neural recording with a 128-mbps uwb transmitter for an implantable brain-machine interfaces," *IEEE Trans. Biomed. Circuits Syst.*, vol. 10, no. 6, pp. 1068–1078, Dec 2016.

[27] T. A. Szuts, V. Fadeyev, S. Kachiguine, A. Sher, M. V. Grivich, M. Agrochão, P. Hottowy, W. Dabrowski, E. V. Lubenov, A. G. Siapas *et al.*, "A wireless multi-channel neural amplifier for freely moving animals," *Nature Neuroscience*, vol. 14, no. 2, p. 263, 2011.

[28] D. A. Borton, M. Yin, J. Aceros, and A. Nurmikko, "An implantable wireless neural interface for recording cortical circuit dynamics in moving primates," *Journal of neural engineering*, vol. 10, no. 2, pp. 26–36, 2013.

[29] H. Miranda, V. Gilja, C. A. Chestek, K. V. Shenoy, and T. H. Meng, "HermesD: A high-rate long-range wireless transmission system for simultaneous multichannel neural recording applications," *IEEE Trans. Biomed. Circuits Syst.*, vol. 4, no. 3, pp. 181–191, June 2010.

[30] E. Kampianakis, A. Sharma, J. Arenas, and M. S. Reynolds, "A dual-band wireless power transfer and backscatter communication approach for real-time neural/EMG data acquisition," *IEEE Journal of Radio Frequency Identification*, vol. 1, no. 1, pp. 100–107, March 2017.

[31] E. Kampianakis, A. Sharma, J. Rosenthal, and M. S. Reynolds, "Wideband UHF DQPSK backscatter communication in reverberant cavity animal cage environments," *IEEE Trans. on Antennas and Propagation (TAP), Special Issue on Biomedical Communication Systems*, March 2018.

[32] E. Kampianakis and M. S. Reynolds, "A biosignal analog front-end leveraging frequency translation," in *Proc. IEEE SENSORS*, Oct 2017, pp. 1–3.

[33] F. Zhang, A. Mishra, A. G. Richardson, and B. Otis, "A low-power ECoG/EEG processing IC with integrated multiband energy extractor," *IEEE Trans. Circuits Syst. I*, vol. 58, no. 9, pp. 2069–2082, 2011.

[34] A. Mahajan, A. K. Bidhendi, P. T. Wang, C. M. McCrimmon, C. Y. Liu, Z. Nenadic, A. H. Do, and P. Heydari, "A 64-channel ultra-low power bioelectric signal acquisition system for brain-computer interface," in *Biomedical Circuits and Systems Conference (BioCAS), 2015 IEEE*, Oct 2015, pp. 1–4.

[35] P. Hottowy, A. Skoczen, D. E. Gunning, S. Kachiguine, K. Mathieson, A. Sher, P. Wikcek, A. M. Litke, and W. Dka browski, "Properties and application of a multichannel integrated circuit for low-artifact, patterned electrical stimulation of neural tissue," *Journal of neural engineering*, vol. 9, no. 6, pp. 66–71, 2012.

[36] A. Boaventura, J. Santos, A. Oliveira, and N. B. Carvalho, "Perfect isolation: dealing with self-jamming in passive RFID systems," *IEEE Microwave Magazine*, vol. 17, no. 11, pp. 20–39, Nov 2016.

[37] N. M. Neihart and R. R. Harrison, "Micropower Circuits for Bidirectional Wireless Telemetry in Neural Recording Applications," *IEEE Trans. Biomed. Eng.*, vol. 52, no. 11, pp. 1950–1959, Nov 2005.

[38] A. P. Sample, D. T. Meyer, and J. R. Smith, "Analysis, experimental results, and range adaptation of magnetically coupled resonators for wireless power transfer," *IEEE Trans. Ind. Electron*, vol. 58, no. 2, pp. 544–554, Feb 2011.

[39] X. Li, C. Y. Tsui, and W. H. Ki, "A 13.56 MHz wireless power transfer system with reconfigurable resonant regulating rectifier and wireless power control for implantable medical devices," *IEEE J. Solid-State Circuits*, vol. 50, no. 4, pp. 978–989, April 2015.

[40] A. Sharma, E. Kampianakis, and M. S. Reynolds, "A dual-band HF and UHF antenna system for implanted neural recording and stimulation devices," *IEEE Antennas Wireless Propag. Lett.*, vol. 16, pp. 493–496, Jun 2016.

[41] T. W. Rondeau, V. Shelburne, and V. O'Shea, "Designing anaylsis and synthesis filterbanks in GNURadio," in *Karlsruhe Workshop on Software Radios*, 2014.

[42] J. P. Costas, "Synchronous Communications," *Proc. IRE*, vol. 44, no. 12, pp. 1713–1718, Dec. 1956.

[43] D. M. Dobkin, *The RF in RFID: Passive UHF RFID in Practice.* Newnes (Elsevier), 2008.

[44] J. Carrick, R. Herold, M. Reynolds, Y. Maguire, and R. Pappu, "Methods and apparatus for self-jamming suppression in a radio frequency identification (RFID) reader," U.S. Patent 20 100 069 011, Mar. 18, 2010.

[45] M. Koller and R. Kung, "Adaptive carrier supression for UHF RFID using digitally tunable capacitors," in *Proc. IEEE EUCAP*, Gothenborg, Sweden, Oct 2013, pp. 943–946.

[46] J. Y. Jung, C. W. Park, and K. W. Yeom, "A novel carrier leakage suppression front-end for UHF rfid reader," *IEEE Trans. Microw. Theory Techn.*, vol. 60, no. 5, pp. 1468–1477, May 2012.

[47] R. Merletti, "Standards for reporting EMG data," *J. Electromyogr. Kinesiol.*, vol. 9, pp. 3–4, 1999.

[48] E. V. Evarts, "Temporal patterns of discharge of pyramidal tract neurons during sleep and waking in the monkey," *Physiology*, vol. 27, no. 2, pp. 152–171, Mar. 1964.

[49] A. P. Georgopoulos, J. F. Kalaska, R. Caminiti, and J. T. Massey, "On the relations between the direction of two-dimensional arm movements and cell discharge in primate motor cortex," *Journal of Neuroscience*, vol. 2, no. 11, pp. 1527–1537, 1982.

[50] P. D. Cheney and E. E. Fetz, "Functional classes of primate corticomotorneuronal cells and their relation to active force," *Journal of Neurophysiology*, vol. 44, no. 4, pp. 773–791, 1980.

[51] T. N. Aflalo and M. S. A. Graziano, "Partial tuning of motor cortex neurons to final posture in a free-moving paradigm," *Proceedings of the National Academy of Sciences of the United States of America*, vol. 103, no. 8, pp. 2909–2914, Feb. 2006.

[52] D. W. Moran and A. B. Schwartz, "Motor cortical representation of speed and direction during reaching," *Journal of Neurophysiology*, vol. 82, no. 5, pp. 2676–2692, Nov. 1999.

[53] B. R. Townsend, L. Paninski, and R. N. Lemon, "Linear encoding of muscle activity in primary motor cortex and cerebellum," *Journal of Neurophysiology*, vol. 96, no. 5, pp. 2578–2592, Nov. 2006.

[54] T. Libery and E. E. Fetz, "Open-source, low cost, free-behavior monitoring, and reward system for neuroscience research in non-human primates," *Frontiers in Neuroscience*, vol. 11, p. 265, 2017.

[55] M. Yin, D. A. Borton, J. Aceros, W. R. Patterson, and A. V. Nurmikko, "A 100-channel hermetically sealed implantable device for chronic wireless neurosensing applications," *IEEE Transactions on Biomedical Circuits and Systems*, vol. 7, no. 2, pp. 115–128, April 2013.

[56] X. Liu, M. Zhang, A. G. Richardson, T. H. Lucas, and J. V. der Spiegel, "Design of a closed-loop, bidirectional brain machine interface system with energy efficient neural feature extraction and PID control," *IEEE Transactions on Biomedical Circuits and Systems*, vol. 11, no. 4, pp. 729–742, Aug 2017.

[57] C. T. Moritz, S. I. Perlmutter, and E. E. Fetz, "Direct control of paralysed muscles by cortical neurons," *Nature*, vol. 456, no. 7222, p. 639, 2008.

[58] J. G. McPherson, R. R. Miller, and S. I. Perlmutter, "Targeted, activity-dependent spinal stimulation produces long-lasting motor recovery in chronic cervical spinal cord injury," *Proceedings of the National Academy of Sciences*, vol. 112, no. 39, pp. 12 193–12 198, 2015.

[59] P. V. Nikitin, K. V. S. Rao, and R. D. Martinez, "Differential RCS of RFID tag," *Electronics Letters*, vol. 43, no. 8, pp. 431–432, 2007.

[60] J. G. Proakis and M. Salehi, *Fundamentals of communication systems.* Pearson Education India, 2007.

[61] Analog devices . AD9364 Noise Figure vs. Gain Index Plots. [Online]. Available: https://ez.analog.com/wide-band-rf-transceivers/design-support/w/documents/10073/noise-figure-vs-gain-index-plots

[62] E. M. Maynard, C. T. Nordhausen, and R. A. Normann, "The Utah intracortical electrode array: a recording structure for potential brain-computer interfaces," *Electroencephalography and clinical neurophysiology*, vol. 102, no. 3, pp. 228–239, 1997.

[63] F. J. Chaure, H. G. Rey, and R. Quian Quiroga, "A novel and fully automatic spike-sorting implementation with variable number of features," *Journal of Neurophysiology*, vol. 120, no. 4, pp. 1859–1871, 2018.

[64] RFLambda. RFPSHT0701D6 Digital 360 Degrees Phase Shifter Datasheet. [Online]. Available: http://rflambda.com/pdf/digitalcontrolphaseshifter/RFPSHT0701D6.pdf

[65] Mini Circuits . JSPHS-1000+ Voltage Variable Phase Shifter Datasheet. [Online]. Available: https://www.minicircuits.com/pdfs/JSPHS-1000+.pdf

[66] G. Muraleedharan, C. G. Soares, C. Lucas, and L. Wright, "Characteristic and moment generating functions of generalised extreme value distribution (GEV)," *Sea Level Rise, Coastal Engineering, Shorelines and Tides*, pp. 269–276, 2011.

[67] Mini Circuits . VLM-33-S+, +10 dBm RF limiter. [Online]. Available: https://www.minicircuits.com/pdfs/VLM-33-S+.pdf

[68] ——. ZX75BP-942+ UHF Bandpass filter. [Online]. Available: https://www.minicircuits.com/pdfs/ZX75BP-942+.pdf

[69] ——. ZX73-2500+ Voltage Variable Attenuator Datasheet. [Online]. Available: https://www.minicircuits.com/pdfs/ZX73-2500+.pdf

[70] R. Langwieser, G. Lasser, C. Angerer, M. Rupp, and A. L. Scholtz, "A modular UHF reader frontend for a flexible RFID testbed," in *Proc. 2nd Intl. European Association for Signal Processing (EURASIP) Workshop on RFID Technology*, 2008.

[71] J. Posamentier, "Radio frequency identification apparatus, system and method adapted for self-jammer cancellation," U.S. Patent 7 684 751, Mar. 23, 2010.

[72] S. Chiu, M. Sajid, and I. Kipnis, "Canceling self-jammer signals in an RFID system," U.S. Patent 8 013 715, Sep. 6, 2011.

[73] I. Mayordomo and J. Bernhard, "Implementation of an adaptive leakage cancellation control for passive UHF RFID readers," in *Proc. IEEE International Conference on radio frequency identification (RFID)*, 2011, pp. 121–127.

[74] D. P. Villame and J. S. Marciano, "Carrier suppression locked loop mechanism for UHF RFID readers," in *Proc. 2010 IEEE International Conference on radio frequency identification (RFID)*, 2010, pp. 141–145.

[75] G. Lasser, R. Langwieser, and A. L. Scholtz, "Broadband suppression properties of active leaking carrier cancellers," in *Proc. IEEE International Conference on radio frequency identification (RFID)*, April 2009, pp. 208–212.

[76] R. Langwieser, G. Lasser, C. Angerer, M. Fischer, and A. L. Scholtz, "Active carrier compensation for a multi-antenna RFID reader frontend," in *Proc. IEEE International Microwave Symposium (MTT-S)*, May 2010, pp. 1532–1535.

[77] T. Brauner and X. Zhao, "A novel carrier suppression method for RFID," *IEEE Microwave and Wireless Components Letters*, vol. 19, no. 3, pp. 128–130, March 2009.

[78] M. Koller and R. Küng, "Adaptive carrier supression for UHF RFID using digitally tunable capacitors," in *Proc. European Microwave Conference*, Oct 2013, pp. 943–946.

[79] K. Lin, Y. E. Wang, C. Pao, and Y. Shih, "A *ka*-band FMCW radar front-end with adaptive leakage cancellation," *IEEE Transactions on Microwave Theory and Techniques*, vol. 54, no. 12, pp. 4041–4048, Dec 2006.

[80] Z. Li and K. Wu, "On the leakage of FMCW radar front-end receiver," in *Proc. Global Symposium on Millimeter Waves*, April 2008, pp. 127–130.

[81] A. Sabharwal, P. Schniter, D. Guo, D. W. Bliss, S. Rangarajan, and R. Wichman, "In-band full-duplex wireless: Challenges and opportunities," *IEEE Journal on Selected Areas in Communications*, vol. 32, no. 9, pp. 1637–1652, Sept 2014.

[82] M. Jain, J. I. Choi, T. Kim, D. Bharadia, S. Seth, K. Srinivasan, P. Levis, S. Katti, and P. Sinha, "Practical, real-time, full duplex wireless," in *Proc. 17th Annual International Conference on Mobile Computing and Networking*, 2011, pp. 301–312.

[83] M. Jain, "Single channel full-duplex radios," Ph.D. dissertation, Dept. Elec. Eng., Stanford Univ., CA, Tech., 2012.

[84] M. Jain, J. I. Choi, T. Kim, D. Bharadia, S. Seth, K. Srinivasan, P. Levis, S. Katti, and P. Sinha, "Practical, real-time, full duplex wireless," in *Proc of 17th annual Intl. Conf. on Mobile computing and networking (Mobicom)*, 2011, pp. 301–312.

[85] J. Kimionis and M. M. Tentzeris, "Pulse shaping: The missing piece of backscatter radio and RFID," *IEEE Trans. Microw. Theory Techn.*, vol. 64, no. 12, pp. 4774–4788, 2016.

[86] B. Kellogg, A. Parks, S. Gollakota, J. R. Smith, and D. Wetherall, "Wi-Fi backscatter: Internet connectivity for RF-powered devices," in *ACM SIGCOMM Computer Communication Review*, vol. 44, no. 4. ACM, 2014, pp. 607–618.

[87] J. Rosenthal and M. S. Reynolds, "A 158 pJ/bit 1.0 Mbps Bluetoothlow energy (BLE) compatible backscatter communication system for wireless sensing," in *in 2019 IEEE Topical Conference on Wireless Sensorsand Sensor Networks (WiSNet)*, Jan 2014.

LIST OF FIGURES

LIST OF TABLES